## MAGNESIUM ISOTOPIC ZONING OF AN OLIVINE GRAIN FROM LUNAR MICROGABBRO 15555: CONSTRAINTS ON CRYSTALLIZATION AND COOLING.

F. M. Richter[1], M. Chaussidon[2], and R.A. Mendybaev[1], and L.A. Taylor[3].[1]The University of Chicago, 5734 S. Ellis, Chicago, IL 60637 , [2]Institut Phsique du Globe de Paris, Paris, France, [3]University of Tennessee, Knoxville, TN 37996. (richter@geosci.uchicago.edu.)

Introduction: Apollo 15 brought back a large olivine-normative sample of mare basalt - sample 15555. A review of the petrology of this sample along with extensive references is given in <http://curator.jsc.nasa.gov/lunar/lsc/15555r.pdf>. Several papers presented at the 8th and 9th Lunar Science Conference are especially relevant to our present study of sample 15555 having reported experimental data on the crystallization of a plausible parental melt [1] and used Fe-Mg zoning of olivine to estimate cooling rates of the order of a few°C/day [2,3]. We expand on these earlier works using magnesium isotopic data to document the extent of Fe-Mg exchange by diffusion and how this modified the crystallization zoning of the olivine grain from sample 15555 shown below.
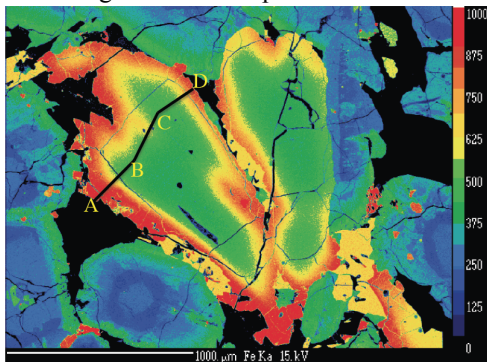

Figure 1. *FeKα image of a zoned olivine grain from lunar sample 15555 and surrounding minerals.*

Elemental and Mg Isotopic Analyses: The major element composition along the traverse A-B-C-D shown in Fig. 1 was measured using a JEOL JSM-5800LV scanning electron microscope equipped with an Oxford Link ISIS-300 energy dispersive X-ray microanalysis system giving a precision of better than 1% relative. The Mg isotopic composition at selected points across olivine grain and of matrix correction standards was measured with the CAMECA ims 1270 multicollector ion microprobe at the Centre de Recherches Pétrographiques et Géochimiques in Nancy France. The matrix correction was +2‰ at 30wt% MgO decreasing linearly to 0‰ at 5wt% MgO. The Mg isotopic fractionation is reported in per mil as

$$\delta^{26}Mg(‰) = 1000 \times \left(\frac{(^{26}Mg/^{24}Mg)_{sample}}{(^{26}Mg/^{24}Mg)_{reference}} - 1 \right)$$

Results: Figure 2 shows the olivine composition along traverse A-B-C-D in Fig. 1. Both Figs. 1 and 2 suggest that the olivine grain is actually two separate grains that became joined at an early stage of crystallization. For this reason we will focus our modeling on the segment A-B of the traverse across the olivine grain in Fig. 1. Figure 3 shows the Mg isotopic fractionation between 0 and 300 µm from the left edge of the grain.
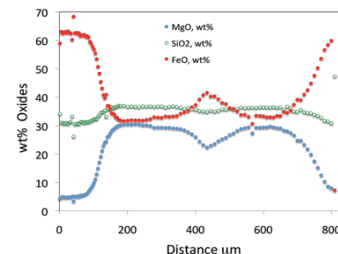
Figure 2. *Wt % of the major oxides measured along the traverse A-B-C-D shown in Fig.1.*
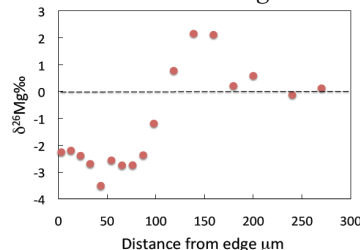
Figure 3. *Mg isotopic fractionation relative to the interior composition along segment A-B shown in Fig. 1. The 2σ errors are smaller than the symbols.*

Diffusion Model Specifications: The diffusion model usede to fit the data shown in Figs. 2 and 3 is based on the one-dimensional mass conservation equation for total magnesium or any of the isotopes written as

$$\frac{\partial C_i}{\partial t} = \frac{\partial}{\partial x}\left(D_i \frac{\partial C_i}{\partial x} \right), \qquad (1)$$

with the diffusion coefficient D_i in the case of isotopes depending on their mass. For the relative diffusivity of magnesium isotopes ^{24}Mg and ^{26}Mg, we use

$$\frac{D_{^{24}Mg}}{D_{^{26}Mg}} = \left(\frac{26}{24} \right)^{\beta} \qquad (2)$$

with $\beta \sim 0.2$ [4] for olivine. We also need to take into account that the diffusion coefficient of magnesium in olivine is a strong function of temperature, fayalite content, crystallographic orientation, and weakly, but not negligibly, of the fO_2. For D_{24Mg} in the c-axis direction we use the parameterization from [5]

$$LogD = -9.21 - 201kJ/(2.303RT) + 3(X_{Fa} - 0.1) + 0.42 \qquad (3)$$

where D is in m²/s, R is the gas constant, T is absolute temperature, X_{Fa} is the mole fraction fayalite, and fO_2 1.5 log units below IW was assumed. The simplest version of the diffusion problem requires specifying an initial condition and boundary conditions at the two ends of the profile being modeled. Posed in this fash-

ion, the calculation represents the limit when the crystal growth time scale is significantly shorter than the diffusion time scale and one can neglect any significant diffusion during the growth stage of the crystal. The results below show that this is not an unreasonable limit in that diffusion only had a relatively minor effect at modifying the zoning of the olivine grain. A more complete model will require calculating diffusion as the crystal grows, but this requires many quantities (i.e., grain radius as a function of time, temperature and composition) that we are not yet able to specify.

Model #1: Initial Zoning as a Step Function: In an earlier modeling effort of the elemental zoning of the same olivine grain we presently studying, [2] assumed a step function for the initial condition that was subsequently modified by diffusion. This model is interesting because, as shown in Fig. 4, it cdoes produce a good fit to the wt% MgO data, but only if the compositional dependence of the magnesium diffusion is minimal. Figure 4 also serves to illustrate the effect of diffusion being a strong function of olivine composition as given by Eqn. (3) and that once this is taken into account, the calculated profile is very different from that of the constant diffusion case and no longer fits the measured data.
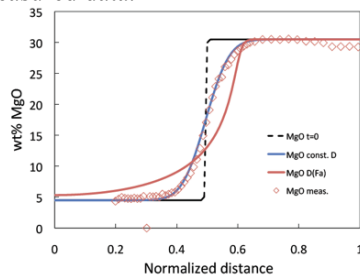

Figure 4. *Model diffusion profiles as a function of normalized distance ($X_{A-B}/300\mu m$) calculated assuming a constant diffusion coefficient (black line) and when diffusion depends on composition (red line) as given by Eqn. (3). A no-flux boundary condition was used at both ends. The red diamonds show the measured data.*

An important point to note in Fig. 4 is that in the constant diffusion coefficient case the calculated profile has the same curvature on both sides of the original step, but when the diffusion depends on composition the curvature at the higher magnesium side is much sharper than at the low magnesium side. This is due to the fact that the diffusion coefficient at 30.5 wt% MgO (Fa#~35) is about two orders of magnitude smaller than at 4.5 wt% MgO (Fa#~65). This implies that the observed zoning at the higher magnesium end must be primarily due to crystallization because it could not have been significantly affected by subsequent diffusive transport.

Model #2: Initial Zoning Required to Fit the Measured data: Figures 5a and 5b show the results of a calculation in which the initial zoning was prescribed so that the diffusion-modified zoning results in a good fit to both the wt% MgO and the Mg isotopic data.
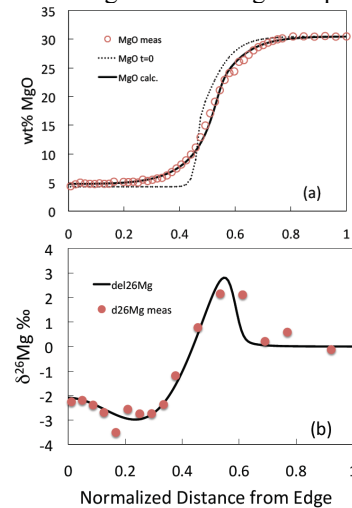
Figure 5. *Measured data (red circles) compared to calculated wt% MgO (a) and Mg isotopic fractionation (b) calculated using the starting composition shown by the dotted line in (a), with the diffusion coefficient specified by Eqn. (3), the isotope fractionation exponent β =0.18, and no flux at normalized distance 0,1. A uniform initial isotopic composition was assumed*

Discussion: The magnesium isotopic data are crucial for demonstrating that diffusion did take place, but that it had a rather limited impact on the final zoning of the olivine grain, especially at the higher magnesium portion of the grain. At the lower magnesium concentrations diffusion becomes increasingly important with portions of the sample losing magnesium becoming isotopicly heavy and those gaining magnesium becoming isotopicly light. This is the result of ^{24}Mg diffusing slightly faster than ^{26}Mg as given by Eqn. (2). The extent of diffusion as documented by the isotopic fractionation can be used to constrain the cooling history, which using the diffusion coefficient given by Eqn. (3), results in an estimated linear cooling rate of about 10°C/day, broadly consistent with previous estimates [2,3]. A cooling rate of the order 10°C/day and the associated crystallization of microgabbro 15555 would have been realized at a depth of less than ten meters below the surface of a lava flow cooled by thermal diffusion.

References: [1] Walker D. et al. (1977) *Proc. 8th Lunar Sci. Conf.* 1521-1547. [2] Taylor L.A. et al. (1977) *Proc. 8th Lunar Sci. Conf.* 1581-1592. [3] Onorato P.I.K. et al. (1978) *Proc. 8th Lunar Sci. Conf. 613-628.*[4] Sio C.K.I. et al. (2013) *Geochim. Cosmochim Acta.* 123, 302-321. [5] Dohmen R. and Chakraborty S. (2007) *Phys. Chem. Minerals.* 34, 597-598.

THE COMPOSITION OF THE FLUX OF MICROMETEORITES AFTER THE L-CHONDRITE PARENT BODY BREAKUP ~470 MA AGO: ≤1% H CHONDRITIC, ≥99% L CHONDRITIC.

P. R. Heck[1,2,3], B. Schmitz[1,4], S. S. Rout[1,2], T. Tenner[5], K. Villalon[1,2,3], A. Cronholm[4], F. Terfelt[4], and N. T. Kita[5], [1]Robert A. Pritzker Center for Meteoritics and Polar Studies, Field Museum of Nat. Hist., 1400 S Lake Shore Dr, Chicago, IL 60605, USA. E-mail: prheck@fieldmuseum.org. [2]Chicago Center for Cosmochemistry, [3]Dept. of Geophysical Sciences, Univ. of Chicago, 5734 S Ellis Ave, Chicago, IL 60637, USA. [4]Astrogeobiology Laboratory, Dept. of Physics, Lund Univ., P.O. Box 118, SE-221 00 Lund, Sweden. [5]WiscSIMS, Dept. of Geoscience, Univ. of Wisconsin-Madison, 1215 W Dayton St, Madison, WI 53706-1692, USA.

Introduction: The motivation for the present study was to find H-chondritic material in ~470 Ma old mid-Ordovician limestone that contains highly abundant L-chondritic material. The latter has been identified as debris from the L-chondrite parent body breakup (LCPB) in the asteroid belt ~470 Ma ago and the flux of L chondrites to Earth has been estimated as ~100× higher than today [1]. This L-chondritic debris, ranging from micrometeorites (MMs) and meteorites, to larger fragments that formed impact craters, dominated the extraterrestrial material that arrived on Earth over a period of more than 1 Ma after the LCPB [1]. This is very different from today, where H and L chondrites fall at about the same rate (H/L meteorite fall ratio is ~0.9; [2]. It is intriguing to search for the small fraction of other chondritic material to determine what other chromite-bearing extraterrestrial material arrived on Earth during a time that was dominated by L chondrites. The mineralogy of MMs and meteorites had been altered during the ~470-Ma-long residence in the sediments and the objects became fossilized. Only chromite and chrome-spinel have retained their original compositions. Average elemental concentrations of a large number of samples are used for classification, e.g., [3]. For individual grains elemental analysis is combined with oxygen isotopic analysis of single grains by SIMS [4]. Out of the 101 recovered fossil meteorites only one is not L chondritic and was classified as winonaite-like [5]. Fossil MMs are more abundant than fossil meteorites and are found as sediment-dispersed extraterrestrial chromite and chrome-spinel (SEC) grains. Elemental averages of hundreds of SECs from mid-Ordovician sediments from Sweden, China and Russia are consistent with L-chondritic composition, e.g., [3,6–8]. An L-chondritic origin of 24 individual SECs from Sweden and Russia was found [4].

Here, we expand the sample base to 120 SEC grains for elemental and oxygen isotopic analysis to search for non-L-chondritic grains.

Samples and Methods: Because of their abundance, SECs can be more readily recovered than fossil meteorites and are well suited for the present study. We randomly selected a total of 120 SECs (63-120 μm in diameter): 83 SECs from three sediment beds from the Thorsberg quarry in Sweden, and 37 SECs from correlated sediments at the Lynna River section in Russia. The grains were extracted from limestone by acid dissolution and sieving and identified with SEM/EDS [8]. Flat-polished epoxy grain mounts were prepared with centrally mounted chromite standard UWCr-3 [4] and imaged by SEM.

Grains on gold-coated mounts were analyzed with a Cameca IMS-1280 SIMS for three oxygen isotopes with conditions and procedures according to [4]. This includes monitoring and correction for the hydride tailing interference on $^{17}O^-$.

A total of 519 analyses were performed on the SECs and the standards. After SIMS analysis major and minor elemental compositions were determined quantitatively with SEM/EDS and grains were imaged again by SEM [10]. All elemental concentrations in SECs were compared to ranges observed in modern meteorites. Of all elements Ti and V are most inert to diagenetic alteration in SECs. Although there is overlap in TiO_2 and V_2O_3 contents among chromites and chrome-spinels from the different ordinary chondrite groups, the overlap is smaller for TiO_2.
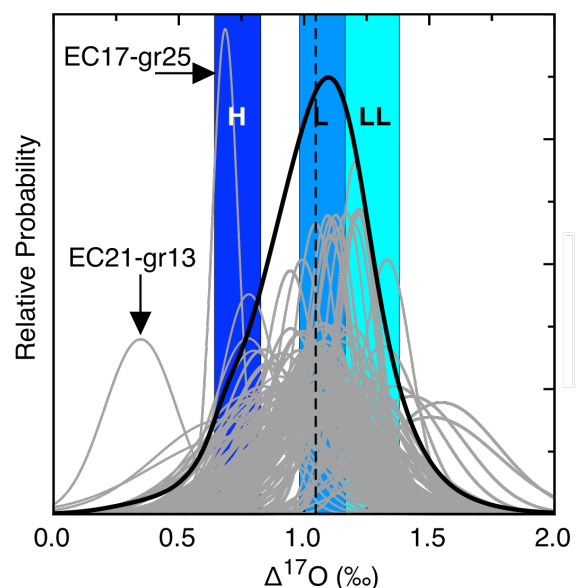

Fig. 1. Each grey curve represents the probability density for a $\Delta^{17}O$ value of a SEC grain. The bold black curve is the sum of all probabilities. Shaded fields are group averages±SD for bulk meteorites reported by [9].

Thus, TiO_2 is more useful to distinguish between the different groups, e.g., [3]. $\Delta^{17}O$ values ($=\delta^{17}O-0.52\times\delta^{18}O$) of the SEC grains were calculated and compared together with TiO_2 contents to values of known ordinary chondrites.

Results and Discussion: 113 out of 120 SECs have $\Delta^{17}O$ values (0.8‰ to 1.5‰; average 1.05‰±0.16‰) and TiO_2 contents (1.7 to 3.6 wt%; average 3.0±0.3 wt%) that match equilibrated L-chondritic composition (Figs. 1,2). Within error, some of the data falls into the natural overlap of L and LL chondrites. Although for those samples we cannot unambiguously distinguish between the L and LL chondritic, we think an LL chondritic composition is unlikely because the grains with the highest $\Delta^{17}O$ values that fall into the LL and L ranges have lower TiO_2 contents than grains with lower $\Delta^{17}O$ values, not higher TiO_2 as would be expected for LL chondrites. Five further grains have lower $\Delta^{17}O$ values (0.7‰ to 0.8‰) consistent with the H-chondritic range but their errors reach into the L-chondritic field and their TiO_2 contents are best matched with L-chondritic values (Figs. 1,2). Thus, based on the data an H-chondritic origin is difficult to support for any of these SECs.

In contrast, one additional grain from Thorsberg (EC17-gr25) is possibly H chondritic as its $\Delta^{17}O$ value within its error (0.7‰±0.1‰) is H chondritic (Fig. 1) and its TiO_2 content (2.5±0.1 wt%) is also consistent with H chondritic (Fig. 2). There is one grain (EC21-gr13) whose origin we cannot explain as its $\Delta^{17}O$ value (0.3±0.1‰) falls between H-chondritic and terrestrial values and its TiO_2 content (2.6±0.2‰) falls into the range of H and L chondrites (Fig. 1). We cannot fully exclude that we sampled a crack filled with epoxy or with a terrestrial alteration phase that resulted in a mixed signal. There is a very low probability that the low $\Delta^{17}O$ values in this and the previously discussed grain are from chondrules of any ordinary chondrite group. It is unlikely that any of the SECs are from chondrules because chromites in chondrules are usually much smaller than the SECs studied here and coarse chromite is very rare in chondrules (<0.1% [11]).

Our finding of one H-chondritic SEC out of 119 L-chondritic SECs is in agreement with the following estimate that is independent of our data: For the sake of this argument we assume the present-day fraction of H chondrites among ordinary chondrite falls (~42%; [2]) for the background flux not related to the LCPB ~470 Ma ago. We also assume that the H/L-chondritic abundance ratio of micrometeorites is similar to the ratio of macroscopic meteorites. We discuss this in [10] based on data from recent ordinary chondritic micrometeorites, e.g., [12,13]. We then use the previous estimate of a 100× higher flux of L-chondritic ma-

terial to Earth and find that only one H-chondritic sample (0.9%) out of 119 samples would be expected.

Conclusions: Our study strengthens conclusions from previous studies that L-chondritic material dominated the flux of extraterrestrial matter to Earth after the LCPB event. We conclude that the upper limit for the fraction of H-chondritic micrometeorites in post-LCPB sediments is 1%. With this upper limit we predict that a fossil H chondrite will be discovered in the Swedish Thorsberg quarry within the next decade at current fossil meteorite discovery rates. In our discussion we illustrate the usefulness of the combined approach of using $\Delta^{17}O$ and TiO_2 for classifying SECs. Although there are limitations due to natural overlap of compositions, none of the indicators alone would be sufficient to classify an individual SEC.
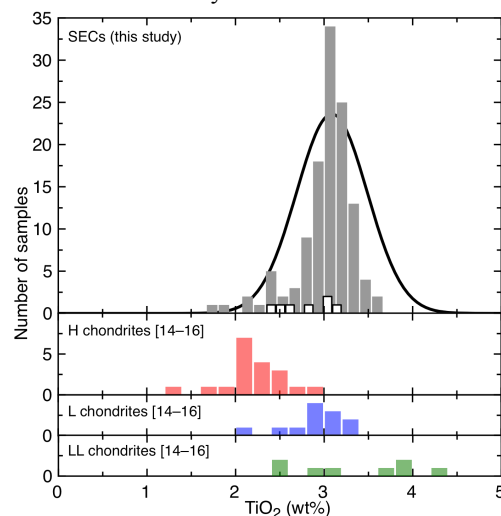

Fig. 2. TiO_2 of studied SECs compared with chromites from equilibrated ordinary chondrites. SECs with low $\Delta^{17}O$ are shown as a white histogram in the top panel.

References: [1] Schmitz B. (2013) *Chemie der Erde 73*, 117–145. [2] Meteor. Bull. Database (2015), http://www.lpi.usra.edu/meteor. [3] Schmitz B. and Häggström T. (2006) *MAPS 41*, 455–466. [4] Heck P. R. et al. (2010) *GCA 74*, 497–509. [5] Schmitz B. et al. (2014) *EPSL 400*, 145–152. [6] Schmitz B. et al. (2008) *Nat. Geosci. 1*, 49–53. [7] Lindskog A. et al. (2012) *MAPS 47*, 1274–1290. [8] Schmitz B. et al. (2003) *Science 300*, 961–964. [9] Clayton R. N. et al. (1991) *GCA 55*, 2317–2337. [10] Heck P. R. et al. (2016) *GCA* (in press). [11] Krot A. N. and Rubin A. E. (1993) *LPS 24*, 827–828. [12] Van Ginneken M. et al. (2012). *MAPS 47*, 228–247. [13] Prasad M. S. et al. (2015) *MAPS 50*, 1013–1031. [14] Snetsinger K. G. et al. (1967) *Am. Min. 52*, 1322–1331. [15] Bunch T. E. et al. (1967) *GCA 31*, 569–1582. [16] Wlotzka F. (2005). *MAPS 40*, 1673–1702.

SEDIMENT COMPACTION ON MARS AND ITS EFFECT ON LAYER ORIENTATION. L. R. Gabasova[1] and E. S. Kite[2], [1]University of Paris-Saclay (l.r.gabasova@gmail.com), [2]University of Chicago (kite@uchicago.edu)

Introduction: Compaction, or the progressive loss of porosity of a loaded sediment, influences many geological phenomena such as fluid flow, diagenesis and faulting. Quantifying the effect of compaction is thus essential to understanding the history of a sedimentary basin. For example, [1] argue that compaction may account for layer tilting in the sediment mount in Gale crater (154 km diameter, 5.4S°S, 137.8°E). Determining the cause of the layer tilting may be important in reconstructing paleofluvial processes in Gale. Here, we model the compaction of sediment infill in Gale and Gunjur (27 km diameter, 0.2°S, 146.7°E) and compare its effects on layer orientation to measured layer dips and faulting.

Data: The Gunjur data is in the form of 120 radial depth profiles measured from a CTX DTM. The Gale layer dip measurements were produced by layer tracing on eight HiRISE DTMs. The first six came from [2]; the other two were traced by Jonathan Sneed in 2015. Contra [1], outward dips at Gale have been independently confirmed (e.g., [3-5]).

Method: To determine the effect of compaction on sediment thickness, we make the following assumptions:

(1) present-day compaction represents maximum pressure during sediment's lifetime (no rebound after erosion)

(2) porosity decays exponentially with depth [6], taking the form $\phi = \phi_0 \times e^{-cz}$ with ϕ_0 and c values taken from [7] and [8] and adjusted for Martian gravity ($c_{Mars} = c_{Earth} \div 9.81 \times 3.71$).

Lithology	Sand	Shale [7]	Shale [8]
c_{Mars} (m^{-1})	0.1021	0.1929	0.3139
ϕ_0	0.49	0.63	0.70

Table 1. Compaction parameters used for calculations

(3) height is uniquely determined by porosity.
(4) the basal surface is noncompactible (e.g., basalt).

To find the original height of a compacted sediment column, we integrate porosity over z, which gives us:

$$z_{uncompacted} = \frac{z + \frac{\phi_0}{c} \times (e^{-cz} - 1)}{1 - \phi_0}$$

To obtain the compacted height of a sediment column, we use simple numeric iteration to converge towards the height that would produce the original column height upon decompaction.

Two adjacent columns of different thicknesses will compact to different extents, and the resulting slope naturally translates to layer tilting.

Gunjur crater. In the case of Gunjur crater, we focus on determining whether compaction-induced subsidence could cause concentric faulting around the crater rim and peak. To do this, we calculate sediment thickness and compaction along the radial profiles and interpolate a grid in order to create a horizontal gradient map, which we then compare with the geomorphological map of the basin.

Gale layer orientation. For Gale, we evaluate the hypothesis of [1] in 1D: we study the effect of compaction on layer tilting in a cross-section from the peak to the rim of the crater, assuming axisymmetry. We examine the effect of different grain lithology as well as different basal surface shape. The possible basal surfaces are taken from pristine Martian craters, scaled appropriately using formulas from [9], as well as a section of Gale itself taken from its southern side, where we assume either little sedimentation or near-total erosion has occurred.
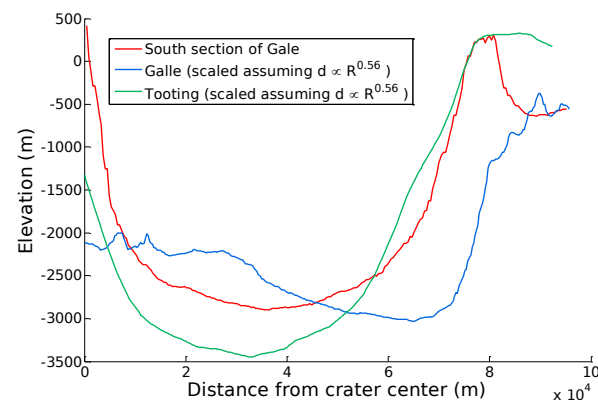

**Fig. 1. Basal surface comparison with scaling parameters from [9].**

We try multiple possibilities for the shape of the infill, using Chebyshev polynomials [10] to model its surface. Our model is restricted to even-degree polynomials up to degree 4.

We then calculate the layer dips produced in the measurement locations for all plausible values of $\{k_0, k_2, k_4\}$ and the mean square error between the calculated and measured layer dips, which have been projected on the radial axis. The lowest mean square errors occur for extraordinarily large sediment thicknesses. Therefore, we have focused on reducing the thickness of the sediment infill rather than the mean square error on the dip. The radial projection means that any azimuthal variation in the geological processes causing the dipping is not taken into account, but instead introduces further

error to the data. Perfect agreement is thus not to be expected.

Results and discussion: At Gunjur, gradients in compaction are maximal near the outer edge of the sediment fill and near the central peak, consistent with the locations of observed circumferential graben. The next step is to compare the strains predicted by the compaction model with graben offsets measured from HiRISE DTMs.

The Chebyshev modeling of the infill in Gale produces a variety of results. We find a smaller error with Galle as a basal surface as opposed to Tooting or the southern part of Gale itself; most likely this is due to its slight outward slope, as the measured dips are also directed outwards. This is consistent with the theory that Gale, like Galle, contains a central ring which is concealed within Mount Sharp [11].
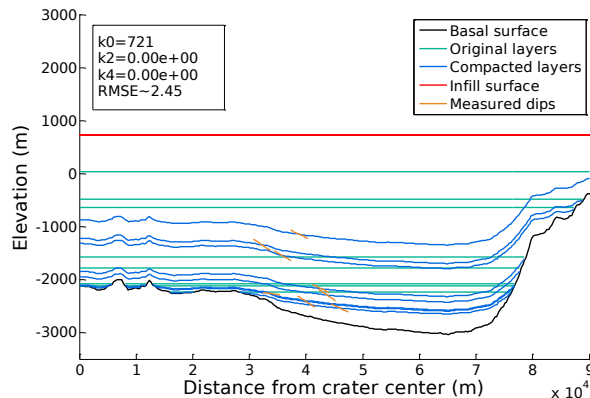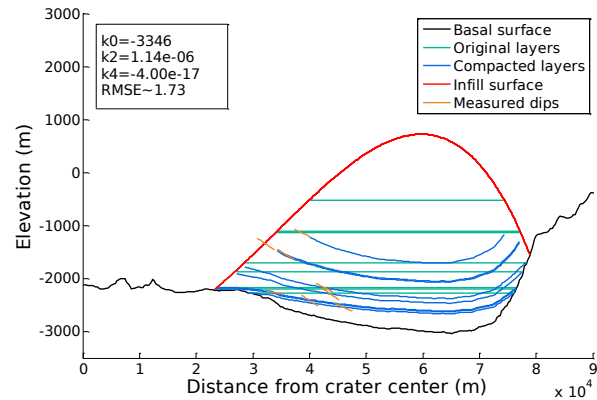

Fig. 2. Gale best-fit scenario with flat infill, using shale lithology and Galle as basal surface.

We can see in Fig. 2 that due to the near-horizontality of the basal surface, a flat sediment infill will not cause significant layer tilting in the locations where it has been measured. This disparity is slightly mitigated by the tilt of the basal surface itself in the case of Galle, but not sufficiently.

Generating a more rugged infill surface gives far more promising results. A model with only a nonzero k_2 (thick around the rim, thins out towards crater peak) is geologically easier to explain with a sediment source located outside the crater rim, but a sediment load of dozens of kilometers is not physically plausible. However, an infill modeled with k_2 and k_4 is reduced to a more realistic thickness towards the rim (see Fig. 3).

It is more difficult to find a formative geological process for the torus shape generated in this case. However, 'lumpy' sediment mounds do occur, for example in Nicholson crater, which may be explained by aeolian processes [12].

Fig. 3. Gale best-fit scenario with convex infill determined by 4th-degree Chebyshev polynomial, using shale lithology and Galle as basal surface.

Shale produces the lowest MSE and smallest sediment thickness [7,8].

In summary, compaction in Gale can only produce the observed outward sign of layer tilting if the basal surface has a central ring, or if the sediment load is torus-shaped and extraordinarily thick (dozens of kilometers). Excluding extraordinarily thick paleo-sediment thicknesses, compaction in Gale can approximately match the measured tilt if (i) the basal surface is shaped like a central ring, (ii) the infill compacted like shale, (iii) the sediment load was torus-shaped.

Continued exploration of the Gale sediment mound, and identification of fluvial paleoflow directions, will allow us to conclude more decisively on whether the dips are driven by compaction: if previously horizontal layers are tilted due to sediment subsidence, fluvial deposits directed "uphill" on modern topography are likely.

References: [1] Grotzinger J. P. et al. (2015) *Science* 350(6257):aac7575. [2] Kite E. S. et al. (2013) *Geology,* 41(5), 543-546. [3] Fraeman et al. (2013) *Geology,* 41(10), 1103-1106. [4] Le Deit et al. (2013) *J. Geophys. Res.* 118, 2439-2473. [5] Stack et al. (2013) *J. Geophys. Res.* 118(6), 1323-1349. [6] Athy L. F. (1930) *AAPG Bulletin,* 14, 1-24. [7] Hantschel T., Kauerauf A. I. (2009) *Fundamentals of Basin and Petroleum Systems Modeling*, Springer. [8] Sclater J. G., Christie P. A. F. (1980) *J. Geophys. Res.* 85(B7), 3711–3739. [9] Tornabene L. L. et al. (2013) *LPS XLIV,* Abstract #2592. [10] Mahanti, P., et al. (2014) *Icarus* 241, 114-129. [11] Allen. C. C. et al. (2014) *LPS XLV,* Abstract #1402. [12] Desai A. J., Murty S. V. S. (2013) *LPS XLIV,* Abstract #1180.

COSMIC-RAY EXPOSURE AND SHOCK DEGASSING AGES OF THE QUASICRYSTAL-BEARING KHATYRKA METEORITE M. M. M. Meier[1], L. Bindi[2], H. Busemann[1], P. R. Heck[3], A. I. Neander[4], C. Maden[1], M. Riebe[1], N. H. Spring[5,6], P. J. Steinhardt[7], R. Wieler[1]. [1]Institute of Geochemistry & Petrology, ETH Zurich, Switzerland (matthias.meier@erdw.ethz.ch); [2]Department of Earth Sciences, Università di Firenze, Italy; [3]Robert A. Pritzker Center, Field Museum of Natural History, Chicago, USA; [4]Department of Organismal Biology & Anatomy, University of Chicago, USA; [5]SEAES, University of Manchester, UK; [6]Department of Earth & Atmospheric Sciences, University of Alberta, Edmonton, CAN; [7]Department of Physics & Princeton Center for Theoretical Science, Princeton Univ., USA.

Introduction: Quasicrystals (QCs) are materials with quasiperiodic arrangements of atoms. They can have symmetries forbidden for true crystals, e.g., icosahedral symmetry for icosahedrite ($Al_{63}Cu_{24}Fe_{13}$), the first known natural QC [1], and 10-fold azimuthal symmetry in the case of the more recently identified decagonite ($Al_{71}Ni_{24}Fe_5$) [2]. Icosahedrite was identified in a mm-sized rock sample belonging to the collection of the Natural History Museum of the University of Florence. The QCs were found in regions rich in khatyrkite ($CuAl_2$) and cupalite ($CuAl$). Oxygen isotopes in the silicate part of the Florence sample show that it is extraterrestrial [3]. Its provenance was traced back to a Soviet prospecting expedition. A new expedition to Chukotka, Russia, in 2011 succeeded in retrieving ~10 more mm-sized grains, from >8 ka old sediments of a tributary of the Khatyrka river. The grains had the same O isotopic composition as the Florence sample, and some of them also contained khatyrkite [4]. These grains are now known as the CV_{ox} chondrite Khatyrka. While the origin and formation of khatyrkite in Khatyrka is still unclear, a shock impact origin has been suggested for the QCs [5]. Here we present He and Ne concentrations and isotopic compositions of six olivine grains from Khatyrka, in order to reconstruct its cosmic history and relationship to other CV chondrites.

Methods: We analyzed six forsteritic olivine (#Mg ~0.96) grains <50 μm in diameter, from fragment #126 [4]. The analysis of He and Ne in such small grains is possible due to a high-sensitivity compressor-source noble gas mass spectrometer connected to an ultra-low blank line at ETH Zurich [6]. Given the low mass of the grains (~0.75 μg total), weighing them was not possible. Instead, we used a μCT scanner with a voxel length of 5.47 μm to determine grain volumes, and calculated grain masses assuming a density of forsteritic (#Mg= 0.95±0.05) olivine (3.33± 0.06 g/cm³). After micro-manipulator transfer of the grains to a sample holder for He-Ne analysis, they were loaded into the mass spectrometer and exposed to ultra-high vacuum for several days before being individually heated with a Nd:YAG laser (λ = 1064 nm) for 60 s to their melting point. He-Ne analysis was done using a protocol based on the one originally developed by Heck et al. [7]. We calculate cosmic-ray exposure (CRE) ages using a cosmogenic nuclide production model [8] for a carbonaceous chondrite matrix and forsteritic target chemistry.

Results: Results are given in Table 1. The reported volumes are 20% smaller compared to the ones given in an earlier abstract [9], due to an improved evaluation of grain volumes including a correction for variable voxel brightness near grain boundaries. All grains show cosmogenic ^3He and ^{21}Ne, corroborating an extraterrestrial origin. A fully cosmogenic origin was assumed for ^3He, while ^{21}Ne was corrected for atmospheric Ne (3-29% of measured ^{21}Ne) using a two-component deconvolution with cosmogenic and atmospheric Ne as end-members. Five grains have an average cosmogenic $^3He/^{21}Ne$ ratio of 3.6±0.3, except for grain 3, where it is 7.3±0.8. All six grains should have the same ratio, as they were irradiated by cosmic rays close to each other within the same mm-sized volume. Since grain 3 has, within uncertainty, the same mass and ^3He concentration as grain 1, yet shows a significantly lower ^{21}Ne concentration, we presume that it was not completely degassed in ^{21}Ne during analysis. A second laser shot onto grain 3 (melt residues) did not result in the release of additional He and/or Ne above detection limit.

#	Vol. (μm³)	Mass (ng)	$^3He/^4He$ ×10⁻⁴	^{20}Ne /^{22}Ne	^{21}Ne /^{22}Ne	^3He_c	$^{21}Ne_c$	R4 (Ma)
1	35800 ±2300	119 ±8	>470	3.6 ±2.5	0.42 ±0.08	6.6 ±0.3	2.3 ±0.1	<260
2	31200 ±2100	104 ±7	38 ±6	9.4 ±0.9	0.09 ±0.01	5.3 ±0.2	1.4 ±0.2	2750 ±660
3	37400 ±2400	125 ±8	400 ±250	11.2 ±1.7	0.13 ±0.02	6.6 ±0.2	0.9 ±0.1	270 ±80
4	47900 ±3000	160 ±10	330 ±150	5.5 ±2.0	0.40 ±0.06	9.9 ±0.3	3.0 ±0.1	400 ±120
5	44900 ±3800	209 ±17	>270	7.9 ±0.9	0.12 ±0.01	8.7 ±0.4	2.0 ±0.2	<350
7	29700 ±2500	99 ±9	>340	2.5 ±5.3	0.29 ±0.08	4.3 ±0.2	1.1 ±0.2	<310
t	227000 ±6700	756 ±23	-	8.1 ±0.6	0.18 ±0.01	41.3 ±0.7	10.6 ±0.4	-

Table 1: Volumes, masses, He, Ne isotopic composition, cosmogenic ^3He, ^{21}Ne amounts (in 10⁻¹⁵ cm³ STP) and radiogenic ^4He retention ages ("R4", in Ma) of Khatyrka olivine grains. t = total.

As shown in Fig. 1, He is likely a two-component mixture of cosmogenic He ($^4He/^3He$ = ~6) and radio-

genic ^{4}He, similar to chondrules from the CV chondrites Leoville and Allende [10]. To calculate a (U,Th)-He age, we use U and Th concentrations of 14-22 and 49-77 ppb, respectively, measured in Allende chondrules [11]. All except grain 2 (2.8±0.7 Ga) have retention ages consistent with ~250-300 Ma.

To calculate the ^{21}Ne CRE age of Khatyrka, we need to determine a production rate, which depends on the position of the sample within the meteoroid and its radius, and thus requires a shielding indicator [8]. Since typical shielding indicators like the cosmogenic ^{22}Ne/^{21}Ne ratio or radionuclides are not available for the Khatyrka grains, we use ^{3}He/^{21}Ne instead. Elemental fractionation between He and Ne (e.g., diffusion losses) since the start of CRE must be minimal as the data points of the grains plot close to the radiogenic-cosmogenic mixing line in Fig. 1. The CRE age curves given in Fig. 2 are for an average cosmogenic ^{21}Ne concentration of 1.51×10^{-8} cm^3 STP/g (i.e., excluding partially degassed grain 3). At the ^{3}He/^{21}Ne ratio measured in the grains, the CRE age of Khatyrka is thus likely in the range ~2-5 Ma, although it could be higher if the meteoroid was very large (R > 5 m). The minimal meteoroid radius (based on ^{3}He/^{21}Ne) is 0.5 m.

Three metallic grains, initially thought to be khatyrkites and analyzed for He and Ne in July 2015 [9], turned out to be samples unrelated to Khatyrka. At this point, we have not taken any measurements from khatyrkite found in the Khatyrka meteorite, although we plan to do so.

Discussion: Khatyrka likely experienced a strong shock ~250-300 Ma ago, but the (U,Th)-He clock was reset inhomogeneously, which is expected in the pres-

Fig 2: Ne-21 CRE ages of Khatyrka olivine as a function of ^{3}He/^{21}Ne, for a range of meteoroid sizes, based on [8]. The shaded region represents the average ^{3}He/^{21}Ne ratio (of the five fully degassed grains) of 3.6±0.3. This range excludes very low shielding in small objects and very high shielding in large objects, and constrains the CRE age to 2-5 Ma.

sure range 10-35 GPa (S3-S5) [12]. This event might thus correspond to the >5 GPa, >1200°C shock event identified by [5] in Khatyrka. Only four CV chondrites have similar CRE ages: Allende [8], ALH 85006 [13], and Acfer 082 and 272 [14]. The former two both have U,Th-He ages >3.8 Ga. While the U,Th-He ages are <0.5 Ga for the latter two, this is likely due to solar heating [14], which is unlikely for Khatyrka given the nearly unfractionated He/Ne ratio (Fig. 1). Khatyrka is thus unique among CV chondrites for having a very short U,Th-He shock age of ~0.3 Ga. This might indicate that Khatyrka is derived from another parent asteroid than the other CVs with known cosmic histories.

References: [1] Bindi L. et al. (2009) *Science* 324, 1306-1309. [2] Bindi L. et al. (2015) *Sci. Rep.* 5, 9111. [3] Bindi L. et al. (2012) *Proc. Nat. Acad. Sci.* 109, 1396-1401. [4] MacPherson G. et al. (2013) *Meteorit. Planet. Sci.* 48, 1499-1514. [5] Hollister L. et al. (2014) *Nat. Comms.* 5, 4040. [6] Baur H. (1999) *EOS Trans.*, AGU 46, #F1118 (abstr.). [7] Heck P. R. et al. (2007) *Astrophys. J.* 656, 1208-1222. [8] Leya I. & Maserik J. (2009) *Meteorit. Planet. Sci.* 44, 1061-1086. [9] Meier M. M. M. et al. (2015) *78th Ann. Meeting Met. Soc.*, #5035 (abstr.). [10] Vogel N. et al. (2004) *Meteorit. Planet. Sci.* 39, 117-135. [11] Amelin Y. & Krot A. (2007) *Meteorit. Planet. Sci.* 42, 1321-1335. [12] Stoeffler D. et al. (1991) *Geochim. Cosmochim. Acta* 55, 3845-3867. [13] Wieler R. et al. (1999) *LPI contr.* 997, 90-94. [14] Scherer P. and Schultz L. (2000) *Meteorit. Planet. Sci.* 35, 145-153.
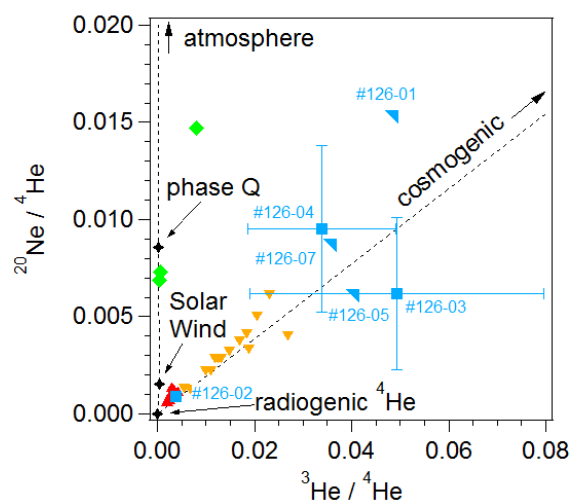

Fig. 1: Khatyrka olivines corrected for atmospheric Ne (blue; triangles are lower limits on both axes), CV chondrites Leoville (orange) and Allende (red) chondrules [10] and Acfer 082 and 272 (green) [14].
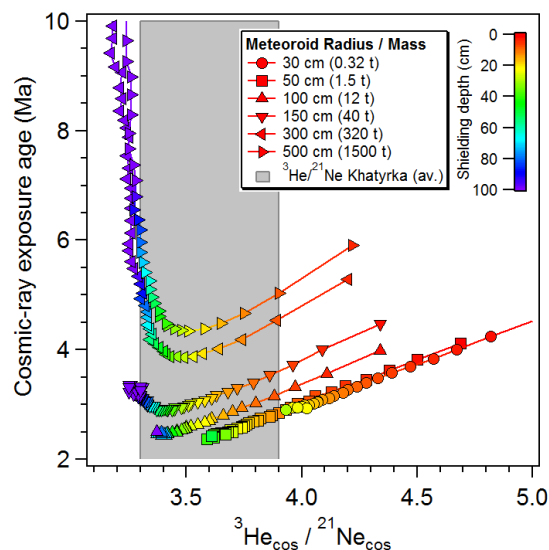
AN INTEGRATED WORKFLOW FOR PRODUCING DIGITAL TERRAIN MODELS OF MARS FROM CTX AND HIRISE STEREO DATA USING THE NASA AMES STEREO PIPELINE. David P. Mayer[1], Edwin S. Kite[1], [1]University of Chicago—Department of Geophysical Sciences (dpmayer@uchicago.edu).

Introduction: Stereo images represent a key dataset for producing digital terrain models (DTMs) of planetary surfaces. Nearly all of the high-resolution (<10 meters/pixel) stereo image data of Mars comes from the CTX and HiRISE sensors. However, CTX DTMs are not available through the PDS and fewer than 300 of the ~4400 HiRISE targeted stereopairs have been transformed to DTMs and released to the PDS as of December 2015. This often requires researchers who wish to incorporate CTX and HiRISE elevation data in their work to produce their own DTMs.

The NASA Ames Stereo Pipeline (ASP) is a free software package that can be used to create DTMs from stereo image data collected by a variety of sensors including CTX and HiRISE [1,2].

Here, we outline a procedure for producing CTX and HiRISE DTMs using ASP. The workflow is highly automated through the use of several Bash scripts that act as wrappers around the ASP routines and is configured for parallel processing in either a distributed computing environment or on a single machine. A human-in-the-loop is required at key steps in order to assess the overall quality of the stereo triangulation results and to estimate parameters necessary for aligning a preliminary DTM to reference elevation data. The workflow uses only free, open-source software, which minimizes the costs associated with producing DTMs.

Image Selection: We identify HiRISE stereo data for a given region of interest using the HiRISE team's database of deliberately targeted stereopairs (http://www.uahirise.org/stereo_pairs.php). We then select CTX stereopairs by first searching the PDS for images that were acquired simultaneously with the HiRISE images. If a corresponding CTX image pair is not available, we instead use the criteria outlined in [3] to identify alternative CTX image pairs that overlap with a given HiRISE stereopair.

CTX Processing:

Preprocessing. The CTX Experimental Data Records (EDRs) are prepared for ASP using the USGS Integrated Software for Imagers and Spectrometers (ISIS). The image data are converted from PDS to ISIS cube format with *mroctx2isis*. SPICE kernels are added to each image using *spiceinit* and the pointing data are smoothed using *spicefit*. A photometric calibration is applied using *ctxcal* followed by a correction for even/odd detector striping using *ctxevenodd*.

Bundle Adjustment. Each preprocessed stereopair is then bundle adjusted using ASP's *bundle_adjust* tool.

We have found that including this step minimizes "washboarding" in the final DTMs.

Preliminary Point Cloud/DTM Generation. ASP's *parallel_stereo* routine is used to generate an initial 3-dimensional point cloud for each stereopair. The use of the parallelized implementation of *stereo* allows much of the stereo extraction process to be distributed among many CPUs on potentially many computers, thereby increasing computational efficiency and reducing the time required to create a single point cloud. ASP's *point2dem* routine is then used to transform the point cloud into a DTM.

Point Cloud Alignment to MOLA. The preliminary CTX point cloud is aligned to MOLA datum elevations using ASP's *pc_align* routine. *pc_align* uses an iterative closest points algorithm to identify a 3-dimensional affine transform that optimizes the alignment between the ASP-derived point cloud and a reference elevation data set (i.e. MOLA). The routine requires an estimate of the largest expected displacement between the source and reference elevation data.

We import individual MOLA shot data that overlaps the CTX DTM into a GIS-compatible format and calculate the difference between the MOLA elevations and the nearest CTX DTM pixel. An analyst then inspects a histogram of the elevation differences and estimates the maximum displacement parameter for *pc_align*. We have found that an appropriate value typically corresponds to somewhere between the 95th and 99th-percentile of the differences between the MOLA and CTX elevations, after removing shots from MOLA orbits that are obvious outliers (elevation differences >>~4 standard deviations).

Final DTM and Orthoimage Generation. We produce a final CTX DTM and orthorectified version of the nadir-most image in the stereopair by passing the point cloud output by *pc_align* and the nadir-most image as input to *point2dem*.

HiRISE Processing:

Preprocessing. HiRISE EDRs are prepared for stereo processing using two Python scripts that are part of ASP. The Python scripts are wrappers for several ISIS routines. *hiedr2mosaic.py* ingests the EDRs into ISIS, apply SPICE kernels, smooth the SPICE data, perform photometric calibrations and mosaics the individual CCDs from each image. c*am2map4stereo.py* is then used to transform the images from each stereopair to a common map projection and spatial resolution.

Preliminary Point Cloud/DTM Generation. The map-projected images are passed as input to

parallel_stereo and the resulting point cloud is passed to *point2dem* in order to create a preliminary DTM.

Point Cloud Alignment to CTX. The preliminary HiRISE point cloud is aligned to a corresponding CTX DTM using *pc_align*. In order to estimate the maximum displacement parameter, an analyst first subtracts the preliminary HiRISE DTM from the reference CTX DTM and then inspects the histogram of the resulting difference raster. An appropriate value for the maximum displacement typically corresponds to approximately the 99th-percentile of the differences between the reference CTX DTM and the preliminary HiRISE DTM.

Final DTM Generation. We produce a final HiRISE DTM and orthorectified version of the nadir-most image of the stereopair using *point2dem* following a similar approach to that used with the CTX data.

DTM Availability: Our lab has produced CTX and HiRISE DTMs of sedimentary rocks in central Valles Marineris, Gunjur crater, Gale crater, and a small number of sites reported in the literature to contain chlorides. A list of DTMs that have been produced so far can be obtained from the lead author. Individual DTMs will be made available on request.

Code Availability: We plan to release the Bash scripts used in our CTX and HiRISE processing workflow and corresponding documentation through the University of Chicago's Git repository (https://psd-repo.uchicago.edu/groups/kite-lab) in spring 2016. Pre-release versions of the scripts are available from the lead author upon request.

References: [1] Moratto, Z. M., et al. (2010). Ames Stereo Pipeline, *LPSC XLI,* Abstract #2364. [2] Broxton, M. J. and Edwards, L. J. (2008), *LPSC XXXIX,* Abstract #2419. [3] Becker, K.J. et al (2015), *LPSC XLVI,* Abstract # 2703.

Acknowledgments: The authors wish to thank O. Alexandrov, F. Calef and C. Fassett for helpful discussions about stereo image processing. This work was completed in part with resources provided by the University of Chicago Research Computing Center.

VALENCE OF Ti, V and Cr in the REDUCED APOLLO 14 BASALTS 14053 and 14072. S. B. Simon[1] and S. R. Sutton[1,2], [1]Dept. Geophysical Sci., 5734 S. Ellis Ave.; [2]Center Adv. Radiation Sources (CARS), The University of Chicago, Chicago, IL 60637, USA (sbs8@uchicago.edu).

Introduction: The oxidation states of the transition metals in lunar samples have been subjects of some interest and controversy ever since the samples became available for study. The presence of trivalent Ti in lunar pyroxene has been inferred from electron probe [1, 2] and spectroscopic [3, 4] analyses, even though (a) the fO_2 of the Ti_2O_3/TiO_2 buffer lies several orders of magnitude below the iron-wüstite (IW) buffer; and (b) Fe^{3+} was reported [5], although [3] disputed the claim. The valences of Ti, V and Cr in the olivine and pyroxene of lunar igneous rocks, important indicators of the fO_2 of their source regions, can be readily measured nondestructively by XANES (X-ray absorption near-edge structure) spectroscopy. Our preliminary work [6] showed little Ti^{3+} but much higher than expected proportions of Ti in tetrahedral coordination; both observations call into question inferences of Ti^{3+} based on Ti/Al ratios >0.5 [1, 2].

In contrast, meteoritic Ti-, Al-rich pyroxene ("fassaite" [7]) has higher Ti contents but no Ti in tetrahedral sites [7], presumably due to the high availability of Al. Because high Al activity favors octahedral Ti, and trivalent Ti only enters octahedral sites in pyroxene, we extend our search for lunar Ti^{3+}-bearing pyroxene to two Al-rich basalts from the Apollo 14 site. Valences of Cr and V are also being investigated because they are redox indicators applicable to higher oxygen fugacities than Ti^{3+}/Ti^{4+}.

Samples and Methods: One polished thin section of 14053 and one of 14072 were studied. Areas of the sections to be analyzed were documented by SEM and analyzed by electron probe. XANES spectra were collected using the GSECARS X-ray microprobe in fluorescence mode, with a 1 µm X-ray beam. Titanium valences were determined following the results of [8], who demonstrated that Ti K-edge XANES spectra of pure Ti^{4+}-bearing minerals fall into two, distinct valence-coordination clusters on a plot of pre-edge peak intensity *vs.* energy. Those with all Ti in tetrahedral coordination have high intensities and low energies, whereas those with all Ti in octahedral coordination have low intensities and high energies. Any Ti^{3+} present in olivine and pyroxene is expected to be in octahedral coordination, yielding a third data cluster, pre-edge peaks with relatively low intensity and low energy [9]. Titanium valences in unknowns were determined by applying the lever rule to mixing lines for XANES results for standards representing these three endmember occurrences. Valences are reported as values between 3 and 4, representing averages for the analytical volumes, with uncertainties based on X-ray counting statistics. The valence of V was determined from the absolute intensity of the pre-edge peak ensemble compared to glass standards as in [9]. The valence of Cr was based on the intensity of the 1s-4s peak and standardized using spectra from Fe-free glasses dominated by Cr^{3+} or Cr^{2+} as in [10]. Valences of V and Cr are expressed as values between 2 and 3. For each analytical spot, spectra were collected at several different orientations and then merged (Ti) or the results averaged (Cr) to minimize orientation effects.

Sample petrography and mineral chemistry: Samples 14053 and 14072 have been considered paired [11], but [12] reported trace element differences that argue against this.

14053. An ophitic basalt with pyroxene grains up to 5 mm across enclosing plagioclase laths [13]. This sample was described as "the most reduced rock from the moon" [11] based on petrographic evidence for subsolidus reduction of Cr-ulvöspinel to chromite+ilmenite+Fe metal, and fayalite to metal + SiO_2. The pyroxene analyzed for this study has a wide range of compositions, representing early, Mg-rich ($En_{61}Wo_{12}Fs_{27}$) to late, Fe-rich ($En_4Wo_{19}Fs_{77}$) materials. Three coarse olivine grains, Fo_{64-68}, were analyzed.

14072. Also has pyroxene and plagioclase in an ophitic texture, plus rare olivine phenocrysts [13]. This sample has also been described as "intensely reduced" [14]. A narrower range of pyroxene ($En_{64}Wo_9Fs_{27}$-$En_{25}Wo_{25}Fs_{50}$) and a wider range of olivine (Fo_{35-61}) compositions than in 14053 were analyzed.

Results: Preliminary XANES data for vanadium indicate mixtures of V^{2+} and V^{3+} for olivine and pyroxene. Pyroxene valences in the two rocks are similar, with V^{3+} dominant. For olivine, the V valence in 14053 is more reduced than that in 14072. More extensive results are available for Ti and Cr.

Valence of Ti and Cr in pyroxene. Results are summarized in Fig. 1. In 14053, Ti valence ranges from 3.73 ± 0.08 to 4.19 ± 0.13 (1σ) and averages 4.00 ± 0.18. For 14072, the range and average are 3.42 ± 0.07 to 4.17 ± 0.13 and 3.89 ± 0.23, respectively. The valences of both Ti and Cr tend to increase with ferrosilite (Fs) content, especially in 14053, where, in early pyroxene (~30 mole % Fs), ~20% of the Ti is trivalent and ~25% of the Cr is divalent. For 14072, most analyses indicate little or no Ti^{3+}, but the two

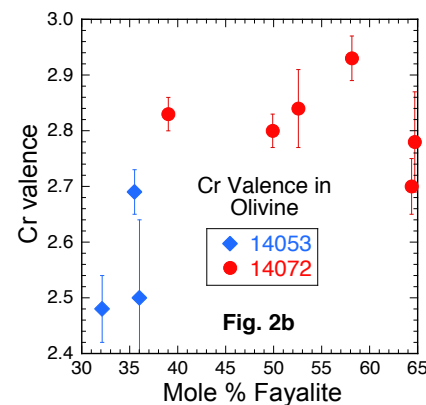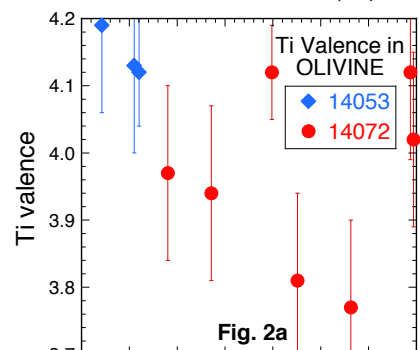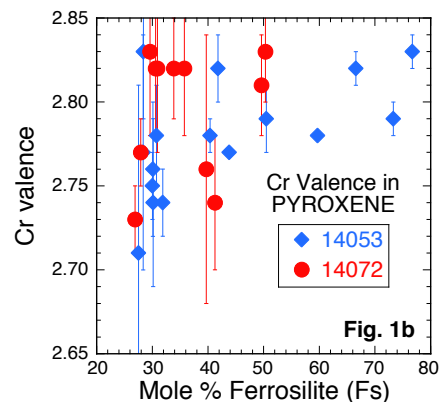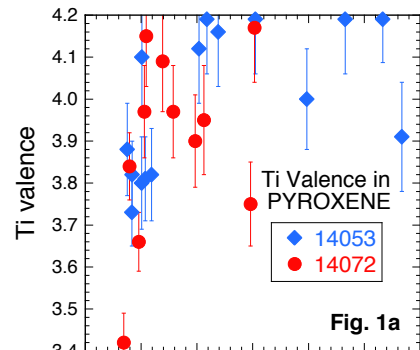most reduced values, 3.42±0.07 and 3.66±0.07, occur in two of the most Fs-poor analysis spots.

Valence of Ti and Cr in olivine. Results are summarized in Fig. 2. Just three analyses were obtained for 14053, all less fayalitic than the olivines analyzed in 14072, and containing no Ti^{3+}. Two of the analyses of olivine in 14072, with valences of 3.77 and 3.81±0.13, have ~20% trivalent Ti and the other five analyses are within error of 4.0. The measurements of Cr valence in 14053 olivine range from 2.48±0.06 to 2.69±0.04, reduced compared to the pyroxene in that sample and compared to both olivine and pyroxene in 14072.

Proportions of Ti in tetrahedral coordination. As in our preliminary study [6] but unlike other previous studies we find significant proportions of the Ti in pyroxene to be in tetrahedral coordination. In 14053 the range is 30-66% and in 14072 it is 20-60%. This component must be considered when interpreting Ti/Al ratios in lunar pyroxene. In 7 of 10 olivine analyses, all of the Ti^{4+} is in tet sites, and two others have ~80%.

Discussion: The pyroxene results indicate that both rocks began crystallizing under conditions where small proportions of the Ti, ~10-20%, and ~75% of the Cr were trivalent. The increase in Ti valence in 14053 seen with continued crystallization could reflect drawdown of highly compatible Ti^{3+} relative to Ti^{4+} in a closed system where redox re-equilibration did not occur. The Cr valence trend (Fig. 1b) reflects the increasingly oxidized conditions. It has been suggested [11] that 14053 underwent subsolidus reduction due to impact heating to 800-900°C that mobilized solar wind-implanted H. Studies of the valence of Ti in equilibrated chondrites [15] indicate that the valence of Ti in pyroxene and olivine is not readily reset by parent-body metamorphism, even to grade 6 (Tmax ~950°C), so it is not surprising that the Ti in 14053 was not strongly reduced by the impact event. On the other hand, Cr exsolves from olivine at the very onset of chondrite metamorphism [15], possibly forming new phases and changing valence states. It is thus possible that the valences of Cr and V in olivine in 14053, reduced compared to those in 14072, were affected by the event that gave rise to the reduced assemblages observed in 14053 [11].

References: [1] Weill D. et al. (1971) *PLSC 2nd*, 413-430. [2] Papike J. et al. (1998) *RiM 36*, 7-1 – 7-11. [3] Burns R. et al. (1973) *PLSC 4th*, 983-994. [4] Sung C-M. et al. (1974) *PLSC 5th*, 717-726. [5] Cohen A. (1973) *LS IV*, 151–153. [6] Simon S. et al. (2014) *LPS XLV*, Abstract #1063. [7] Dowty E. and Clark J. (1973) *Am. Min. 58*, 230-242. [8] Farges F. et al. (1997) *Phys. Rev. B*, 56, 1809-1819. [9] Sutton S. (2005) *GCA 69*, 2333-2348. [10] Bell A. et al. (2014) *Am. Min. 99*, 1404-1412. [11] Taylor L. A. et al. (2004) *Am.*

Min. 89, 1617-1624. [12] Neal C. and Kramer G. (2006) *Am. Min. 91*, 1521-1535. [13] Meyer C. (2011) *Lunar Sample Compendium*. [14] Haggerty S. (1977) *PLSC 8th*, 1809-1829. [15] Simon S. et al. (2015) *LPS XLVI*. Abstract #2141.

Fig. 1a — Ti Valence in PYROXENE

Fig. 1b — Cr Valence in PYROXENE

Fig. 2a — Ti Valence in OLIVINE

Fig. 2b — Cr Valence in Olivine

C³ (C-CUBED): A CONSORTIUM OF INSTRUMENTS AND RESOURCES IN CHICAGO FOR NASA-BASED RESEARCH AND EDUCATION.

N. Dauphas[1,2,3], A. M. Davis[1,2,3], R. Yokochi[1], R. A. Mendybaev[1], P. R. Heck[1,3], T. Stephan[1,3], M. J. Pellin[1,2,4], F. M. Richter[1,3], [1]Department of the Geophysical Sciences and [2]Enrico Fermi Institute, The University of Chicago (dauphas@uchicago.edu); [3]Robert A. Pritzker Center for Meteoritics and Polar Studies, The Field Museum of Natural History, Chicago; [4]Materials Science Division, Argonne National Laboratory, Argonne, IL 60439.

Introduction: As analytical capabilities improve, it becomes possible to analyze smaller samples with better precision, allowing to make optimum use of precious meteorites as well as unique samples returned by spacecraft missions, such as lunar rocks by the Apollo and Luna programs, solar wind by Genesis, cometary dust by Stardust, and asteroidal samples by Hayabusa. More asteroidal samples will be returned to Earth in the next 10 years by the OSIRIS-Rex and Hayabusa 2 spacecrafts, which calls for further investment in analytical capabilities to ensure that a solid base of labs will be available to do the measurements that these missions call for.

The Chicago Center for Cosmochemistry (C³) is a consortium of PI-lead research laboratories at the University of Chicago, the Field Museum, and Argonne National Laboratory whose main focus is in the analysis of meteorites, returned samples, and their constituents. As a premier educational institution, The University of Chicago provides training to undergraduate and graduate students in the fields of meteoritics and cosmochemistry. To accomplish those goals, a large range of instruments are used that were mostly purchased and built through the support of NASA and NSF. These comprise, at the University of Chicago: (1) a new FIB/ FE-SEM with a powerful suite of x-ray analytical accessories; (2) a multicollector Nu Noblesse noble gas mass spectrometer; (3) a Neptune MC-ICPMS associated with a state-of-the-art clean laboratory; (4) a Resonance Ionization Mass Spectrometer; (5) an experimental lab to prepare standards and simulate high T-low P conditions relevant to the formation of the Solar System. At the Field Museum, there are a world-class meteorite collection, an SEM, an iCAP Q LA-ICPMS, and a sample preparation and cosmochemistry laboratory. Except for the two SEMs, all other instruments deliver unique capabilities for analysis, but require significant training in their use and sample preparation. Such training is uniquely available within the C³ environment.

Below, we present in more detail the analytical capabilities of the C³ instruments, all of which are already available for external use on a collaborative basis and some of which could be part of a newly defined facility that would provide a palette of analytical options, from routine SEM measurements to more dedicated research instrumentation.

Laser ablation MC-ICPMS lab for high precision isotopic and elemental analyses: A Thermo Neptune Multi-Collector Inductively Coupled Plasma Mass Spectrometer (MC-ICPMS) is installed in the Origins Lab. It has been upgrade with a Jet Pump, bringing it to specs with the Neptune Plus. Much of the art and time in MC-ICPMS measurements is in sample preparation and wet chemistry. Sample preparation and element purification is done in a large, state-of-the-art clean lab associated with the mass spectrometer. An automated Pneumatic Fluoropolymer HPLC system (patent pending) was developed that streamlines sample processing and improves chemical separation purity and yield. Approximately half of the time on the MC-ICPMS instrument is devoted to objectives relevant to NASA, such as rock dating, cosmic ray irradiation history, chemical and isotopic characterization of extraterrestrial samples. A significant fraction is done through collaboration with outside users. Many students at all levels are involved in this research. The instrument can also be connected to an Excimer laser ablation system.

CHILI, for isotopic and chemical analyses of small samples: The Chicago Instrument for Laser Ionization (CHILI) is a resonance ionization mass spectrometry (RIMS) instrument with unprecedented analytical capabilities. Designed for high lateral resolution (~10 nm), high sensitivity (~40 % useful yield), it is especially suited for the analysis of isotopes of up to three elements simultaneously in μm- and sub-μm-sized samples [3]. After several years of designing and building CHILI, the first analyses of natural samples, Sr, Zr, and Ba isotope studies of presolar SiC grains, were presented last year [4]. It is expected that CHILI will reach its design specifications within this year, and Fe and Ni isotopic measurements on natural samples are underway. CHILI is a unique instrument with capabilities not duplicated at any other cosmochemistry laboratory world-wide. At Argonne National Laboratory, there are two older-generation RIMS instruments, CHARISMA and SARISA, which have been used for presolar grain measurement and analysis of Genesis samples.

Noble gas lab: A multi-collector Noblesse noble gas mass spectrometer (Nu Instruments) is equipped with a dedicated gas purification vacuum line, and a resistance furnace that is used for releasing noble gases from meteorite samples. This facility can analyze noble gas abundances and isotopic compositions at high sensitivity and accuracy.

Experimental lab for modeling evaporation and crystallization processes and for preparation of standards for high precision isotopic analyses: Currently, the lab is equipped with a high-temperature vacuum furnace and one-atmosphere vertical DelTech and Carbolite furnaces. The vacuum furnace is a unique facility that is not replicated anywhere else in NASA or university laboratories in the US. It is used to model chemical and isotopic fractionations during evaporation of refractory CAI-like materials under low-pressure conditions. We are also planning to convert the Carbolite furnace into a low-pressure hydrogen furnace to better reproduce solar nebula conditions. One of our DelTech furnaces is equipped with a gas-mixing apparatus to model melting and crystallization processes in a wide range of redox conditions.

The furnaces are also used to prepare synthetic standards of glasses and minerals that are used as: a) matrix correction standards with the same isotopic but different chemical compositions, as required for high precision isotopic measurements using laser-ablation MC-ICPMS and SIMS instruments [1, 2]; b) standards with the same chemical but varying isotopic compositions to check for possible instrumental mass fractionation effects in some machines.

FIB-SEM at the University of Chicago for petrographic, chemical characterization and sample preparation: A Tescan LYRA3 focused ion beam (FIB)/field emission scanning electron (FE-SEM) microscope was installed in 2015. It is equipped with an Orsay Physics Cobra Ga^+ ion gun, a Schottky field emission gun, a secondary electron detector, a TV-rate backscattered electron detector, in-column secondary and backscattered electron detectors and a STEM (scanning transmission electron microscopy detector). FIB liftout is enabled with an Oxford OmniProbe 400 micromanipultator and OmniGIS II gas injector capable of depositing C, Pt, or W and etching with water or XeF_2. The instrument also has several microanalysis accessories, including two XMax 80 mm^2 silicon drift x-ray detectors, one Wave 500 wavelength-dispersive spectrometer, and a NordlysMax^2 electron backscatter diffraction (EBSD) detector, all from Oxford Instruments and run under their AZtec platform. The instrument is capable of a wide variety of sample preparation and analysis tasks, including liftout and thinning of samples for TEM, fast chemical mapping, quantitative

chemical analysis and determination of crystal structure in both reflection and transmission modes. This facility was largely funded by NASA and is operated as a facility open to users within and outside the University of Chicago, with priority being given to NASA-supported research.

Meteorite Collection, Cosmochemistry Lab, SEM, and Q ICPMS at the Field Museum for sample preparation, petrographic and chemical characterization: The Field Museum houses the largest meteorite collection at a private research institution. It is conveniently accessible in particular for Chicago-based researchers, and a portion of the collection that comprised the research collections of E. Anders and R. N. Clayton remains in residence at the University of Chicago for ready access for teaching purposes. A cosmochemistry laboratory allows sample preparation for different analytical techniques, including SEM, RIMS, SIMS, and atom probe in a clean environment.

The Zeiss Evo 60 SEM is equipped with a state-of-the-art X-Max silicon-drift EDS detector and AZtec software from Oxford Instruments. The setup allows large area mapping with phase identification, automatic particle analysis and quantitative elemental analysis with a large set of standards.

In addition, a state-of-the-art Thermo Fisher Scientific iCAP Q ICMPS was recently acquired with NSF- and private funding and can be used for trace element analysis of extraterrestrial samples. It is equipped with laser ablation, an adaptable chamber for oversized objects, and a nanoparticle analysis system.

References: [1] Janney P. E. et al. (2011) *Chem. Geol., 281,* 26–40. [2] Knight et al. (2009) *GCA, 73,* 6390–6401. [3] Stephan T. et al. (2014) *LPS 45,* #2242. [4] Stephan T. et al. (2015) *LPS 46,* #2825.

REFRACTORY LITHOPHILE ABUNDANCE PATTERNS: THE DEVIL IS IN THULIUM. N. Dauphas[1],
A. Pourmand[2], J.-A. Barrat[3], [1]Origins Lab, Department of the Geophysical Sciences and Enrico Fermi Institute, The
University of Chicago (dauphas@uchicago.edu), [2]Neptune Isotope Lab, Department of Marine Geosciences, University of Miami – RSMAS, Miami, [3]Université de Bretagne Occidentale, Institut Universitaire Européen de la Mer,
CNRS UMR 6538, Plouzané, France

Introduction: Refractory lithophile element
(RLE) abundances are often assumed to be in CI chondrite-porportions among different chondrite groups and
planetary bodies. While this is demonstrably true at the
~10% level, discerning non-chondritic abundance patterns is challenging because planetary processes such
as parent-body metamorphism, alteration, and igneous
processes have oftern fractionated RLEs from one another. Testing this question has important ramifications
as many refractory lithophile pairs, such as Sm-Nd and
Lu-Hf, are decay systems routinely used to date early
solar system events. In addition, fractionation of RLEs
in bulk planetary bodies can provide clues on the nebular processes that governed the composition of planets.
These processes could have involved decoupling between gas and dust after the most refractory elements
had condensed.

A challenge to testing the assumption that RLEs
are in constant proportions is that some chondrites contain large refractory inclusions that are heterogeneously distributed. Equally important is the redistribution of
some of those elements among secondary phases that
formed during parent-body aqueous alteration and
metamorphism.

The rare earth elements (REEs) form a group of
relatively uniform behavior during aqueous, metamorphic, and igneous processes. Exceptions are Ce and Eu,
which also exist as 4+ and 2+ ions while other REEs
maintain their 3+ state. Nebular processes can, however, fractionate REEs from one another in unique ways
that do not necessarily follow any smooth trend with
mass [1,2]. This is most clearly manifested in fine
grained Calcium-Aluminum Inclusions (CAIs) with
type II REE patterns. These objects show depletions in
ultrarefractory heavy REEs (except Tm and Yb) and
volatile REEs (Eu and Yb), while REEs of intermediate volatilities are a uniformly enriched (*i.e.,* Tm and
light REEs except Eu). It remains uncertain what phase
sequestered ultrarefractory REEs but it could have
been hibonite of Ca,Ti-perovskite. it is also not clear
whether such fractionations are present in bulk planetary bodies, in part because parent-body processes typically obliterate the fractionation signature associated
with nebular processes [see *e.g.*, 3,4].

In order to test the assumption that RLEs are present in constant relative proportions in planetary bodies, we have measured at the University of Chicago,
the University of Miami and Université de Bretagne

Occidentale the REE abundance patterns of many
chondrites, achondrites, and terrestrial rocks [5,6].

Methods: At the University of Chicago and Miami, the samples were fused with high-purity lithium
metaborate flux. The REEs were then extracted from
the rest of the matrix using the TODGA resin. The
REE measurements were performed on a Thermo Neptune multi-collector inductively coupled plasma mass
spectrometer (MC-ICPMS) [5 and references therein]
in multi-collection, providing high precision on REE
patterns including mono-isotopic REEs such as Tm.
The abundances of mono-isotopic REEs had seldom
been measured prior to the advent of ICPMS because
these were not amenable to isotope dilution mass spectrometry (IDMS) techniques. The measurements at the
Université de Bretagne Occidentale were done completely independently using a separate protocol [6 and
references therein]. The samples were dissolved in acid
and the measurements were then performed on a single
collector high-resolution Thermo Element 2 ICPMS.

Results: There is very good agreement between the
different techniques for the samples that were measured in all three labs. There is also good agreement
between Lu measurements by bracketing with measurements performed earlier on the same samples by
IDMS [7]. The results show significant variations in
REE abundance patterns, even within one chondrite
group. Eu/Eu* anomalies are also variable and tend to
correlate with the extent of LREE/HREE fractionation.
Tm/Tm* anomalies are constant within a group. All
achondrites, terrestrial rocks, enstatite chondrites and
ordinary chondrites display negative anomalies in
Tm/Tm* of -3 to -5% relative to CI chondrites. Other
carbonaceous chondrites show Tm/Tm* anomalies
similar to CI or even larger, reaching +10% in the Allende CV chondrite.

The nugget effect: We focus our discussion below
on ordinary chondrites, as they are characterized well.
Nevertheless, similar issues exist for enstatite and carbonaceous chondrites as REEs tend to be concentrated
in oldhamite and phosphate, respectively, in these meteorite groups. During metamorphism in ordinary
chondrites, REEs that were initially in the chondrule
mesostasis and other phases migrate into Ca-phosphate
minerals, Ca-pyroxene, and plagioclase for Eu. In metamorphosed chondrites, Ca-phosphate show depletion
in HREE because they are also partitioned into pyroxene [4]. Eu that is concentrated in plagioclase also

shows up as a negative anomaly in the Ca-phosphate pattern. Heterogeneous distribution of phosphates should thus be associated with a negative correlation between LREE/HREE fractionation and Eu/Eu* anomalies, as is observed. Using available data on the size and mode of phosphate grains in ordinary chondrites, we calculate that a 85 mg chondrite sample would only contain ~28 phosphate grains of 200 μm size, and the 95% confidence interval for this value is 18 to 39 grains. This nugget effect and the fact that phosphates have fractionated REE patterns explain much of the variations in REE patterns documented in ordinary chondrites. To evaluate this more quantitatively, we derived an equation that gives the dispersion (σ_R) on an elemental or isotopic ratio ($R = C_2/C_1$) arising from the nugget effect,

$$\sigma_R \simeq$$

$$\frac{r(\rho_{nugget}/\rho_{matrix})}{[1+rf(\rho_{nugget}/\rho_{matrix})]^2}\sqrt{\frac{f\rho_{matrix}\pi d^3}{6m}}\left|R_{nugget} - R_{matrix}\right|,$$

where r is the ratio of concentrations $C_{1,nugget}/C_{1,matrix}$, m is the mass homogenized, and d is the size (diameter) of the nugget grains. We applied this equation to ordinary chondrite and found that it does explain the dispersion in La/Lu, $^{176}Hf/^{177}Hf$ and Eu/Eu* measured in ordinary chondrites, proving that a nugget effect associated with the presence of Ca-phosphate is responsible for the variations. A diagnostic signature of this effect is the presence of large and variable Eu/Eu* anomalies. To account for this, we have filtered all the data to retain patterns that have Eu/Eu* within 5% of the CI value. The patterns seen in all chondrite groups after such filtering are approximately parallel, demonstrating that to the first order, the REEs are present in chondritic proportions among planetary bodies (Fig. 1 [5]).
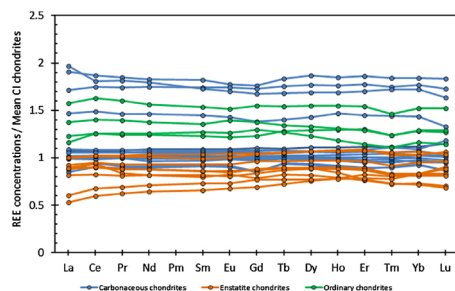
Fig. 1. REE patterns of all the chondrite samples with Eu/Eu* anomalies within 5% of the CI value [5].

Thullium anomalies: A characteristic feature of type II REE patterns most commonly found in fine grain CAIs is the presence of a large positive Tm anomaly. This arises from the fact that other REEs surrounding Tm are either more volatile (Yb) or more refractory (other HREEs) than Tm. ICPMS instruments allow one to measure the abundance of mono-isotopic Tm with a precision that was unachievable with previous techniques. Our results show that the Earth, Mars, the Moon, Vesta, ordinary chondrites, enstatite chondrites, and achondrites, all exhibit negative Tm/Tm* anomalies relative to CI. Carbonaceous chondrites show no or positive anomalies [5,6]. The measurements agree between Chicago, Miami, and Brest and they also agree with independent measurements by [8].
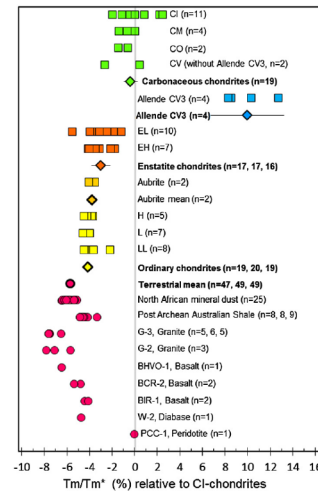
Fig. 2. Tm/Tm* anomalies in chondrites and terrestrial rocks [5]. Note that the variations in Tm/Tm* is explained by the fact that some of those rocks have strongly fractionated REE patterns, whose curvature introduce an artifact in the calculation of Tm/Tm*. Using a more sophisticated definition of Tm/Tm* removes this artifact [5,6].

This is interpreted to reflect the fact that CIs incorporated an extraneous 0.15% of refractory dust similar in composition to fine grain CAIs with the type II pattern. Allende, with its large +10% excess in Tm must have incorporated an extra 0.35% type II dust in addition to what CIs contained. These results demonstrate that at a fine level, all refractory lithophile elements are not present in CI proportions in all planetary bodies; the devil is in Tm.

References: [1] Boynton W. V. (1975) GCA 39, 569. [2] Davis A. M. and Grossman L. (1979) GCA 43, 1611–1632. [3] Murrell M. T. and Burnett D. S. (1983) GCA 47, 1999. [4] Crozaz G. et al. (1989). EPSL 93, 157. [5] Dauphas N., Pourmand A. (2015) GCA 163, 234. [6] Barrat J.A. et al. (2016) GCA 176, 1. [7] Dauphas N. and Pourmand A. (2011) Nature 473, 489. [8] endel V., Pack A. and O'Neill H. (2012) LPSC 43, #2578.

DOUBLE-SPIKE DATA REDUCTION IN THE PRESENCE OF ISOTOPIC ANOMALIES. J.Y. Hu[1] and N. Dauphas[1], [1]Origins Laboratory, Department of the Geophysical Sciences and Enrico Fermi Institute, The University of Chicago, Chicago IL.

Introduction: Isotopic analyses of planetary materials provide insights into the natural processes that govern those variations, such as evaporation/condensation in the nebular, metamorphism, and igneous processes in planets and meteorite parent bodies. Those measurements can be performed by either TIMS or MC-ICPMS. A challenge to isotope analysis is to distinguish per-mil level natural fractionation from even larger instrumental mass bias. This problem can be solved by using the double-spike technique for elements with four or more isotopes [1]. Through double-spike technique, true isotope ratios can be inverted mathematically by analyzing a mixture of sample and spike solution. However, implementation of the double-spike technique is hindered by several difficulties including 1) determination of spike composition and sample/spike proportion, 2) double-spike calibration and, 3) tedious data inversion. On the other hand, the sample-standard bracketing (SSB) method provides comparable precision with a simpler protocol for isotope analysis. In the SSB method, mass bias of samples is assumed to be similar to that of standards. However, the SSB method is not a silver bullet for isotope analysis. Its robustness lies in the stability of plasma source mass spectrometers (*e.g.* MC-ICPMS) and similarity of sample and standard. Therefore, the SSB method is sensitive to the status of mass spectrometers and vulnerable to mismatched concentration and matrix effect. Mass bias correction in the SSB method is limited to instrumental measurement and consequently requires 100% yield in chemical purification.

In contrast, double-spike does not require as high yield and purity as the SSB method and is gaining traction in isotopic analysis by MC-ICPMS [2]. A critical assumption of the double-spike data reduction is the mass-dependent relationship between standards and samples. Uncorrected isotopic anomalies will affect the accuracy of double-spike reduction. The influence of isotopic anomalies can be corrected numerically [3]. Here we present an analytical method to correct isotopic compositions determined by the double-spike technique for the presence of isotopic anomalies. The true isotopic ratio can be obtained through a simple correction of the routine double-spike data reduction algorithm that assumes terrestrial mass dependent fractionation. We focus below on an application to Mo. Details on the formalism will be presented in the conference and will follow in a forthcoming publication.

Double-spike with Mo anomalies: Molybdenum is a refractory and moderately siderophile element. Substantial mass-dependent isotopic fractionation of Mo has been reported in the solar nebular and during planetary differentiation [4, 5]. Mo isotopic composition in bulk meteorites can be interpreted as a mixture of a terrestrial source and an *s*-depleted source [3]. Therefore, Mo nucleosynthetic anomalies are correlated with each other. Burkhardt et al. (2014) modeled the effects of nucleosynthetic anomalies (Table S2 in Burkhardt et al., 2014) and obtained a relationship between the size of the anomaly and the correction in the double-spike data reduction. From the numerical test, Burkhardt et al. (2014) obtained a parameterized relationship:

$$\delta^{98/95}Mo_{corrected} = \delta^{98/95}Mo_{measured} - \varepsilon^{96/95}Mo_{nucleosynthetic} \times 0.066 \quad (1)$$

Where $\varepsilon^{96/95}Mo_{nucleosynthetic}$ is the nucleosynthetic anomaly normalized to $^{97/95}Mo$. We tested our analytical method with the simulated data presented in Table S2 in Burkhardt et al. (2014) and obtained the following relationship

$$\Delta^{98/95}Mo = 0.0304\varepsilon^{97/95}Mo + 0.1136\varepsilon^{98/95}Mo - 0.0206\varepsilon^{100/95}Mo \quad (2)$$

Where $\Delta^{98/95}Mo$ is the correction that needs to be applied if one does the data reduction blindly, not accounting for the presence of isotopic anomalies (i.e., δ_{true}-δ_{calc}). The correction given by Eq. 2 is consistent with the simulated data in Burkhardt et al., (2014) (Table 2). Based on correlations of anomalies on different isotopes, a formula similar to Eq. 1 can be derived

$$\delta^{98/95}Mo_{corrected} = \delta^{98/95}Mo_{measured} - \varepsilon^{96/95}Mo_{nucleosynthetic} \times 0.070 \quad (3)$$

As shown in Table 1, the analytical approach accurately corrects the synthetic compositions for the presence of anomalies.

Table 1

$\delta^{98/95}Mo$	SRM 3134 Mo	-0.005%s[a]	-0.01%s	-0.05%s
δ by anomalies[b]	0	-0.06	-0.12	-0.60
δ to be corrected[c]	0	0.06	0.12	0.60

[a] Deficit of *s*-process Mo in synthetic composition

[b] Apparent fractionation induced by nucleosynthetic anomalies

[c] Applicable correction

Conclusion: We introduce an analytical formula that allows one to apply a uniform double-spike data reduction to all samples regardless of the presence of isotopic anomalies. One can assume mass-dependent relationship with terrestrial composition to calculate the double-spike corrected values. Our formula gives

the correction that one needs to apply to account for the presence of isotopic anomalies. This is useful when investigating stable isotopic fractionation in extraterrestrial samples where isotopic anomalies are ubiquitous.

References: [1] Dodson (1963) *JSI* 40.6, 289. [2] Millet and Dauphas (2014) *JAAS* 29.8, 1444-1458. [3] Burkhardt et al. (2014) *Earth Planet. Sci. Lett.* 391, 201-211. [4] Dauphas et al. *Astrophys. J. Lett.* 569, L139-L142. [5] Hin et al. (2013) *Earth and Planet. Sci. Lett.* 379, 38-48.

CADENCE AND CAUSE OF LAKE-FORMING CLIMATES ON MARS.

Edwin S. Kite[1], John Armstrong[2], Colin Goldblatt[3], Peter Gao[4], David P. Mayer[1]. [1]University of Chicago (kite@uchicago.edu), [2]Weber State University, [3]University of Victoria, [4]Caltech.

The problem: Many models give an account of how Early Mars' *mean state* approached the melting point, but all have trouble matching the constraints on the *time-variability* of climates that permitted precipitation-fed lakes - their number, duration, and spacing.
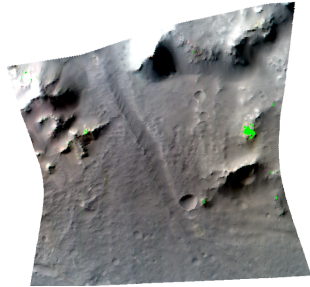
Fig. 1. The olivine constraint. An olivine outcrop in an alluvial fan source region (fan drains to bottom of image). Olivine detections highlighted in green. CRISM FRT00016E79, Saheki crater.

Some deltas (e.g. Eberswalde), and all large alluvial fans, had a top-down water source (rain or snowmelt). Hydrologic constraints suggest Lake Eberswalde lasted 10^4-10^6 yr [1]. Alluvial-fan volume and facies suggest >3 km column runoff [2], requiring >10^4 yr runoff in a snowmelt climate. Olivine dissolves in <10^7 yr for Mars-relevant conditions [3], but olivine is found in both the source regions (plus adjacent plateaus) and the deposits of post-Noachian Mars rivers (e.g. Fig. 1). After sediment transport ceased, subsequent soil-wetting events were insufficient to dissolve all the olivine. Many sites show two generations of river valleys [e.g. 4]. Crisp banks are seen on young valleys, but older valleys have subdued banks. This suggests a long interval of diffusive bank-softening between valley-forming events. The rarity of late-stage incision into delta deposits and the rarity of embedded craters within alluvial fans suggest fan deposition was completed in <10^8 yr, with little or no reactivation. These data suggest that post-Noachian lake-forming climates were (a) widely separated in time, (b) lasted >10^4 yr individually, (c) were few in number but (d) cumulatively lasted <10^7 yr (to allow olivine to survive globally). What model can match these constraints?

How well do proposed triggers of lake-forming climates match cadence constraints?: Wetting the soil (dissolving olivine) requires much less rain/melt than sediment transport by runoff (because of refreezing and infiltration). If the atmosphere was thin, and wetting was due to snowmelt, then runoff requires ~50 W/m^2 more energy than does soil wetting. This large energy gap, plus the olivine constraint and the lake-lifetime constraint, together imply that the post-Noachian climate system was below the melt threshold in most times and places,

but when it was above the melt threshold it was also above the sediment-transport threshold for a surprisingly large fraction of that time. A baseline of warming can be provided by long-lived greenhouse gases such as CO_2(+/-H_2), supplemented by cloud and $H_2O_{(v)}$ feedbacks [5-7]. However, long-lived forcings cannot be solely responsible for lake-forming climates, because this would violate the olivine constraint. Possible triggers for lake-forming events are impacts, volcanic SO_2, solar brightening, tidal breakup of a low-albedo moon, and orbital variability. SO_2 warming struggles to match the minimum-duration constraint [8]. Post-Noachian impacts usually had subdued local hydrologic response, so why would they have a global response [9]? Cirrus-warming can be a positive feedback on orbital forcing, or indeed on any trigger [6]. It is not clear what would halt metastable H_2O-supported climates (whose existence is model-dependent); if the duration of metastable climates is set by H_2 escape at current (slow) rates [10], then metastable wet climates would last too long to match the olivine constraint. Groundwater-outburst floods have the right cadence to match cadence constraints on the triggers of lake-forming climates, but $H_2O_{(v)}$ released by outbursts is cold-trapped close to source and does not affect global climate [11,12]. CO_2 release during outburst floods is probably unimportant [13]. Is there an alternative scenario that better matches the data?
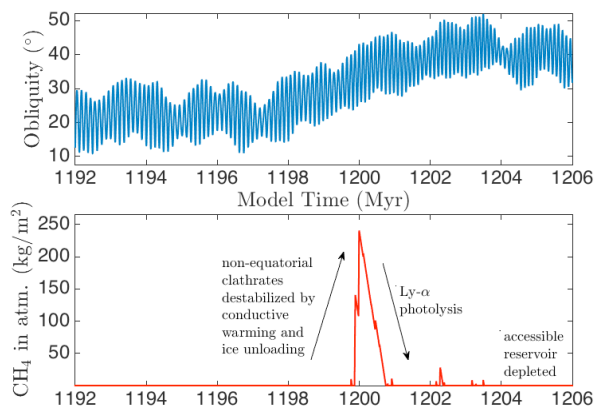
Fig. 2. (Preliminary) CH_4-release scenario, driven by orbital forcing from one of our 912 possible histories. Ice-load removal drives the main release pulse, with heating dominant for later minor pulses.

Can variable lake-forming climates be triggered by orbital variability?: The main driver of climate variability on 10^2-10^7 year timescales on Amazonian Mars is thought to be orbital forcing, so perhaps the main driver of climate variability on these lake-hydrology-relevant timescales on Early Mars was also orbital forcing.

To test this, we calculated ~4 trillion years of Mars obliquity/eccentricity/longitude-of-perihelion (912 randomly-initialized runs each >3.5 Gyr long), using `mercury6` and J.C. Armstrong's obliquity code. Including solar brightening, the annual-maximum insolation that is exceeded (somewhere) for 10^7 yr tends to be <50 W/m^2 below the overall-maximum insolation. Therefore, the hypothesis that direct forcing by orbitally-driven insolation is solely responsible for the variability of lake-forming climates is in tension with the olivine constraint.

The *transitions* in mean (10^6-yr averaged) obliquity, ϕ, are more attractive as a candidate trigger for lake-forming climates. ϕ transitions last a few Myr, and are remarkably rare (it is a coincidence that a ϕ transition occurred only ~5 Mya) [14,15]. To illustrate this, set the boundary between high ϕ and low ϕ at 40° (about the threshold for equatorial vs. non-equatorial surface ice). Then, time-travelling to a random point in Mars' history, one would expect to find oneself in an interval of continuously high (or low) ϕ of 800 Myr duration. If Early Mars lasted ~1 Ga, then the median number of ϕ transitions is 1. Two or fewer ϕ transitions occur for 72% of "Early Mars" instantiations. The brevity and large time interval of ϕ transitions make them an attractive trigger for rare lake-forming climates. But what mechanism could link ϕ transitions to lake-forming climates?

Mechanism #1: Methane bursts: CH_4 stored in clathrates is quickly released by warming [26] and decompression when ice cover migrates subsequent to obliquity shift. Although CH_4 is irreversibly destroyed by photolysis, this is photon-limited at high CH_4 concentration. This might permit a CH_4 boost to the greenhouse effect lasting >10^5 yr, provided >1 mbar of CH_4 ($\equiv$ 20 cm global-equivalent layer of clathrate) destabilized in <10^5 yr. A low-to-high shift in ϕ warms and depressurizes (via ice-overburden removal) shallow-subsurface clathrates poleward of ~30°. A preliminary calculation is shown in Fig. 2. (CH_4 can also be quickly released by a groundwater outburst [19].) Assuming that snow/ice is just below the melting point in the absence of CH_4, long-wave radiative forcing from CH_4 in CO_2-dominated atmospheres can exceed 25 W/m^2 [16]. This gives 300 m^3 km^{-2} hr^{-1} meltwater, well within the range of runoff estimates for river-forming climates [17]. With $H_2O_{(v)}$ and cirrus feedback, discharge increases. Therefore, CH_4 release could in principle trigger a lake-forming climate. In this scenario, the cold shallow subsurface acts as a capacitor for CH_4 (ultimately sourced from water-rock reactions). The greenhouse-warming potential is released in one-to-a-few bursts in Mars' past, and the clathrate reservoir is almost all depleted today. Mechanism #1 can be tested by photochemical modeling of CH_4 oxidation in a water-rich atmosphere, as well as by geologic assay of the number of lake-forming events (which cannot exceed a few in this scenario).

Mechanism #2: $H_2O_{(v)}$ feedbacks on a planet with more H_2O: Mars had ~3× more H_2O ~3 Gya [27]. Adding H_2O does not directly cause a wet Mars surface: the "extra" ice piles up at cold traps, still frozen [22,23]. However, adding H_2O can indirectly cause a wet Mars surface. For example, a thicker ice cap requires more time to completely shift from the pole to the equator. This increased time delay implies that, during rare shifts from low ϕ to high ϕ, ice at the pole can persist to higher obliquity. Therefore, the peak water vapor pressures above the pole are higher [9]. Direct $H_2O_{(v)}$ radiative forcing, plus cloud feedbacks, then warm the planet. Once all the ice has shifted to the equator (10^5 yr?), or retreated beneath $\gg$1 m sublimation/debris lag, the lakes dry out. #1 and #2 predict geologically-simultaneous discharge from destabilized groundwater reservoirs [20].

Mechanism #3: Late-stage carbonate formation: A climate evolution model for Mars with only CO_2, surface snow/ice, and solar brightening, can produce late bursts of habitable climate on Mars – the trigger is late low-to-high ϕ shifts. Rapid CO_2 removal could end the wet burst, by increasing evaporitic cooling [24]. CO_2 removal by (post-Noachian) escape-to-space processes cannot remove climatically significant CO_2 in 10^7 yr. CO_2 removal by carbonate formation can end the wet episode more quickly. The amount of CO_2 that must be sequestered is >20 mbar. The only sufficiently voluminous and sufficiently young reservoir for carbonate is the dust-covered "rhythmite" rocks [25]. If late-stage carbonate formation is responsible for the end of lake-forming climates on Mars, then "rhythmite" must contain several wt% carbonate. "Rhythmite" is exemplified by the upper mound in Gale. Therefore, nondetection of carbonate in the upper mound would disprove mechanism #3. This test requires that MSL is driven at least as high as the major unconformity marking the boundary between the Lower and Upper formations at Mt. Sharp.

References: [1] Irwin et al. (2015) *Icarus* [2] Williams et al. (2011) *Icarus* [3] Olsen & Rimstidt (2007) *Am. Min.* [4] S.A. Wilson et al. (2014) *AGU Fall Meeting* [5] Mischna et al. (2013) *JGR-E* [6] Urata & Toon (2013) *Icarus* v.226 p.229 [7] Batalha et al. (2015) *Icarus* [8] Kerber et al. (2015) *Icarus* [9] Irwin (2013) *LPSC* [10] Segura et al. (2012) *Icarus* [11] Kite et al. (2011) *JGR-E* E10002 [12] Turbet et al. (2015) *LPSC* [13] Forget et al. (2013) *Icarus* [14] Laskar et al. (2004) *Icarus* [15] Lissauer et al. (2012) *Icarus* [16] Byrne & Goldblatt (2014) *Climate of the Past* [17] Irwin et al. (2005) *Geology* [18] Baker et al. (1991) *Nature* [20] Scheidegger & Bense (2014) *JGR-F* 2014 [21] [22] Kite et al. (2013) *Icarus* [23] Wordsworth et al. (2015) *JGR-E* [24] Hecht (2002) *Icarus* [25] Grotzinger & Milliken (2012) pp.1-48 in *"The sedimentary rock record of Mars"* SEPM [26] Root & Elwood-Madden (2012) *Icarus* [27] Mahaffy et al. (2015) *Science*.

THE TITANIUM ISOTOPIC COMPOSITIONS OF CHONDRITES AND EARTH

N.D. Greber[1,*], N. Dauphas[1], M.A. Millet[2] and I.S. Puchtel[3], [1]Origins Laboratory, Department of the Geophysical Sciences and Enrico Fermi Institute, The University of Chicago, Chicago, IL 60637, USA; [2]Durham University, Department of Earth Sciences, South Road, Durham DH1 3LE, UK; [3]Department of Geology, University of Maryland, College Park, MD 20742, USA, *corresponding author, greber@uchicago.edu

Introduction: Due to its lithophile and strongly refractory character, Ti is an element of particular interest in planetary sciences as the range of processes susceptible of fractionating its isotopic composition is rather limited and involves primarily magmatic/metamorphic processes. Indeed, Ti is refractory and cannot easily be lost during impact heating, it is lithophile meaning that core partitioning is irrelevant, and it is fluid immobile, meaning that it is immune to parent-body alteration.

Here, we present first Ti isotope data for chondritic meteorites and komatiites and discuss and summarize the current state of knowledge for this promising new isotope system.

Methods: Samples analyzed in this study have been digested using the $LiBO_2$ fusion technique, which, unlike the more conventional acid digestion technique, affords complete dissolution of refractory accessory minerals and it avoids the creation of insoluble Ti-bearing fluoride. As a test, several samples were also digested using the conventional high-temperature acid attack. Chemical purification and Ti isotope measurements using a ^{47}Ti-^{49}Ti double spiking procedure were done following published methodology [1]. This separation guarantees proper removal of Li, which may cause ArLi molecular interferences on masses ^{46}Ti and ^{47}Ti.

All measurements were corrected for the presence of ^{47}Ti and ^{49}Ti isotopic anomalies (^{50}Ti is not used for isotope reduction procedure) based on the published values [2]. The Ti isotope composition is expressed in the delta notation (i.e. $\delta^{49}Ti$) relative to the $^{49}Ti/^{47}Ti$ isotope ratio. The 2SD uncertainty on the standard measurements during each analytical session was always below ±0.035‰, and this value served as a measure of external precision of the isotopic analysis, unless stated otherwise.

Samples: To date, 13 chondritic meteorites have been analyzed for their Ti isotopic composition; these included the CO, CM, EC, LL, L, and H groups of chondrites. In addition, three USGS standard reference materials (SRM) (BHVO-2; BIR-1a, and G3) and Archean komatiites from four different localities were also analyzed for their Ti isotope compositions. This included komatiites from the 3.55 Ga Schapenburg, 3.48 Ga Komati, 3.26 Ga Weltevreden, and 2.72 Ga Alexo komatiite systems. For all four localities, sets of samples that included both olivine cumulates and spinifex-textured rocks, were analyzed for their $\delta^{49}Ti$.

Results: The Ti isotope compositions obtained by both digestion techniques are identical within the respective uncertainties, indicating that the flux fusion technique yields accurate results. The measured Ti isotope composition of the USGS SRM BHVO-2 ($\delta^{49}Ti = 0.009 \pm 0.035$‰) and BIR-1a ($\delta^{49}Ti = -0.062 \pm 0.035$‰) are identical to our previous measurements [1]. The $\delta^{49}Ti$ of the USGS SRM G3 is +0.412 ± 0.035‰ and is, thus, significantly heavier than that of the other two SRMs.

The $\delta^{49}Ti$ values of all chondrites are indistinguishable within uncertainty, ranging from -0.027‰ (Bald Mountain, L4) to +0.027‰ (Blithfield, EL6) with a mean value of 0.004 ± 0.010‰ (95% c.i, n=13; Fig. 1). The Komati and Schapenburg komatiites have an average $\delta^{49}Ti$ that is identical to that of chondrites, while the Weltevreden and Alexo komatiites have slightly lighter Ti isotope compositions (Fig. 2).
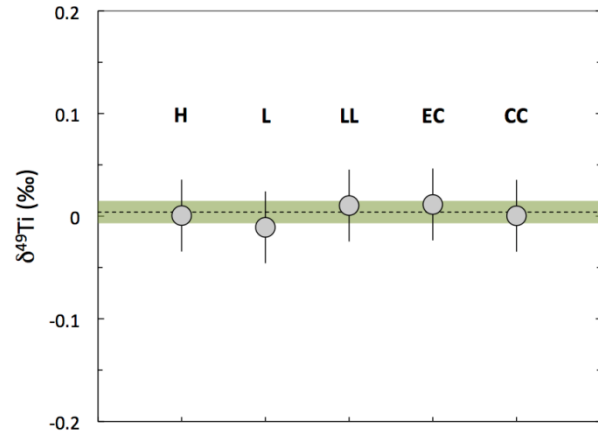

Figure 1: Ti isotope composition of the different chondrite groups analyzed. All $\delta^{49}Ti$ are identical within the uncertainty, averaging at +0.004 ± 0.010‰ (95% c.i.) relative to Chicago-Ti standard. CC includes CM and CO chondrite groups.

Discussion: The similarity in the Ti isotope composition among all investigated chondrite groups indicates the absence of Ti isotope fractionation during accretion on a bulk planetary scale, at least for the samples investigated. In addition, the average chondritic $\delta^{49}Ti$ is identical to the recent estimate of the bulk silicate Earth [1]. Due to the lithophile character

of Ti, these results show that the bulk silicate Earth has a chondritic mass-dependent Ti isotope composition.

Calcium is an element with a similar refractory and lithophile character as Ti and recently published data revealed that the Ca isotope compositions of most carbonaceous chondrites (except CO) are lighter than that of the bulk silicate Earth, ordinary and enstatite chondrites [3]. Our preliminary measurements of CM chondrites indicate that they have Ti isotope composition similar to the bulk Earth and all the enstatite and ordinary chondrites. Further work is needed to test whether other carbonaceous chondrites also have indistinguishable Ti isotopic composition as Earth. A possible reason why carbonaceous chondrites have light Ca isotopic composition is that they incorporated a greater proportion of refractory dust, which carries a very light Ca isotopic signature, reaching -5 ‰ [4]. Such a signature was found in the abundance of the REEs in the form of a Tm excess in carbonaceous chondrites relative to other meteorite groups, Earth, Mars, and Vesta [5,6]. CAIs also have fractionated δ^{49}Ti [7] but the fractionations are on both sides of the terrestrial composition and have on average a δ^{49}Ti isotopic value (around 0.22 ‰) that is not very different from the terrestrial value. Thus, while the greater incorporation of refractory dust in carbonaceous chondrites may have affected their Ca isotopic composition and REE pattern, such an effect is not necessarily expected for Ti isotopes.
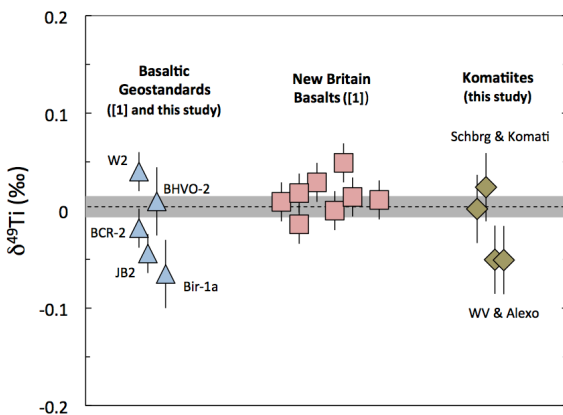
Figure 2: Ti isotope composition of basalts and komatiites. Most samples have Ti isotope compositions that are identical, within uncertainties, to the chondritic δ^{49}Ti (grey bar with dotted line). Schbrg, Schapenburg; WV, Weltevreden

As mentioned earlier, the bulk silicate Earth [1] and chondritic Ti isotope compositions are identical within the uncertainties. However, small deviations from the chondritic δ^{49}Ti towards lighter and heavier Ti isotope compositions are observed for the Alexo and the

Weltevreden komatiites, as well as for some of the Cenozoic basalts (Fig. 2). This implies that some sort of δ^{49}Ti heterogeneity exists in the terrestrial mantle. The solubility of Ti in different mantle minerals changes with pressure [8] and thus, Ti is an element affected by metamorphic reactions occurring in the Earth mantle. The inter-mineral Ti exchange that takes place during such reactions might fractionate Ti isotopes and thus produces variable δ^{49}Ti between different mantle phases. Fractional melting or melting of refractory mantle residues could then lead to the observed δ^{49}Ti variations found in mafic rocks.

While the δ^{49}Ti differences in mafic and ultramafic rocks are rather small, the only granitic rock measured exhibits a pronounced heavier Ti isotope composition. Thus, processes involved in the production of continental crust might favor heavy Ti isotopes [9].

Summary: Ordinary, enstatite and carbonaceous chondrites have uniform mass dependent Ti isotope compositions. The chondritic average is within error identical to the recent estimate for the Ti isotopic composition of the bulk silicate Earth. This indicates insignificant Ti isotope fractionation during accretion processes of planets.

Significant variation in the Ti isotope composition is found among igneous terrestrial rocks. The only granitic sample measured has a pronounced heavier Ti isotope composition than the bulk Earth and chondrites, indicating preferential incorporation of heavy isotopes into Earth's crust.

References: [1] Millet and Dauphas (2014) JAAS 29, 8, 1444. [2] Zhang et al., (2012) Nat. Geosci. 5, (4), 251–255. [3] Valdes et al., (2014) Earth Planet. Sci. Lett. 394, (C), 135–145. [4] Huang et al., (2012), GCA 77, 252-265 [5] Dauphas and Pourmand (2015) Geochim. Cosmochim. Acta 163, 234–261 [6] Barrat et al., (2016) Geochim. Cosmochim. Acta, 176, 1-17 [7] Zhang (2012) Phd Thesis, University of Chicago [8] Zhang et al., (2003) Earth Planet. Sci. Lett. 216, (4), 591–601. [9] Millet et al. (in review) Earth Planet. Sci. Lett.

PACING WIND-INDUCED SALTATION ABRASION ON MARS: USING CRATER COUNTS TO CONSTRAIN AEOLIAN EXHUMATION. David P. Mayer[1] and Edwin S. Kite.[1] [1]University of Chicago (dpmayer@uchicago.edu).

Introduction: To understand Mars landscape evolution we need estimates of surface erosion rates, and how they vary across the landscape. For example, constraints on wind-induced saltation abrasion can test models of past wind shear stresses [1], as well as models of sedimentary-rock mound formation [2,3]. Erosion rates are also needed as inputs to models of organic matter preservation potential [4]. Measurements of the number and diameter of impact craters are essential inputs for estimating erosion rates. Relatively small, shallow craters are preferentially obliterated as a landscape undergoes erosion [5], so the size-frequency distribution of impact craters in a landscape undergoing steady exhumation will develop a shallow power-law slope [6]. Because crater counts require only orbiter data, they enhance the value of rare direct measurements of exposure age from rovers [4].

Here we present preliminary results from our effort to map impact crater frequency in HiRISE image data for sedimentary rocks across Mars (Figure 1). Fast crater-obliteration has been previously reported for Mars sedimentary rocks, but has not been systematically quantified [e.g. 7,8,13,14].

Data and Methods: We used image data from the HiRISE red channel as the basis for crater mapping. Analysts counted craters on selected areas of map-projected HiRISE images using the CraterTools extension for ArcMap [9].
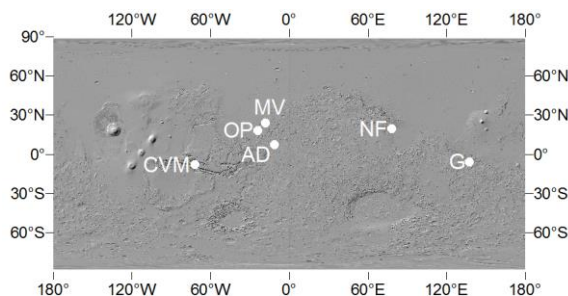
Figure 1. Map showing regions where craters were counted. AD = Aram Dorsum, CVM = Central Valles Marineris, G = Gale Crater, NF = Nili Fossae, MV = Mawrth Vallis, OP = Oxia Planum.

Crater Counting. Analysts (University of Chicago undergraduates) were given 2 hours of classroom training on martian impact crater morphology, with examples primarily drawn from HiRISE image data, followed by ~6 hours of hands-on training mapping impact craters on 2 HiRISE images using ArcMap and CraterTools. Following training, the analysts inde-

pendently mapped craters in pre-selected areas of ~40 HiRISE images. Portions of the images containing dunes or other landforms of apparently unconsolidated material were masked out.
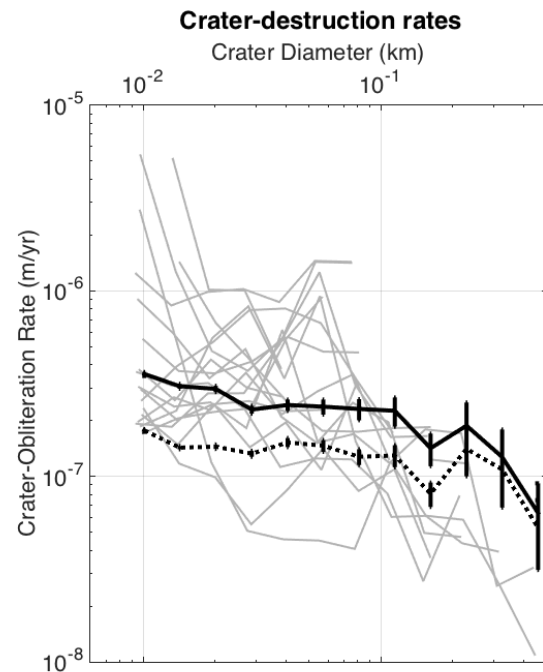
Figure 2: Crater obliteration rates derived from crater counts on HiRISE images. Solid line shows results (and statistical error bars) for craters agreed upon by ≥3 analysts. Dashed line shows results (and statistical error bars) for craters agreed upon by ≥2 analysts; this count includes more false positives. Gray lines show crater obliteration rates for the 18 individual HiRISE images based on craters agreed upon by ≥3 analysts.

Erosion-Rate Estimation. Erosion rates were estimated for areas in HiRISE images in which craters were mapped by ≥3 analysts. For each such image, craters mapped by different analysts were aggregated using a clustering algorithm implemented in Matlab. Overlapping features whose centers were located within 50% of the maximum diameter of one another and whose absolute value of diameter differences were less than 150% were clustered together. Final agreed-upon craters were then defined by the mean center location and diameter of the clustered features. To calculate erosion rates, we used the "1 Ga" flux of craters in Table 1 of Ref. [10]. We then divided our counts (N/km^2) by the fluxes to obtain effective ages of the surface for each size bin. We assumed a resurfacing depth of 10% of

the diameter of the crater is sufficient to obliterate the crater (this is ~50% of original crater depth; if the required resurfacing depth is in fact 100% of original crater depth, then our computed rates increase by a factor of 2). With these assumptions, the mean erosion rate for each size bin equals the depth-to-obliteration divided by the size-bin-specific exposure age.

Preliminary Results:
Impact craters were mapped by ≥3 analysts in 18 HiRISE images showing sedimentary rocks (Figure 1). Most of the images were in areas of steep terrain. The false positive crater identification rate appears to be low based on inspection of agreed-upon craters. Therefore, this gives a lower limit on the "true" number of craters within each mapped area – and thus an upper bound on crater-destruction rate. The crater-obliteration rates we obtain are upper limits on the rate of landscape-wide exhumation (i.e. landscape lowering). For example, craters can be removed by diffusive infilling without landscape-lowering, and diffusion fits crater-degradation observations in the flat landscape of the Burns Formation [5]. For an unusually steep sedimentary-rock outcrop, >1 μm/yr average erosion sustained over 200-400 Myr has been reported by [12]. If the erosion rates are interpreted as landscape-lowering rates, then the mean rates are 0.2-0.4 μm/yr (if craters counted by ≥3 analysts are included) or 0.1-0.2 μm/yr (if craters counted by ≥2 analysts are included (Figure 2); this count has a greater frequency of false positives). Individual images showed crater-obliteration rates that clustered in the range 0.1-1 μm/yr, consistent with [6].

Comparison to Other Methods: Most studies involving crater-counts rely on a single experienced analyst to identify craters. The other endmember is crowdsourcing platforms, such as MoonZoo (http://moonzoo.org) and Cosmoquest (http://cosmoquest.org), which invite the general public to count craters on the Moon and Mars. Robbins et al. (2014) compared lunar crater counts from expert analysts to those of non-specialist volunteers using CosmoQuest and found that, on average, non-specialists are able to identify craters as well as expert analysts are [11]. We took an intermediate approach, involving multiple less-experienced analysts with some training, mapping "in triplicate" to minimize false positives.

Summary and Implications: At the conference, we will present a quantitative estimate of the false positive crater identification rate, discuss the implications of our results for aeolian erosion, and relate our results to the organic-matter preservation potential of sites including Oxia Planum, the intended target of ESA's ExoMars 2018 rover.

References: [1] Armstrong et al. (2005) *Icarus.* [2] Day et al. (2015) *LPSC.* [3] Bridges et al. (2012) *Nature.* [4] Farley et al. (2014) *Science.* [5] Golombek et al. (2014) *JGR-Planets.* [6] Smith et al. (2008) *Geophys. Res. Lett.* [7] Sefton-Nash et al. (2014) *Icarus* [8] Malin et al. (2007) *JGR-Planets.* [9] Kneissel T. et al. (2011) *Planetary Space Sci., 59,* 1243-1254. [10] Michael (2013) *Icarus.* [11] Robbins S. J. et al., (2014) *Icarus, 234,* 109–131. [12] Grindrod & Warner (2014) *Geology.* [13] McEwen et al. (2005) *Icarus*, *176,* 351-381. [14] Malin et al. (2007) *JGR-Planets.*

IRON AND OXYGEN ISOTOPE FRACTIONATION DURING PHOTO-OXIDATION. N. X. Nie[1], N. Dauphas[1] and R. C. Greenwood[2]. [1]Origins Lab, Department of the Geophysical Sciences and Enrico Fermi Institute, The University of Chicago, Chicago, IL 60637, USA (xike@uchicago.edu); [2]Planetary and Space Sciences, The Open Univeristy, Milton Keynes MK7 6AA, UK.

Introduction. Ultraviolet (UV) photochemical oxidation of aqueous ferrous iron ($Fe(II)_{aq}$) has been proposed as an effective pathway to the precipitation of banded iron formations (BIFs) [1, 2]. The rationale is that in the early Precambrian more high-energy UV sunlight could reach the seawater surface, because in absence of O_2, the atmosphere was more transparent to UVs. The other two possible alternatives are: (i) O_2-mediated oxidation, in which local "O_2 oasis" are created during photosynthesis by microorganisms such as cyanobacteria [3, 4], and (ii) anoxygenic photosynthesis in which bacteria could use $Fe(II)_{aq}$ instead of H_2O as the electron donor to produce the oxidized byproduct Fe(III) rather than gaseous oxygen [5, 6]. However, compared to these alternative mechanisms, UV photo-oxidation does not require involvement of any gaseous oxygen or biology, and the oxidation rate has been calculated to be high enough to account for the extensive occurrence of BIFs [2, 7].

The principal argument against photo-oxidation is based on the experimental observation that $Fe(II)_{aq}$ in solution tends to combine with bicarbonate and silicon to form insoluble minerals [8], but the experimental setup may not have been completely relevant to the conditions that prevailed at that time and it posed instead the question of Fe(II) solubility regardless of the process responsible for its oxidation. There is no direct evidence for the involvement of biology in the formation of BIFs as they lack microfossils [9]. The only indirect evidence comes from carbon and iron stable isotope signatures of BIF-associated carbonates, which point to dissimilatory iron reduction associated with respiration of organic carbon [10, 11]. To examine the role of UV photo-oxidation in BIF formation and to differentiate between the three scenarios, we performed photo-oxidation lab experiments and analyzed the isotopic compositions of the products to a very high precision. In particular, the mass fractionation law governing the photo-oxidation process was investigated.

Methods. Our experimental procedure has already been described in detail previously [12] and so is only outlined here in brief. Oxygen is evacuated from a closed reaction system with high-purity Ar gas ($O_2 < 0.1$ ppm). The system consists of a reactor containing 350 mL H_3BO_3-NaOH buffer, and an iron introduction section and a sampling section, both connected to the reactor. Ferrous iron as $(NH_4)_2Fe(SO_4)2.6H_2O$ salt is dissolved in absence of oxygen and $Fe(II)_{aq}$ is trans-

ferred to the reactor before the UV lamp is turned on. During the reaction, products are taken at 30 min time intervals. For each, product Fe(III) precipitate and $Fe(II)_{aq}$ solution are separated from each other with a 0.1 μm syringe filter.

Experiments for iron and oxygen isotope analyses were performed seperately. For iron analysis (experiment #1; [12]), the volume of each sampled $Fe(II)_{aq}$ − Fe(III) precipitate mixture was about 7 mL (not enough for oxygen isotope measurement). Oxygen was measured on Fe(III) precipitate in experiment #2, which was similar to the experiment #1 except that more iron was introduced and larger aliquots of 18 mL were sampled. Both Fe(III) solid and $Fe(II)_{aq}$ solution from experiment #2 were also analyzed for their iron isotopic composition. The iron isotopic composition was measured with a Thermo Scientific Neptune Plus MC-ICPMS at the university of Chicago as described in [13], while the oxygen isotope measurements were performed at the Open University using the procedures outlined by [14].

Results. Preliminary data of iron isotope analysis (δ-values in experiment #1) have been reported previously [12], the data show that the Fe(III) precipitate is enriched in heavier iron isotopes relative to the initial composition, while the $Fe(II)_{aq}$ solution has a lighter composition, and all of them plot on a mass-dependent isotope fractionation line. The newly obtained data, acquired in order to determine the iron isotope fractionation law during photo-oxidation, are expressed as ε'- values (ε' ^{i}Fe = 10000* ln ($R_{i/54}/R_{i/54, std}$)). The most fractionated samples have non-zero ε'- values. Since the ε'- values were calculated by normalizing $^{57}Fe/^{54}Fe$ ratio to a fixed value of 0.3625492 using the exponential law, the non-zero values indicate that the photo-oxidation process follows a mass fractionation law that differs from the exponential law.

For the experiment #2, there is no clear correlation between iron and oxygen isotopic compositions. The change of iron isotopic composition as a function of time follows the same trend as in the experiment #1 [12]. Oxygen isotopic composition of the precipitate is heavier (ranges from -0.14‰ to +0.80‰ with an average of +0.33‰ in terms of $\delta^{18}O_{VSMOW}$) compared to Chicago tap water which is about -0.5‰ [15].

Discussion. The δ-values of photo-oxidation experiment #1 follow a Rayleigh distillation model with an isotope fractionation factor of 1.0012, that is,

+1.2‰ instantaneous isotope fractionation between Fe(III) precipitate and Fe(II)$_{aq}$ solution at 45 ℃ [12]. A plot of ε'^{56}Fe *vs.* δ'^{57}Fe (calculated as 1000*ln (δ^{57}Fe/1000 + 1)) shows that the products of photo-oxidation follow the equilibrium law (n=-1) within error. Data with high enough precision is missing to compare the mass-fractionation law documented here with the other two processes (O$_2$-mediated oxidation and anoxygenic photosynthesis) that could have been involved in BIF formation, but it is likely that those would follow the equilibrium law as well.

The BIF sample measured at very high precision, IF-G, agrees with the experimental Fe(III) precipitate and the equilibrium law. However, in the experiments the data points providing better leverage in determining the law are Fe(II)$_{aq}$ solution. The counterpart to Fe(II)$_{aq}$ solution during BIF formation would be seawater, the composition of which may have been recorded in shales [16]. If that is true, measuring shales would be a promising way to further test the photo-oxidation hypothesis.

Unlike iron, where the solution and precipitate evolved in the course of photo-oxidation, no systematic trend of δ^{18}O as a function of time is seen, implying that the solution effectively acted as an infinite reservoir in terms of oxygen. The oxygen isotopic composition is consistent with equilibrium isotope fractionation between Fe(III) oxides and waters from previous experiments which found little fractionation (Fig. 1). Although it has been well known that UV light irradiation can cause photo-chemical reactions featuring mass-independent isotope fractionation, such as photolysis of ozone [17] and of SO$_2$ [18], no clear mass-independent isotope signature was found for photo-oxidation. The Δ^{17}O values of Fe(III) precipitate (calculated from measured δ-values) range between -0.133‰ and -0.048‰ with an average of -0.078‰, where the reference mass fractionation line is the terrestrial fractionation line with a slope of 0.5247 [19], are not outside the range of terrestrial materials.

In conclusion, the isotopic compositions of iron and oxygen measured in BIFs are consistent with the results from photo-oxidation experiments and therefore photo-oxidation remains a viable pathway to BIF formation.

References: [1] Cairns-Smith A. G. (1978) *Nature, 276,* 807–808. [2] Braterman P. S. et al. (1983) *Nature, 303,* 163–164. [3] Cloud P. E. (1965) *Science, 148,* 27–35. [4] Cloud P. (1973) *Econ. Geol., 68,*1135–1143. [5] Garrels R. M. et al. (1973) *Econ. Geol., 68,* 1173–1179. [6] Widdle F. (1993) *Nature, 362,* 834–836. [7] Francois L. M. (1986) *Nature, 320,* 352–354. [8] Konhauser K. O. et al. (2007) *EPSL, 258,* 87–100. [9] Klein C. (2005) *Am. Mineral., 90,*1473– 1499. [10] Craddock P. R. and Dauphas N. (2011) *EPSL, 303,* 121–132. [11] Heimann A. et al. (2010) *EPSL, 294,* 8–18. [12] Nie N. X. and Dauphas N. (2015) *LPS 46,* #2635. [13] Dauphas N. and Rouxel O. (2006) *Mass Spectrom. Rev., 25,* 515-550. [14] Miller M. F. (1999) *Rapid Commun. Mass Spectrom. 13,* 1211-1217. [15] Bowen G. J. et al. (2007) *Water Resour. Res., 43(3).* [16] Rouxel O. J. et al. (2005) *Science, 307,* 1088-1091. [17] Chakraborty S. and Bhattacharya S. K. (2003) *J. Chem. Phys., 118,* 2164-2172. [18] Farquhar J. et al. (2001) *J. Geophys. Res., 106,* 32829-32839. [19] Miller M. F. (2002) *GCA, 66,* 1881-1889. [20] Frierdich A. J. et al. (2015) *GCA, 160,* 38-54. [21] Yapp C. J. (2007) *GCA, 71,*1115-1129. [22] Bao H. and Koch P. L. (1999) *GCA, 63,* 599-613. [23] Zheng Y. (1991) *GCA, 55,* 2299-2307.
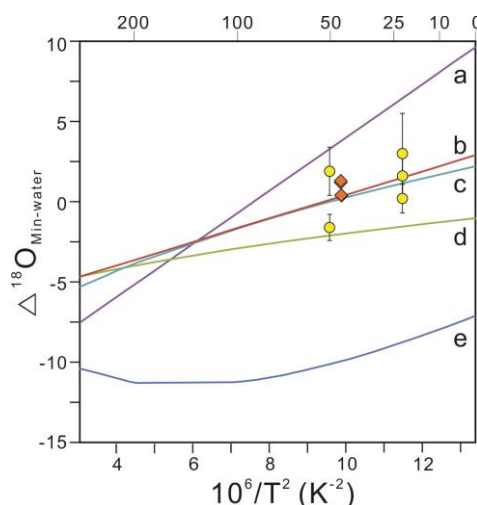
Fig. 1: *Oxygen isotopic fractionation between Fe(III) minerals and water. Yellow points are experimental data of geohite [20] and orange squares are from this study. Lines a, b, c, and d are experimental determinations while e is a theoretical calculation. a. Goethite [21]; b. Hematite [22]; c. Akaganeite [22]; d. Goethite [22]; e. Hematite [23].*

STEPS TOWARD IMPLEMENTATING THE GRADY-KIPP FRAGMENTATION MODEL IN AN EULERIAN HYDROCODE.

B. C. Johnson[1], T. J. Bowling[2], and H. J. Melosh[3], [1]Department of Earth, Environmental and Planetary Sciences, Brown University, 324 Brook Street, Providence, RI 02912, USA. (Brandon_Johnson@Brown.edu). [2] Department of the Geophysical Sciences, University of Chicago, 5734 S. Ellis Avenue, Chicago, Illinois 60637. [3]Department of Earth, Atmospheric, and Planetary Sciences, Purdue University, 550 Stadium Mall Drive, West Lafayette, IN 47907, USA

Introduction: The details of impact fragmentation and ejection are critical for understanding secondary impact cratering, the formation of planetary regolith, and the ejection of meteorites from the terrestrial planets. Smooth Particle Hydrocodes (SPHs) give robust estimates of fragment sizes especially in lower velocity collision [eg. 1], but so far SPHs have not achieved the resolution necessary to resolve fast ejecta produced by hypervelocity impacts. Recent modeling [2] shows that high velocity ejecta comes from very near the projectile where the point source approximation used in Lagragian hydrocodes and analytical models may not be valid [3,4]. Here we detail steps toward implementing the Grady-Kipp fragmentation model [5] into an Eulerian hydrocode. In the future we may consider other fragmentation models [6]. Although our end goal is to model the formation of fast ejecta and gain valuable insight into the processes outlined above, here we focus on reproducing results from laboratory scale impact experiments to validate our numerical methods.

Methods: In this work we use the 2D version of the iSALE shock physics code [7-9]. We model basalt impactors striking spherical basalt targets at vertical incidence while matching the target mass, projectile mass, and impact velocity from laboratory experiments. Fracture area and damage are calculated in the code following [5]. As clearly demonstrated by [10], the constant threshold strain for failure used by [5] is not hydrodynamically self-consistent. Thus, we use a randomly seeded threshold strain similar to [10] but still calculate fracture area according to [5] rather than making cracks and their growth explicit as in [10]. To fit the experimental data, we held the Weibull parameter m=9.5 constant while varying the k parameter.

Tensile strength and failure are determined by the Grady-Kipp model [5] where 'shear' failure is determined by [8] however we include a strain rate hardening term such that the yield stress is

$$Y = Y_0 \left(1 + \left(\frac{\dot{\varepsilon}}{\dot{\varepsilon_0}}\right)^{\frac{2}{3}}\right)$$ [6]. Where Y_0 is the yield stress without the added term, $\dot{\varepsilon}$ is the equivalent strain rate, and $\dot{\varepsilon_0}$ is a material constant.

Results: The color scale on Figure 1 is truncated at a fragment size of ~3 cm, comparable to the radius of the target. Material with these low fractures areas represent fragments that are actually resolved in the mod-

el. As expected, the smallest fragments are located under the point of impact and large spalls are located along the entire free surface. With our relatively high resolution (as compared to [5]) of 20 cells per projectile radius and a self-consistent definition for the threshold strain, we are able to resolve the observed 'intact' inner core of material [11] whereas [5] was unable to reproduce this feature.
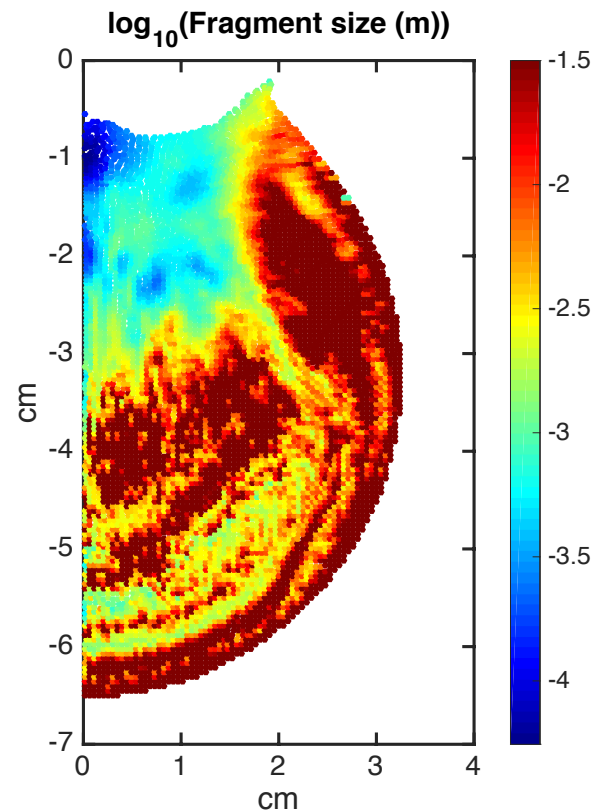
Figure 1: Tracers colored according the logarithm of final peak fragment size (50 μs after impact) for Weibull parameters $k=10^{37}$ and m=9.5. This is a model of a 1.00 x 10^{-2} kg basalt sphere striking a 0.410 kg basalt sphere at 599 m/s similar to experiment #820520 of [11].

Although we are working on producing a reliable algorithm to calculate the size of these resolved intact fragments, without estimates of their size we can only speculate on how they might change the large end of

the calculated fragment Size Frequency Distribution (SFD). Figure 2 shows some estimates of the fragment SFD where the dashed curve simply uses the method of [5] and effectively ignores these intact fragments, which account for a large fraction of the target mass (Fig. 1). The solid lines assume all tracers with peak fragment sizes more than two times larger than the largest fragment given by the previous method make up a single large fragment. This assumption is also clearly problematic as there are many resolved fragments (Fig 1.). Based on the average cell mass resolved fragments may contribute to the SFD at normalized fragment masses exceeding 1.3×10^{-4}. Although Weibull parameter k and m vary significantly with material, our best-fit to experiments occurs close to experimentally derived estimates of $k=1.59 \times 10^{38}$ and $m=9.5$ for Dresser basalt [5, 13]. Another potential problem with all current fragmentation models and an area for future exploration is the fact that fracture area is not accumulated during shear failure.

There is clearly much work to be done, but our initial models represent an important first step toward a better understanding fast ejecta fragments, secondary cratering, and the ejection of meteorites. Because we are able to directly resolve large fragments, this model may help determine the size of spall plates without significant modifications.

References: [1] Jutzi M. et al. (2009) *Icarus, 201,* 802-813. [2] Johnson B. C. and Melosh H. J. (2014) *Icarus, 228,* 347-363. [3] Head J. N. et al. (2002) *Science, 298,* 1752-1756. [4] Melosh H. J. (1984) *Icarus, 59,* 234-260. [5] Melosh et al. (1992) *JGR, 97,* 735-759. [6] Ramesh K. T. et al. (2015) *Planet. Space Sci., 107*, 10-23. [7] Amsden, A. et al. (1980) *LANL Report*, LA-8095. [8] Collins G. S. et al. (2004) *MAPS, 38*, 217-231. [9] Wünnemann K. et al. (2006) *Icarus, 180,* 514-527. [10] Benz W. and Asphaug E. (1995) *Comput. Phys. Commun., 87,* 253-265. [11] Nakamura A. and Fujiwara A. (1991) *Icarus, 92,* 132-146. [12] Takagi Y. et al. (1984) *Icarus, 59,* 462-477. [13] Lindholm U. S. et al. (1974) *Int. J. Rock. Mech. Min. Sci. Geomech. Abstr., 11,* 181-191.

Figure 2 (below): Comparison of cumulative fragment size frequency distributions for the impact conditions from Figure 1 to laboratory measurement (blue diamonds) and previous estimates from Lagrangian hydrocodes (red triangles). The black curve represents a separate run with different Weibull parameters.
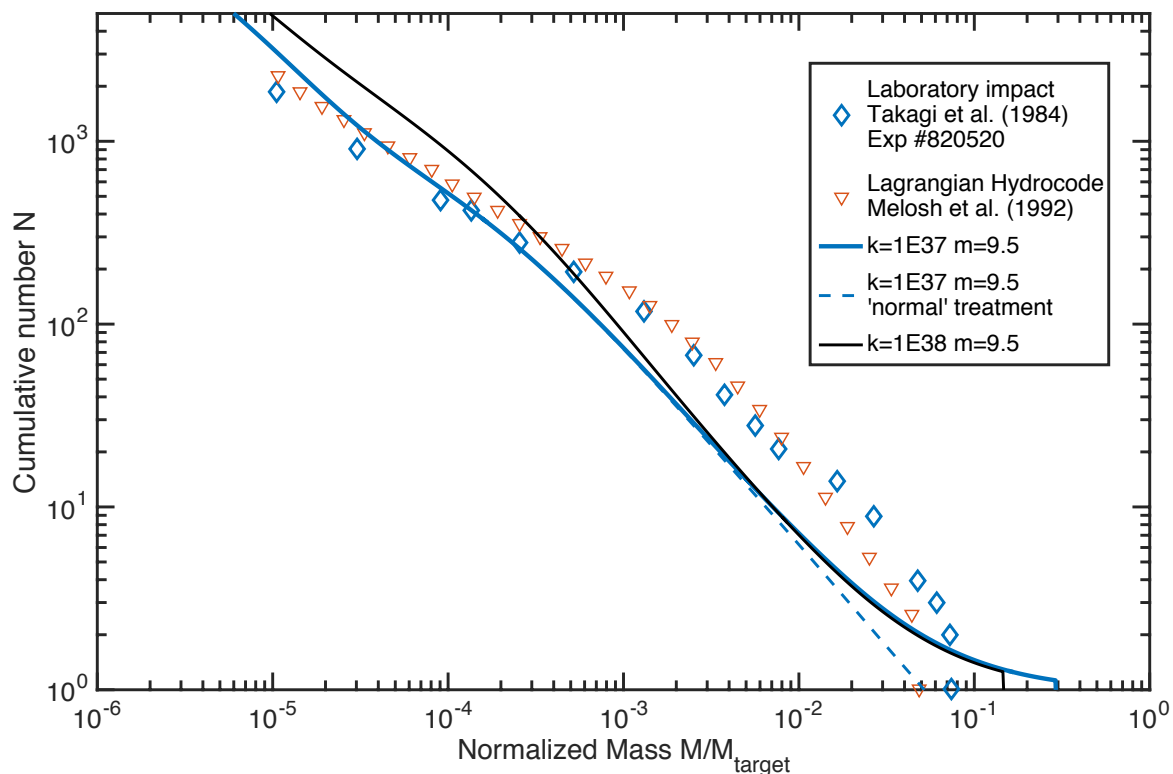
VOLCANISM ON MAGMA PLANETS: EXTREME VOLCANISM IS REGULATED BY PLANET MASS, TEMPERATURE, AND INITIAL COMPOSITION.

Edwin S. Kite[1], Bruce Fegley[2], Laura Schaefer[3], Eric Gaidos[4]. [1]University of Chicago (kite@uchicago.edu), [2]Washington University at St. Louis, [3]Harvard University, [4]University of Hawaii.

Summary: The daysides of short-period rocky exoplanets, which are now being observed [1-3], are long-lived surface magma pools. We provide estimates of magma-planet outgassing rates and magma composition. Atmospheric pressure tends toward vapor-pressure equilibrium with surface magma, and surface composition is set by the competing effects of fractional vaporization and surface-interior exchange. We use basic models to show how surface-interior exchange is controlled by the planet's mass, temperature, and initial composition. We find:- (1) atmosphere-interior exchange is fast enough to buffer surface composition when the planet's bulk-silicate FeO concentration is low, and slow when FeO concentration is high; (2) magma pools are compositionally well-mixed for substellar temperatures $\lesssim$2400 K, but compositionally patchy and rapidly variable for substellar temperatures $\gtrsim$2400 K; (3) magma currents within the magma pool cool the base of the magma pool ("tectonic refrigeration"), so the usual upper boundary condition for modeling the solid-mantle circulation of hot rocky exoplanets is too warm; (4) contrary to earlier work, many magma planets have time-variable surface compositions.

Background: Over one hundred exoplanets have masses or radii in the rocky-planet range, and substellar equilibrium temperatures hot enough to melt peridotite rock (e.g. CoRoT-7b, Kepler-10b, and WASP-47e) [4-6].These molten surfaces are tantalizing because they are relatively easy to detect and characterize [1-3] - what sets molten-surface composition? The melt-coated dayside is exposed to intense insolation, sufficient to remove H_2 [7] and to maintain a thin silicate atmosphere [8] (Fig. 1). The most-volatile rock-forming element constituents of the melt (e.g. Na, K, Fe) preferentially partition into the atmosphere. These atmospherically transported volatiles are cold-trapped on the permanent nightside, or lost to space (Fig. 1). If trans-atmospheric distillation is faster than mass exchange between the melt pool and the solid interior, then surface composition will differ from bulk-planet silicate composition. But if mass exchange between the melt pool and solid interior is fast, then surface composition will be repeatedly reset towards bulk-planet silicate composition.

In the first (compositionally evolved) case, with relatively slow atmosphere-interior exchange, preferential loss of volatiles (Na, K, Fe ...) creates a refractory Ca-Al-rich lag [9]. The lag armors the vulnerable volatile-rich interior, as on a comet. After lag formation, atmospheric pressure will be everywhere $\lesssim O(1)$ Pa. In the second (compositionally buffered) case, Na, K, and Fe are re-

plenished by surface-interior exchange; the exosphere fills with Na and K; and surface compositional evolution is extremely slow: it is buffered by the whole planet's silicate mass.
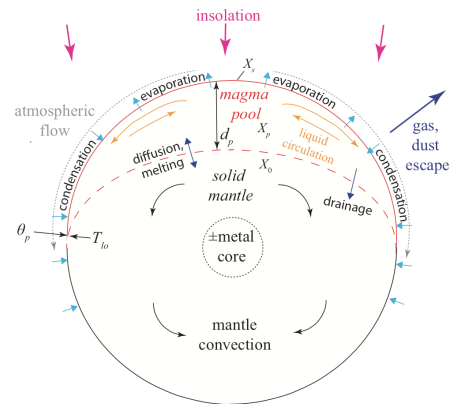

Fig. 1. Processes shaping the surface composition of a hot rocky exoplanet. Magma pool (depth d_p, mean composition X_p, surface composition X_s) overlies a solid mantle (composition X_0). d_p is shown greatly exaggerated. T_{lo} corresponds to the lock-up temperature that defines the edge of the melt pool. θ_p corresponds to the angular radius of the melt pool.

To what extent does fractional evaporation drive the hot rocky exoplanets' dayside surface composition? We set out to determine the rates of surface-atmosphere versus surface-interior exchange. To do this, we quantify the key controls on magma pool surface composition (Fig. 1): stirring of the melt pool by horizontal convection, chemical distillation of the pool through atmospheric flow, and (crucially) the buoyancy evolution of melt pools undergoing fractional evaporation (Fig. 2).

Model: In order for surface composition X_s to deviate from pool-average composition X_p (Fig. 1), the ocean mixing timescale τ_T must be shorter than the time (τ_X) needed for evaporatic ablation by fractional vaporization (advection). We use simple scalings for the ocean overturning circulation [10]. To find the fractional vaporization rate, we need a model of the winds, which we adapt from vertically-averaged models of Io's sublimation-driven atmosphere [11,12]. The ratio τ_X/τ_T decreases with temperature because evaporation increases much more quickly with temperature than thermal diffusion in the liquid. (Thermal diffusion in the liquid is needed to drive upwelling in horizontal-circulation). Neither winds nor currents much affect surface energy balance, which is set by radiative equilibrium (for $T \lesssim 3000K$). Next, we use the MAGMA code [8,13], plus literature equations-

of-state [14], to investigate whether the density of the chemically-fractionated reservoir (the residual magma left behind during fractional evaporation) is less than initial density throughout fractional evaporation. This determines whether the fractionating reservoir is unstable to sinking (Fig. 2).
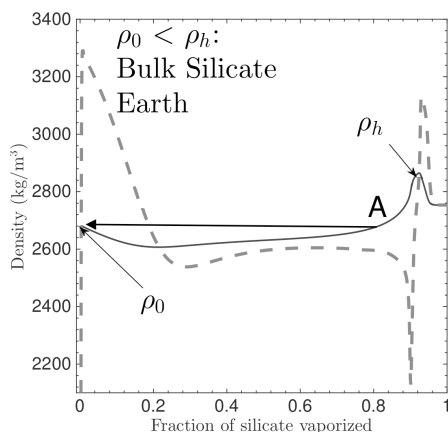

Fig. 2. Density evolution for fractional vaporization (at 2000K) of an initial composition corresponding to Bulk Silicate Earth. Thin black solid curve corresponds to the density of residual magma, and thick gray dashed curve corresponds to the density-upon-condensation of the gas. At point A, the surface boundary layer sinks into the interior. ρ_h corresponds to the maximum density at >70 wt % fractional vaporization. ρ_0 corresponds to unfractionated magma density.

Results: Results are summarized in Fig. 3. Magma-pool overturning circulation and differentiation can be viewed as a new tectonic mode for rocky planets at temperatures too high for plate tectonics, stagnant-lid convection, or heat-pipe recycling. Surface-interior exchange on magma planets is driven by near-surface contrasts in melt density (and can shut down if the surface layer becomes stably buoyant). In turn, these density effects are regulated by two factors (Fig. 3). (1) Relative vigor of winds and currents. For substellar temperature ≲2400K ("ocean-dominated" worlds), magma-pool overturning circulation outruns net evaporation, and pool surface composition tracks bulk pool composition. For substellar temperature ≳2400K ("atmosphere-dominated" worlds), pool overturning circulation is slow compared to atmospheric transport, and fractional evaporation drives pool composition away from the composition of the bulk of the pool. (2) Exposure of the planet's building-blocks to H_2O. If we assume a radial temperature gradient similar to the solar nebula, then if the planetesimals that formed the planet grew >1 AU from the star, water rock reactions will lead to high Fe-oxide concentrations in the planet's silicate mantle. Close to the star, preferential evaporation of volatile and dense Fe favors stable stratification of the residu-

al magma. This may allow a buoyant, stable lag to form a compositionally-evolved surface. However, if the planetesimals that formed the planet are reduced (low mantle FeO), fractionally-evaporated residual melt will sink. The concomitant resurfacing will repeatedly reset the surface composition to the planet-averaged silicate composition.

Tests: Magma composition may be constrained using atmospheric column densities of Na and K [15], surface spectra [16], and the properties of dust streaming from disintegrating magma planets such as K2-22b [17].
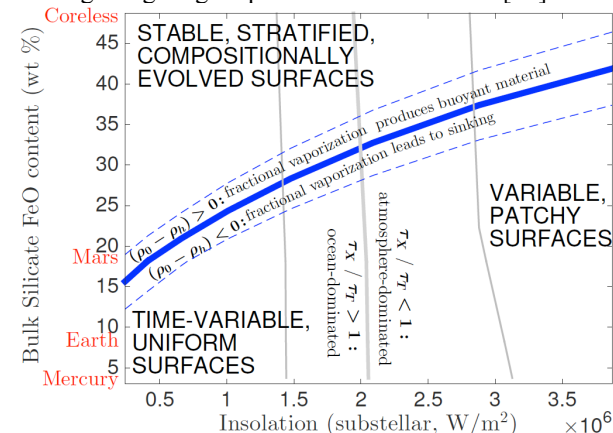
Fig. 3. Magma planet phase diagram. Stratification index $(\rho_0 - \rho_h)$ is contoured at +50 kg/m^3 (top dashed blue line), 0 kg/m^3 (thick solid blue line), and -50 kg/m^3 (bottom dashed blue line). Planets below the line are unlikely to have CaO/Al_2O_3-dominated surfaces, planets above the line are likely to have CaO/Al_2O_3-dominated surfaces. Ocean-dominance index τ_X/τ_T is contoured at 10 (left gray line), 1 (thick gray line), and 0.1 (right gray line), for 50 wt% vaporization. Lower-left quadrant corresponds to magma pools with uniform, but time-variable surfaces, well-stirred by currents. Lower-right quadrant corresponds to atmosphere-dominated magma pools with variable, patchy surfaces driven by evaporative overturn. Upper two quadrants correspond to planets with stable, stratified, CaO/Al_2O_3-dominated surfaces. Calculations assume planet period 0.84 days, radius 1.5× Earth, and gravity 1.9× Earth (= Kepler-10b).

References: [1] Rouan et al. (2011) *ApJ*. [2] Demory (2014) *ApJ*. [3] Sheets & Deming (2014) *ApJ*. [4] Leger et al. (2009) *A&A*. [5] Batalha et al. (2011) *ApJ*. [6] Dai et al. (2015) *ApJ*. [7] Lopez & Fortney (2014) *ApJ*. [8] Schaefer & Fegley (2009) *Icarus*. [9] Leger et al. (2011) *Icarus*. [10] Vallis, *Atmospheric & Oceanic Fluid Dynamics*. [11] Ingersoll (1989) *Icarus*. [12] Castan & Menou (2011) *ApJ*. [13] Fegley & Cameron (1987) *EPSL*. [14] Ghiorso & Kress (2004) *Am. J. Sci.* [15] Heng et al. (2015) *ApJ* [16] Samuel et al. (2014) *A&A* [17] Budaj et al. (2015) *MNRAS*.

THERMAL ANALYSIS OF POST-IMPACT BODIES IN THE EARLY SOLAR SYSTEM. R. J. Lyons[1], F. J. Ciesla[1], K. J. Walsh[2], T. M. Davison[3], G. S. Collins[3] , [1]The Department of the Geophysical Sciences, The University of Chicago, Chicago, Illinois, USA (rjlyons@uchicago.edu), [2]Southwest Research Institute, Boulder, Colorado, USA, [3]Impacts & Astromaterials Research Centre, Department of Earth Science & Engineering, Imperial College London, London, UK.

Introduction: Early collisions (those occurring ~10 Myrs after CAIs or less) have been invoked to explain the mixing/juxtaposition of materials of different thermal histories observed in a given meteorite and the thermal evolution of meteoritic materials which cannot be explained by radiogenic heating alone [1-8]. Unfortunately, while collisions are believed to be responsible for these features, it is unclear what collisional parameters would produce samples consistent with the observed petrologies, chronologies, and cooling rates. We aim to use quantitative methods to investigate the origin of these features. In particular, we are focusing on the Iron IAB, Winonaites, and Iron IIE, whose origins are believed to be related to an impact and for which the cooling rates of multiple samples have been determined [4,5,8].

Previously, we reported our hydrocode-N-body hybrid methodology for tracking the reaccumulation of material after an impact between young planetesimals [9]. In that work, we simulated a high-energy collision using the hydrodynamic code iSALE, and then followed the gravitational reaccumulation of ejected materials using the N-body code REBOUND. We found that the reaccumulated remnant exhibited mixing of material from different regions of the initial target body, which had been heated to different degrees due to the decay of ^{26}Al. This type of post-impact mixing is similar to that invoked for the Iron IAB/Winonaites [4,5,8] and Iron IIE [7] parent bodies. We have continued to develop our methodology and extended it to study the long-term, thermal evolution of the reaccumulated remnant. Here we report on our preliminary results, focusing on comparing model output to data collected from the Iron IAB and Winonaites.

Post Impact Reaccumulation: As we described previously [9], we ran an iSALE simulation for a given collision scenario until the shock wave from the impact had dissipated in the target body. The final states of all materials in the iSALE simulation are then taken as the initial conditions for our REBOUND simulation, which represents the post-impact body as a collection of particles. We looped over a large volume of hexagonally closed packed (HCP) spheres, interpolating the properties (mass, velocity) of each from the iSALE output to initialize the REBOUND simulations. Each particle was also assigned thermodynamic properties from the post-impact state that were retained throughout the REBOUND simulation. This differs from our

approach in [9] where we converted each iSALE Cartesian grid cell directly to particles. Using an HCP body allows us to retain the volume of the impacted body more accurately and better resolve the reaccumulation of the final remnant. We will perform a series of simulations using the N-body code pkdgrav to validate our results.

Here we report the results of our study of a 10 km body striking a 100 km target at 10 km/s at a 45-degree angle. The target is assumed to have been heated by radioactivity for 5 Myr at the time of the collision, after having accreted 2.2 Myr after CAIs. The left panel of Figure 1 shows a slice through the body at the initiation of the REBOUND simulation (end of iSALE), while the right panel shows the post-accumulation structure after ~33 hours of simulation time. The spheres are colored based on their temperatures as described in the figure caption. We again see that some materials from different regions (different colors) of the parent body are mixed as suggested for the formation theory for IAB/Winonanaites [4,5,8]. More energetic collisions would lead to greater excavation and levels of mixing. These will be the focus of future simulations.

Thermal Evolution: In order to understand the post-impact evolution of the reaccreated material we then took the final positions of the REBOUND simulation, interpolated to a Cartesian grid, and imported to a 3D thermal evolution model [3,10]. The 3D model tracks the conductive cooling of the reaccumulated body. We set the surface elements of the planetesimal to the assumed ambient temperature (170 K) for our initial calculations, but will relax this assumption in the future. The grid used in our preliminary study had a grid spacing of 1 km in each direction. A uniform heat capacity of 8.e6 erg/g/K was assumed along with a constant thermal diffusivity of 0.007 cm^2/s. We initially tracked the cooling of materials over ~10 Myr to focus on the thermal evolution of materials that were accreted at the surface of the remnant, and will consider cooling of the entire body in the future.

The top panel of Figure 2 shows the thermal state of a slice through the reaccumulated remnant after 10 Myrs. The bottom panel shows the cooling rate over that entire time period. The region around the impact site initially contains materials of very different temperatures, highlighting the mixing of materials, and this leads to large variations in cooling rates.

Figure 3 shows the cooling rate of material around the impact site as a function of the peak temperature reached. Here the cooling rate is taken as the cooling rate at T=773 K, the approximate temperature at which metallographic cooling rates are recorded in meteoritic samples. We have removed the very high cooling rates seen in materials at the surface of the remnant, as their high cooling rates are a result of the boundary conditions used in our model. Despite this, there is a large spread of cooling rates for materials buried within the final remnant, with these rates spanning 3 orders of magnitude for a given peak temperature. As discussed in [3], this is due both to the mixing of hot and cold materials, as well as the removal of insulating crust over deeper, heated materials at the impact site. An unimpacted body would evolve with an onion-shell structure, showing a tight trend of higher peak temperature regions cooling more slowly than lower ones. The lower range of the cooling rates seen in Figure 3 is close to those reported for the IAB/Winonaites [4,5,8].

Future Plans: We are currently investigating a suite of impact scenarios with our methodology, varying impactor size, velocity, and angle of impact, as well as target size and thermal structure in order to determine which impacts produce remnants whose evolution is consistent with what has been inferred for meteorite parent bodies. We will also consider differentiated bodies and the fate of mantles and cores. Ultimately, our model predictions will be used to constrain the dynamic state in the early Solar System.

References: [1] T. M. Davison et al. (2013) MaPS 48, 1894-1918. [2] T. M. Davison et al. (2012) GCA 95, 252-269. [3] F. J. Ciesla et al. (2013) MaPS 48, 2559-2576. [4] Benedix et al. (2000) MaPS 35, 1127-1141. [5] Schulz et al. (2012) GCA 85, 200-212. [6] Scott et al. (2014) GCA 136, 13-37. [7] A. Ruzicka and M Hutson (2009) GCA 74, 394-433. [8] K. J. Theis et al. (2013) EPSL 361, 402-411 [9] R. J. Lyons et al. (2015) LPSC 2015, #1982 [10] T.D. Komacek et al. (2013) LPSC 2013, #1359
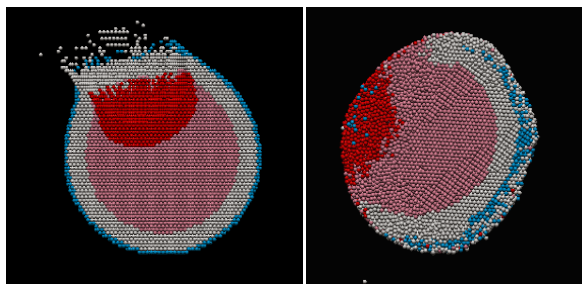

Figure 1: A vertical slice through the center of mass of the reaccumulation of a 45 degree angle impact of a 10km impactor onto a 100km body at 10km/s. Left and right panels show the initial and final states of the REBOUND simulation. Each particle is 2km in

radii and the colors indicate the temperature of the material; blue <175K, light blue <500K, white <1200K, light red <1230K, red >1230K.
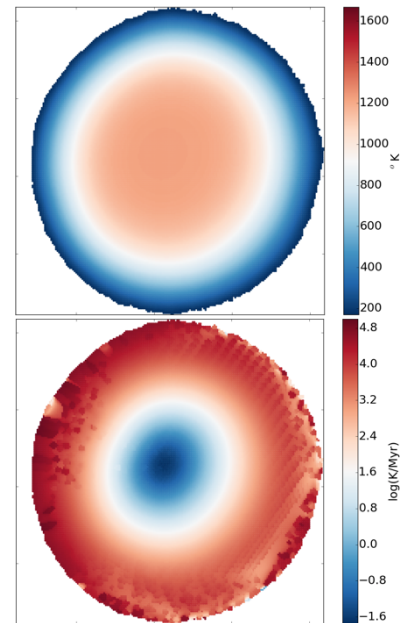

Figure 2: Contour plot of a vertical slice of the thermal evolution model distribution after 10 Myr (top). The cooling rates after 10 Myr of the same vertical slice (bottom). The juxtaposition of materials with varying post-impact thermal histories is readily seen near the surface of the body in the bottom image.
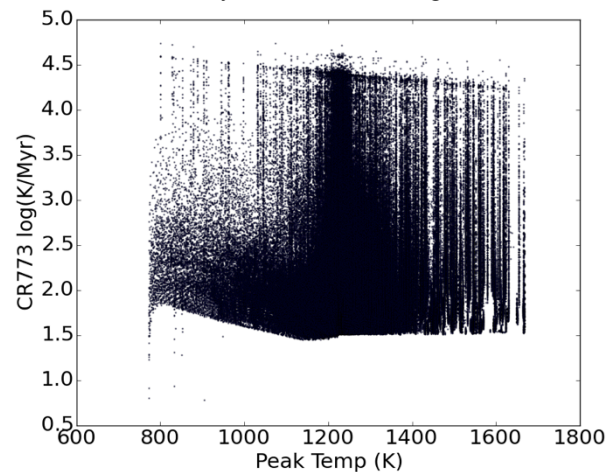

Figure 3: Peak temperature of a cell compared to the cooling rate it has experience after cooling to 500C. There is a clear spread in the cooling rates most likely due to the impact upon the body and mixing of material that has experienced different thermal histories.

EVIDENCE FOR A SINGLE STELLAR ENVIRONMENT OF R-PROCESS NUCLEOSYNTHESIS FROM LIVE [247]Cm IN THE EARLY SOLAR SYSTEM. F. L. H Tissot[1,2], N. Dauphas[1], L. Grossman[3], [1]Origins Lab, Department of the Geophysical Sciences and Enrico Fermi Institute, The University of Chicago, IL (ftissot@uchicago.edu), [2]Department of the Earth, Atmospheric and Planetary Sciences, MIT, Cambridge, MA, [3]Department of the Geophysical Sciences and Enrico Fermi Institute, The University of Chicago, IL.

Motivation: The Early Solar System (ESS) abundance of short-lived radionuclides (SLR) can be interpreted in terms of a free-decay interval (Δ) or a mixing timescale (τ), which correspond to complete or partial isolation from fresh nucleosynthetic inputs of the molecular could core parental to the solar system. For *r*-nuclides, however, the abundances measured in ESS materials require less isolation for [107]Pd and [182]Hf ($\Delta \sim$ 35 Myr) than for [129]I ($\Delta = 100 \pm 7$ Myr) and [244]Pu ($\Delta = 158 \pm 85$ Myr) [1]. To make sense of these observations, models have proposed the existence of up to three different *r*-processes producing, respectively, the light *r*-nuclides, the heavy *r*-nuclides and the actinides [1-4]. In this work [5], we determined the ESS abundance of another short-lived *r*-nuclide, the long sought after [247]Cm [*e.g.*, 6-7], and show how this additional constraint is consistent with either three different *r*-processes, or, and more likely, a single stellar environment of *r*-process nucleosynthesis and a partial *s*-process origin for [107]Pd and [182]Hf.

Background: Elements with mass above ~70 amu are the products of three main processes of stellar nucleosynthesis: the *s*- (*slow* neutron capture), *r*- (*rapid* neutron capture) and *p*- (proton) process [8-9]. If the *s*- and *p*-processes are relatively well understood (neutron capture in AGB-stars and photodisintegration of seed nuclei in supernovae, respectively [10-11]), little is known regarding the astrophysical conditions under which *r*-process nuclides are produced [1-4].

In particular, the number of different *r*-processes is a topic of intense debate. Evidence for the existence of multiple *r*-processes comes from both spectroscopic observations of Low Metallicity Halo Stars (LMHS) and the relative abundance of SLR in meteorites. LMHS are stars with low metal content that formed early in the history of the Galaxy, before the onset of the *s*-process in AGB stars. Evidence for multiple *r*-processes in LMHS include: (i) the favored production of lighter *r*-nuclides (such as Sr) over heavier *r*-nuclides (such as Ba) ([12] and refs. therein); (ii) the obvious decoupling between *r*-nuclides of lower and higher atomic masses in the composition of star CS 22892-052 [13-14]; (iii) the overabundance of Th and U relative to lighter *r*-nuclides (*e.g.*, Eu) in CS 31082-001 [15-16]; or even (iv) the gradual decrease in the abundance pattern of *r*-nuclides as a function of atomic number, from Sr to Yb, in star HD 122563 [17-20].

The second line of evidence pointing to a multiplicity of *r*-processes comes from the relative abundance of SLR in meteorites. In particular, the abundance of [182]Hf ($t_{1/2} = 8.90$ Myr) in the ESS is too high relative to that of another short-lived *r*-nuclide, [129]I ($t_{1/2} = 15.7$ Myr). This led Wasserburg et al. (1996) [2] to propose that different *r*-processes were producing the light *r*-nuclides (A≤135–140, up to ~Ba) and the heavy *r*-nuclides (A≥135–140), respectively. The existence of an actinide-specific (*e.g.*, U, Th, Pu) site was also hypothesized based on the low meteoritic abundance of [244]Pu ($t_{1/2} = 79.3$ Myr) compared to [182]Hf [1].

The existence of an actinide-specific site is, however, not necessarily warranted because [244]Pu has a long half-life and its stellar yield is uncertain [21], which makes it poorly sensitive to the history of nucleosynthesis prior to SS formation and whether or not multiple *r*-process sites contributed to the synthesis of this nuclide. In contrast, Curium-247, which ultimately decays into [235]U, has a much shorter half-life ($t_{1/2} = 15.6$ Myr) and is very well suited to address this question, provided its abundance in the ESS can be accurately and precisely determined.

[247]Cm ESS abundance: Evidence for [247]Cm decay can only be found as [235]U excesses in ESS materials. Yet, the ESS abundance of [247]Cm expected from models of Galactic Chemical Evolution (GCE) is low, and a [235]U excess from curium decay will therefore only be resolvable in phases which formed early in the SS and preferentially incorporated Cm over U. Recently, [235]U excesses of up to +3.5 ‰ (rel. to CRM-112a) were found in four fine-grained CAIs [7]. Those excesses correlate with Nd/U ratio (Nd is used a proxy for Cm, which has no stable isotope) and the authors interpreted their results as evidence for live [247]Cm in the ESS.

A complicating factor is that [235]U excesses of such magnitude could have also been produced by isotopic fractionation during evaporation/condensation processes in the early solar nebula. Indeed, the kinetic theory of gases predicts that the lighter isotope will condense (evaporate) faster during condensation (evaporation), leading to isotopic fractionation that scale as the square root of the mass of the reacting species: in the case of monatomic U in a low pressure gas, $\alpha \sim \sqrt{238/235} - 1 \sim 6.3$ ‰. The excesses found by [7] are smaller than 6 ‰ and the question thus remained as to what were the causes of the observed U isotope variations.

In the present work [5], we conducted a survey of the U isotope composition in 12 fine-grained CAIs characterized by group II Rare Earth Element (REE) patterns, in which the light REE are enriched relative to the heavy REE and U. As Cm is expected to behave like a light REE during evaporation/ condensation processes, group II CAIs, which display high Nd/U ratios (a proxy for the Cm/U ratio), are the best phases to investigate when looking for ^{235}U excesses due to ^{247}Cm decay. As in previous studies, most samples display ^{144}Nd/^{238}U ratios below 600 and δ^{235}U values within 6 ‰ of the bulk SS value. The samples display a trend between δ^{235}U and ^{144}Nd/^{238}U similar to that observed by [7], but there is significant scatter around the best-fit line. One sample (named *Curious Marie*) has an extremely high ^{144}Nd/^{238}U ratio (~13,720) and a ^{235}U excess of ~+ 59 ‰. Considerable effort was expended to confirm this result that was eventually triplicated using different analytical protocols, demonstrating that the ^{235}U excess in *Curious Marie* is real.

Using the slope of the isochron (δ^{235}U vs. ^{144}Nd/^{238}U diagram), the (^{247}Cm/^{235}U)$_{Initial}$ ratio can be calculated. Because the slope of the isochron is mainy leveraged by *Curious Marie*, the initial ^{247}Cm/^{235}U ratio obtained will correspond to the time when *Curious Marie* acquired its Nd/U ratio. The extreme U depletion observed in Curious Marie is likely due to solar nebula condensation and/or nebular/parent body alteration. The two can be disentangled by looking at the relative depletion of two refractory lithophile elements with similar volatilities (*i.e.*, expected to condense together during nebular processes). In most samples, U and Yb present similar levels of depletion relative to solar composition and the abundance of other refractory lithophile elements (*e.g.*, Nd or Sm), indicating that U and Yb have similar behaviors during evaporation/condensation processes under solar nebula conditions. In *Curious Marie*, however, the U/Nd ratio is 1000× lower than solar, while the Yb/Nd ratio is only depleted by a factor of 50. The twentyfold greater depletion in U relative to Yb in *Curious Marie* is likely due to alteration, either in the early nebula or on the parent body of Allende. Dating of aqueous alteration products on meteorite parent-bodies with extinct radionuclides ^{36}Cl, ^{26}Al, ^{53}Mn or ^{129}I suggests it took place no later than 10 Myr after SS formation [22-23]. Accounting for an alteration age of 5±5Myr, the (^{247}Cm/^{235}U)$_{Initial}$ ratio obtained from the two-point isochron between *Curious Marie* and average SS materials can be corrected to obtain a (^{247}Cm/^{235}U)$_{ESS}$ ratio of $(1.1 \pm 0.3) \times 10^{-4}$. This value is in agreement with the value of $(1.1-2.4) \times 10^{-4}$ obtained by [7] based on CAI measurements and an upper limit of ~4×10^{-3} inferred

from earlier meteoritic measurements [6]. It is also in line with the lower limit derived from GCE modeling: $(5.0 \pm 2.5) \times 10^{-5}$ [21].

Implication for the r-process: Using the (^{247}Cm/^{235}U)$_{ESS}$ ratio determined above and the open non-linear GCE model of [24], a free-decay interval of $\Delta = 87 \pm 14$ Myr is obtained. This value is in good agreement with the Δ value of ~ 100 Myr derived from ^{129}I and ^{244}Pu but is much longer then the value of ~ 35 Myr obtained from ^{107}Pd and ^{182}Hf. Recent nucleosynthetic models have, however, reconsidered the origin of ^{107}Pd and ^{182}Hf and find a significant *s*-process contribution (~80%) for both isotopes [3, 25]. In such a framework, the initial abundance of all *r*-process SLR in the ESS can be explained by a single *r*-process event, which last injected material into the protosolar molecular cloud ~100 Myr before SS formation.

Our results indicate that the multiplicity of *r*-processes inferred from LMHS abundance patterns may only be relevant to exotic conditions that prevailed in the earliest generation of stars of the Galaxy and that a single *r*-process may still be relevant to long-term GCE models.

References: [1] Dauphas N. (2005) *Nucl. Phys. A 758*, 757C-760C. [2] Wasserburg G. J. et al. (1996) *APJ 466*, L109-L113. [3] Meyer B. S. and Clayton D. D. (2000) *Space Sci. Rev. 92*, 133-152. [4] Huss G. R. et al. (2009) *GCA 73*, 4922-4945. [5] Tissot F. L. H. et al. (Accepted) *Science Advances*. [6] Chen J. H. and Wasserburg G. J. (1981) *EPSL 52*, 1-15. [7] Brennecka G. et al. (2010) *Science 327*, 449–451. [8] Burbidge E. M. et al. (1957) *Rev. Modern Phys. 29*, 547-650. [9] Cameron A.G.W. (1957), *Stellar evol. nucl. astrophys. nucleogenesis*. [10] Bisterzo S. et al. (2014) *APJ 787*. [11] Rauscher T. et al. (2013) *Rep. Prog. Phys. 76*. [12] Truran J. W. et al. (2002) *Astron. Soc. Pacific 114(802)*: 1293–1308. [13] Sneden C. et al (2003) *APJ 591(2)*: 936. [14] Cowan J. J and Sneden, C. (2004) *Carnegie Observ. Astrophys. Series 4*, 1:27. [15] Cayrel R. et al. (2001) *Nature 409*, 691–692. [16] Hill, V. et al. (2002) *A&A. 387*, 560–579. [17] Sneden C. and Parthasarathy M. (1983) *APJ 267*, 757–778. [18] Westin J. et al (2000) *APJ 530*, 783. [19] Sneden C. and Cowan J. J. (2003) *Science 299*, 70–75. [20] Honda S. et al. (2006) *APJ 643*, 1180. [21] Nittler L. R. and Dauphas N. (2006) *Meteo. Chem. Evol. Milky Way* 127–146. [22] Ross D. K. et al (2015) *LPSC XLVI*, #2552. [23] Russell S. S. and MacPherson G. J. (1997) *Workshop parent-body nebular modif. chondr. materials.* 4054. [24] Dauphas N. et al. (2003) *Nuc. Phys. A 719*, 287C-295C. [25] Lugaro M. et al. (2014) *Science 345*, 650-653.

FISSION AND RECONFIGURATION OF BILOBATE COMETS REVEALED BY 67P/C-G Daniel J. Scheeres[1], Toshi Hirabayashi[2,*], Steve Chesley[3], Simone Marchi[4], Jay McMahon[1], Jordan Steckloff[2], Stefano Mottola[5], Shantanu P. Naidu[3], Tim Bowling[6], [1]University of Colorado at Boulder, [2]Purdue University, [3]Jet Propulsion Laboratory, California Institute of Technology, [4]Southwest Research Institute, [5]German Aerospace Center (DLR), [6]University of Chicago; *thirabayashi@purdue.edu

Abstract: This paper shows that sublimation torques induced fast rotation of 67P that formed the observed cracks in its neck, and that fast spin periods can fission 67P, but that its separated components would be unable to mutually escape, leading to a new configuration due to another low-velocity merger. Other observed bilobate nuclei have volume ratios between their components consistent with being trapped in a similar cycle. Thus, this rotational fission and reconfiguration process is likely a dominant structural evolution process for short-period comet nuclei.

Introduction: The spin period of 67P was observed to decrease by 0.36 hours across its 2009 perihelion passage, down to 12.4 hours [1], indicating that significant changes in a spin rate can occur over short time periods. On the brittle surface of the nucleus [1, 2], two straight cracks are aligned along the neck, separated by 750 m, and appear to be inactive [1]. El-Maarry et al. [3] hypothesized that they might result from orbital-induced or tidal-line forces although this hypothesis has not been quantitatively tested.

We propose that they were formed during a period of past rapid rotation. To investigate this hypothesis we employed elastic and plastic Finite Element Models (FEMs). An OSIRIS shape model publicly available [4] was used, and the total mass was fixed at 1.0×10^{13} kg [1]. Also, we assume the material to be uniformly distributed and the bulk density to be 535 kg/m3 [5].

Dynamical and structural evolution of the nucleus of 67P: To investigate the structure of the nucleus of 67P, we employed FEMs on ANSYS Academic APDL 15.03. We used the elastic model by Hirabayashi and Scheeres [6] to consider the formation of cracks on the neck. The plastic FEM by Hirabayashi and Scheeres [7] was also performed to obtain the final failure types.

Our elastic analysis confirmed that tensile stress peaks appear at the locations of the observed cracks at shorter spin periods (Figure 1). At a spin period shorter than 9 hours, the locations of the peak stresses are the same as those of the observed cracks. The direction of the maximum principal stress is perpendicular to the crack planes, implying that the cracks are of open-type.

We also identified three failure types of the nucleus (Figure 2). Type I occurs at a spin period longer than ~ 9 hours. Compression may cause failure around the neck surface while the interior does not reach the yield. Type II represents tensional failure appearing on the northern side of the neck at spin periods between ~ 7

and ~ 9 hours. However, since gravity is still predominant, the southern side can support the neck structure. In Type III, since centrifugal force exceeds gravitational force at spin periods shorter than ~ 7 hours, the failure region spreads over the majority of the neck.

Our model shows that a Type I failure does not occur unless the cohesive strength is much smaller than the reported compressive strength, which is on the order of kPa [2]. In Type III, because of the existing cracks on the neck surface, stress concentration at their tips causes propagation of failure across the entire neck.

Based on these considerations, we conclude that a Type II failure resulted in the formation of the observed cracks. Figure 2 describes the upper and lower bounds cohesive strength for the nucleus to keep the original shape. Because of the existing craters, we also found that the bulk cohesive strength is between ~ 10 and ~ 200 Pa (Figure 2), consistent with earlier studies [8].

Once the spin period reaches the 7-hour limit, the body should fission. Computing the system energy of such a fissioned system, we found that at the 7-hour split limit, the system has a negative total energy and is, therefore, Hill Stable, which prevents the two lobes from escaping one another [9]. This would lead them to enter a period of orbiting and re-impacting at speeds less than escape speed (~ 1 m/s), which would preserve the nature of the lobes [10].

The above discussion raises a question of how the spin period could have exceeded 9 hours in the past without transitioning beyond the 7-hour limit during its current configuration. To analyze this problem, we used the recent observation that shows the nucleus spin acceleration to be correlated to normal emission from its surface, appropriately scaled by the incident sunlight [11]. This allows the application of computational techniques from the YORP effect [12] to a prediction of the spin acceleration of the nucleus as a function of the subsolar latitude at perihelion.

Since sublimation pressure strongly varies with heliocentric distance, the spin acceleration of the 67P nucleus primarily occurs near perihelion [11]. To assess past evolution of the spin period, we integrated 1000 clones for 5000-years by using uncertainties proportional to current orbital uncertainties. This adopted time scale is compatible with the activity lifetime of typical JFCs, $\sim 10^3$ years, which is much shorter than their $\sim 4 \times 10^5$ year dynamical lifetime [13].

Our model showed that the sub-solar latitude at perihelion is uniformly distributed between -40 and $+40$ degrees at heliocentric distances between 2 and 5 AU over a 1000-year activity lifetime (Figure 3). Therefore, this randomization allows the nucleus to pass into and out of the interval between 7 and 9 hours, forestalling spin fission. For a longer timespan, this randomization also allows the nucleus to have experienced previous cycles of the nucleus reconfiguration. Since the orbit of 67P is typical among short-period comets, it is reasonable for them to experience a similar evolution cycle.

Volume ratios of observed bilobate nuclei: We consider a volume ratio of the small lobe to the large lobe of observed bilobate nuclei. For a volume ratio higher than ~ 0.2, the total energy of these systems will be negative after fission, leading them to be subject to a period of bound evolution similar to rubble pile asteroids [14], during which additional sublimation effects could further erode or spin up the individual lobes prior to re-impact. We computed the volume ratios of bilobate cometary nuclei 1P/Halley, 8P/Tuttle, 19P/Borrelly, 67P and 100P/Hartley 2 and found that all of these nuclei had a volume ratio higher than 0.2. Observed nuclei with a single component structure may either be primordial or may have been part of a multi-component nucleus, from which smaller components are more easily shed.
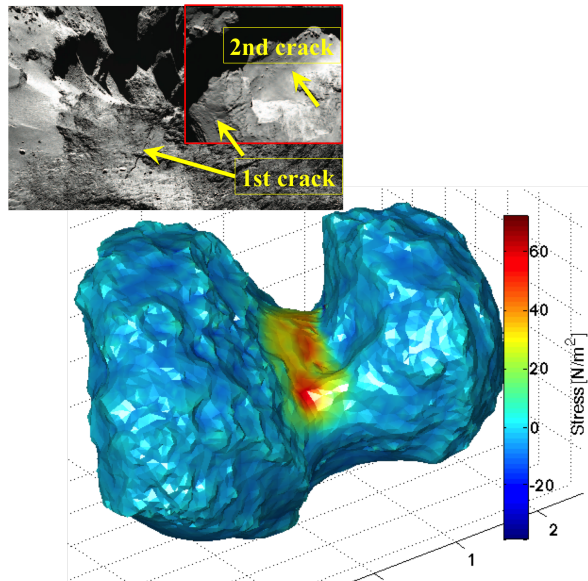

Figure 1: Elastic stress solution at a spin period of 9 hours. The plot shows the maximum component of the principal stress. The locations of the stress peaks are the same as those of the observed cracks. The images on the top are from Sierks et al. [1].

References: [1] H. Sierks, et al. (2015) *Science* 347(6220):aaa1044. [2] J. Biele, et al. (2015) *Science* 349(6247):aaa9816. [3] M. El-Maarry, et al. (2015) *GRL* 42(13):5170. [4] http://sci.esa.int/rosetta/54728-shape-model-
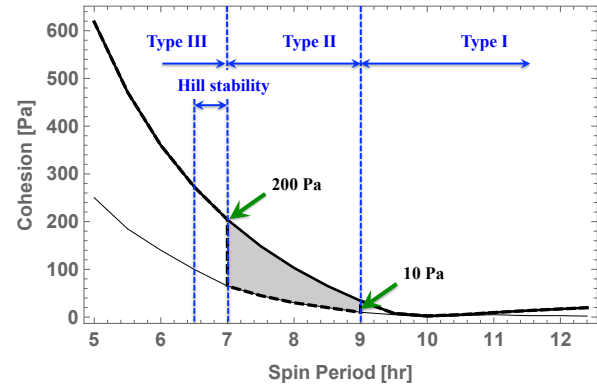

Figure 2: Failure types and conditions at different spin periods. The thicker and normal lines indicate the upper and lower bounds of the cohesive strength. The gray region is a possible region of the cohesive strength.
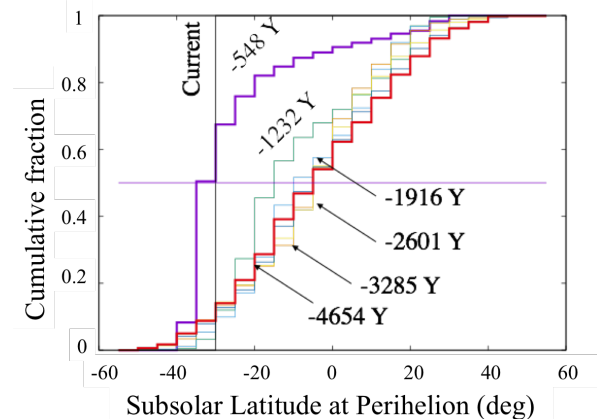

Figure 3: Cumulative fraction of the subsolar latitude of the 67P nucleus.

of-comet-67p/. [5] F. Preusker, et al. (2015) *A & A* 583:A33. [6] M. Hirabayashi, et al. (2014) *The ApJ* 780(2):160. [7] M. Hirabayashi, et al. (2015) *The ApJ Letters* 798(1):L8. [8] O. Groussin, et al. (2015) *A & A* 583:A32. [9] S. A. Jacobson, et al. (2011) *Icarus* 214(1):161. [10] M. Jutzi, et al. (2015) *Science* aaa4747. [11] H. Keller, et al. (2015) *A & A* 579:L5. [12] D. Scheeres (2007) *Icarus* 188(2):430. [13] H. F. Levison, et al. (1994) *Icarus* 108(1):18. [14] P. Pravec, et al. (2010) *Nature* 466(7310):1085. [15] R. Sagdeev, et al. (1986) *Nature* 321(6067):262. [16] J. K. Harmon, et al. (2010) *Icarus* 207(1):499. [17] H. U. Keller, et al. (2004) *Comets II* 211. [18] T. Farnham, et al. EPOXI derived shape model of 103P/hartley 2.

Table 1: Volume ratios of bilobate cometary nucleus

Comet	Volume ratio q	Ref.
1P/Halley	0.30	[15]
8P/Tuttle	0.47	[16]
19P/Borrelly	0.22	[17]
67P/Churyumov-Gerasimenko	0.58	[1]
103P/Hartley 2	0.32	[18]

[238]U/[235]U RATIO IN CARBONATES AS A GLOBAL PALEOREDOX PROXY. C. Chen[1], F.L.H Tissot[1,2], N. Dauphas[1], A. Bekker[3], G.P. Halverson[4], J. Veizer[5], B.M. Go[1], M. Naziemiec[1], L. Shaw[1], G. Healy[1] [1]Origins Lab, Department of the Geophysical Sciences and Enrico Fermi Institute, The University of Chicago, Chicago, IL (chenxicindy@uchicago.edu), [2]Department of the Earth, Atmospheric and Planetary Sciences, MIT, Cambridge, [3]Department of Earth Sciences, University of California-Riverside, Riverside, CA, [4]Department of Earth and Planetary Sciences, McGill University, Montreal, Quebec, Canada, [5]Department of Earth and Environmental Sciences, University of Ottawa, Ottawa, Canada.

Introduction:

Uranium has two main oxidation states: 4+ and 6+. In the modern ocean, U is present in its most oxidized, highly soluble form, U^{6+} [1]. In the Archean, however, when the oxygen concentration in the atmosphere was low, U was likely present in its reduced 4+ state, which has low solubility. This contrast in solubility behavior depending on the redox conditions makes U a very useful proxy of the global oxygenation state of the Earth. Indeed, one of the most important indicators that the pO_2 was low in the Archean is the survival of detrital uraninite [2], which is unstable under the modern oxic conditions.

In addition to its oxidation state, the elemental abundances of U in marine sediments can bring further insights into the redox conditions in Earth's atmosphere and ocean [3, 4]. Additionally, several recent studies have shown the potential of U isotope ratios to provide further constraints on the redox conditions in the oceans through time [*e.g.*, 5-9]. So far, much focus has been devoted to analysis and interpretation of the shale record [5-6, 10-13]. A difficulty with black shale samples, however, is that they have highly fractionated U isotopic compositions relative to seawater, and it is unclear what controls this fractionation and whether it remained constant throughout Earth's history. An additional source of uncertainty is that shales can contain a significant portion of detrital U that needs to be corrected for [5, 13-14].

To circumvene these difficulties, we have decided to study U in the carbonate record. There are two main reason for this choice: (i) the U isotopic fractionation relative to seawater in modern carbonates is small [15], (ii) and the detrital component in these samples should be relatively minor and can easily by corrected for, if present. Furthermore, carbonate samples provide an extensive record of Earth's history.

Background:

Application of U isotopes as a paleoredox proxy relies on the fact that sediments precipitated under anoxic/euxinic conditions are enriched in [238]U relative to [235]U. Assuming that the oceanic U budget is at steady-state with regards to U isotopes (a valid assumption for

the modern ocean, [9]), the seawater $\delta^{238}U$ value directly depends on the extent of global oceanic anoxia (*i.e.*, the fraction of U that is removed to anoxic sediments; Fig. 1). Therefore, estimates for the $\delta^{238}U$ value of seawater through time will provide constraints on the redox state of the global ocean. This is true provided that a rock record that faithfully tracks the U isotopic composition of the seawater can be identified.
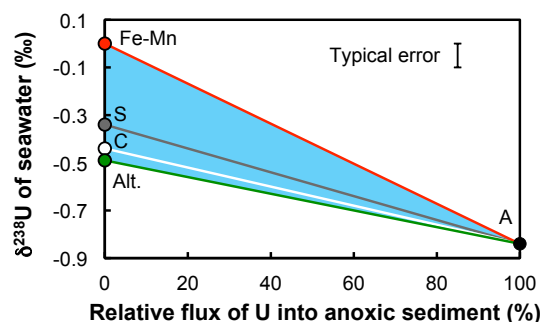
Figure 1: Expected $\delta^{238}U_{Seawater}$ value plotted as a function of the flux of U into anoxic sediments, relative to the total U flux out of the ocean. The sinks considered are: anoxic sediment (A), iron-manganese nodules and metalliferous sediments (Fe-Mn), suboxic sediments (S), carbonates (C), and altered oceanic crust (Alt.). Lines between the endmembers represent the evolution of the $\delta^{238}U_{Seawater}$ assuming that U is only incorporated in the two endmembers considered, and that the oceanic U budget is at steady-state.

The fractionation factor associated with the carbonate sink is small [15], and varies much less than the one associated with the anoxic/euxinic sink. Thus, carbonates might potentially provide a more powerful and reliable record of the $\delta^{238}U$ of seawater than black shales. By measuring the U isotopic compositions of a large suite of marine carbonates, which span a broad time period, we aim to reconstruct the paleoredox conditions in the ocean through time. This first continuous record of ocean oxygenation can provide new insight into the redox conditions during the "boring billion" [16]: a billion year period of purported environmental and biospheric stasis that started with the disappearance of BIFs at ~1.8 Ga. The demise of BIFs is widely interpreted to reflect a major change in the global redox state of the ocean. The question remains, however,

as to whether the nature of this shift was towards more oxygenated, anoxic (ferruginous), or euxinic (anoxic + sulfidic) water column conditions.

Digestion protocol:
To avoid the impact of secondary processes and access the original $\delta^{238}U$ value recorded by the carbonate samples, a step-leaching protocol was developed. It is based on the idea that easily mobilized U, which is also more likely to be of secondary origin, can be selectively removed from the sample by partial digestion with a dilute acid. A progressive digestion experiment, with 10% increment digestion steps, was performed on modern carbonates (stony coral from Florida) with dilute acetic acid (20% by volume) to track the release pattern of U isotopes.

For the concentrations, the first few leachates are depleted in U, while those of the intermediate and late leachates vary around the bulk value. Moreover, the U fractions collected in each step have variable isotopic compositions that can be significantly different from the value of modern seawater [9]. In particular, early leachates show U isotopic composition heavier than seawater by up to 0.3 ‰, while the final leachates tend to have $\delta^{238}U$ lower than seawater by 0.1 to 0.2 ‰.

From the results of the sequential leaching experiment, a two step-leaching protocol was designed for application to carbonate samples. In the first leaching step only a small fraction of the carbonate is digested in order to remove easily mobilized U that could have an extraneous origin, then in a second step, the bulk of the carbonate is digested in order to access the original U isotopic composition of the carbonate sample. Care was taken to avoid dissolution of detrital fraction, which could contribute U from phases other than carbonates (*e.g.*, silicates), whose isotopic composition will likely be different from that of the carbonate.

Sample selection and processing:
More than 200 samples are currently being processed through the U isotopic analysis protocol (*i.e.*, step-leaching, column chemistry and high-precision measurement on MC-ICPMS) [see details in 9]. Each of the carbonate sample of this large collection was carefully selected so as to satisfy the following requirements: (1) the unit must be of marine origin (*i.e.*, sediment, deposited in the open ocean) in order to ensure that the signal recorded in the sample corresponds to the global ocean redox conditions, (2) the unit and sample must have experienced only limited secondary alteration in order to minimize elemental and/or isotopic resetting of the U systematics, (3) the entire sample

set must span most of Earth's history, with a high temporal resolution.

Identification of the least-altered and best-preserved samples was based on a combination of petrological evidence and an array of geochemical tracers that reveal the extent of post-depositional resetting of geochemical signatures. For example, post-depositional fluid circulation enriches carbonates in Mn, and decreases their Sr/Ca ratios [17]. Thus, samples with the highest Sr/Ca ratio and lowest Mn concentration were selected in preference to other samples. Similarly, the isotopic compositions of oxygen and carbon were also considered, with preference given to samples characterized by higher $\delta^{18}O$ and $\delta^{13}C$ values, which are less likely to be affected by dissolution-reprecipitation during infiltration of diagenetic and basinal waters or hydrothermal fluids with mantle composition [18].

The results obtained from this study will be used to reconstruct the evolution of the marine redox conditions through time. Preliminary results will be presented at the conference on at least 50 samples that have already been measured.

References: [1] Langmuir, D. (1978) *Geochim. Cosmochim Act, 42(6),* 547–569. [2] Rasmussen, B. and Buick, R. (1999) *Geology, 27(2),* 115-118. [3] Partin, C. A. et al. (2013) *Chemical Geology, 362,* 82-90. [4] Partin, C. A. et al. (2013) *Earth and Planetary Science Letters, 369-370,* 284–293. [5] Andersen, M. B. et al. (2014) *Earth and Planetary Science Letters, 400,* 184-194. [6] Montoya-Pino C., Weyer S., et al. (2010) *Geology, 38,* 315–318. [7] Weyer S. et al. (2008) *Geochim. Cosmochim Act, 53,* 845-857. [8] Stirling C.H. et al. (2007) *Earth and Planetary Science Letters, 264,* 208-225. [9] Tissot, F.L.H. and Dauphas, N. (2015) *Geochim. Cosmochim Act, 167,* 113-143. [10] Kendall, B. et al. (2013) *Chemical Geology, 362,* 105-114. [11] Kendall, B. et al. (2015) *Geochim. Cosmochim Act, 156,* 173-193. [12] Dahl, T. W. et al. (2014) *Earth and Planetary Science Letters, 401,* 313-326. [13] Asael, D. et al. (2013) *Chemical Geology, 362(0),* 193-210. [14] Noordmann, J. et al. (2015) *Chemical Geology, 396,* 182-195. [15] Romaniello et al. (2013) *Chemical Geology, 362,* 305-316. [16] Buick, R. et al. (1995) *Chemical Geology, 123,* 153-171. [17] Veizer, J. et al. (1989) *Geochim. Cosmochim Act, 53(4),* 845-857. [18] Veizer, J. et al. (1989) *Geochim. Cosmochim Act, 53(4),* 859-871.

ENHANCED COSMOGENIC NEON-21 AND HELIUM-3 IN HIBONITE-RICH CAIS L. Kööp[1,2,4], P. R. Heck[1,2,4], H. Busemann[5], C. Maden[5], R. Wieler[5], and A. M. Davis[1,2,3,4], [1]Department of the Geophysical Sciences, [2]Chicago Center for Cosmochemistry, [3]Enrico Fermi Institute, Univ. of Chicago, Chicago, IL, USA [4]Robert A. Pritzker Center for Meteoritics and Polar Studies, Field Museum of Natural History, Chicago, IL, USA (E-mail: koeoep@uchicago.edu), [5]Institute of Geochemistry and Petrology, ETH Zurich, Zurich, Switzerland.

Introduction: PLAty hibonite Crystals (PLACs) and isotopically related hibonite-rich Ca-Al-rich inclusions (e.g., non-platy crystals and aggregates, collectively referred to as PLAC-like CAIs hereafter) are among the most isotopically anomalous materials believed to have formed inside the Solar System [1,2]. Isotope anomalies in PLAC-like CAIs can be of similar magnitude as those in presolar grains (e.g., PLAC-like CAIs show a $\delta^{50}Ti$ range of ~300‰ [1,2], which is comparable to many mainstream silicon carbide grains [3]). However, several lines of evidence indicate a Solar System origin for PLAC-like CAIs. For example, with diameters up to ~200 µm, PLAC-like CAIs are significantly larger than presolar grains (typically sub-µm-sized). Furthermore, their $\Delta^{17}O$ values fall within the range of Solar System materials [2,4] and their mass-independent isotopic characteristics strongly resemble those of FUN CAIs (i.e., variations in $\Delta^{17}O$, large variations in the neutron-rich isotopes ^{48}Ca and ^{50}Ti that tend to correlate in sign, a link between ^{26}Al-depletions and presence of large-scale anomalies [4,5 and references therein]).

The highly anomalous isotopic character of PLAC-like CAIs may indicate that these CAIs formed at an early stage in Solar System history, prior to a widespread distribution of ^{26}Al and large-scale dilution of nucleosynthetic effects. They could thus be among the first materials that formed inside the Solar System. The resulting long residence times inside the solar nebula make PLAC-like CAIs interesting samples to look for effects that could have affected disk materials. Among these is the possibility that nebular materials may have been exposed to high fluxes of solar energetic particles, for example during an early, active period of the young Sun [6], which could have manifested itself in the presence of noble gas isotopes formed by spallation. Therefore, we have analyzed two Murchison hibonite grains for their He and Ne isotopic composition. Here, we report the preliminary results.

Samples and methods: Two hibonite crystals (a stubby, ~50 µm crystal and a platy, ~200 µm crystal) were chosen for this study and analyzed together in one step ('bulk analysis'). These two grains were extracted from an HCl-HF-treated density separate of the Murchison (ME 2752, Field Museum of Natural History) residue alongside other hibonite-rich CAIs presented in [4]. While no isotopic characteristics were determined prior to noble gas measurement, their morphologies and mineral chemistry determined by energy-dispersive spec-

troscopy (EDS; average composition of 1 wt% MgO, 89 wt% Al_2O_3, 8 wt% CaO, 2 wt% TiO_2) resemble properties of other PLAC-like CAIs [4]. The total mass of the two grains (1.4×10^{-6} g) was calculated from volume estimates using scanning electron microscope (SEM) images taken at different stage rotation and tilt angles and an assumed density of 3.84 g cm^{-3}. A conservative ~50% uncertainty was assumed for the volume determination and propagated.

For noble gas analysis, the grains were first cleaned with Optima^{TM} quality isopropanol and water, then dried and pressed into gold. Noble gases were extracted with a Nd-YAG 1064 nm laser and He and Ne isotopes were measured with an ultra-high-sensitivity noble gas mass spectrometer at ETH Zurich [7]. We used an analytical protocol developed specifically for analyses of very low gas amounts [8]. SEM work after noble gas measurements showed that the hibonites were fully melted, and Ca- and Al-enrichments were found in the gold in the analysis region by EDS.

Results: The measured amount of ^3He is ~9×10^{-13} cm^3 STP (<u>s</u>tandard <u>t</u>emperature and <u>p</u>ressure; 1 cm^3 STP = 2.6868×10^{19} atoms) with an uncertainty on the order of 3–4%, the ^3He concentration is $(6.0\pm2.8)\times10^{-7}$ cm^3 STP g^{-1} (uncertainty dominated by volume estimate). The measured Ne isotopic composition plots close to a mixing line between air [9] and the cosmogenic Ne isotopic composition produced within hibonite ([10]; Fig. 1a). Assuming that the measured composition is a mixture of these two components, the cosmogenic amount of ^{21}Ne ($^{21}Ne_{cos}$) is ~2×10^{-13} cm^3 STP, with an uncertainty on the order of 3–4%. The concentration of $^{21}Ne_{cos}$ is $(1.6\pm0.7)\times10^{-7}$ cm^3 STP g^{-1}.
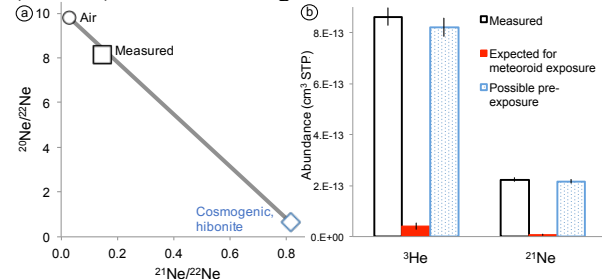
Figure 1. a) The measured Ne isotopic composition plots close to the mixing line defined by air Ne [9] and by cosmogenic Ne produced within hibonite during meteoroid exposure [10]. b) The measured ^3He and ^{21}Ne gas amounts (gray) are higher than the calculated amounts expected for a ~1.6 Ma [11] meteoroid exposure (solid, red). The difference (dotted, blue) corresponds to the gas amount we ascribe to precompaction exposure in space or the regolith on the parent body.

Discussion: Assuming that these concentrations of cosmogenic [3]He and [21]Ne were entirely acquired in the Murchison meteoroid would lead to exposure ages of the hibonites of 34±11 Ma and 51±21 Ma, respectively (assuming the same shielding assumptions for the Murchison meteoroid as [11] and production rates calculated by [10] using the elemental abundances of the hibonites obtained by EDS). These nominal exposure ages are significantly longer than the bulk meteoroid exposure age of Murchison of ~1.6 Ma [11], indicating that at least one of the two grains analyzed experienced an additional phase of exposure to cosmic rays. This could have occurred at small depths in the parent body regolith before compaction (scenario I), while the grains were free-floating in the solar nebula, possibly close to the young Sun (scenario II), or in interstellar space if the grains are presolar (scenario III). We consider scenario III unlikely, based on the arguments outlined in the introduction.

Scenario I: Support for a regolith precompaction exposure of the analyzed hibonites may come from the long nominal exposure ages of ~30 Ma that have been reported for some Murchison chondrules [11,12]. A regolith irradiation by GCR was favored by [11,12] for the [3]He and [21]Ne excesses in chondrules, because the excess Ne had a [22]Ne/[21]Ne ratio as expected for GCR production and because excesses were exclusively found in chondrules separated from the clastic matrix, not in chondrules from primary rock fragments (i.e., aggregates that are thought to have experienced the same precompaction exposure history in the parent body). The petrological context of our hibonites within the meteorite (primary rock fragment vs. matrix) could therefore help to distinguish between preexposure origins [12]. However, this context is not known as the studied hibonites were picked from an acid residue obtained from bulk Murchison. Therefore, a nonregolith (scenario II) precompaction exposure history for hibonites cannot entirely be excluded at this point.

Scenario II: If the excess [3]He and [21]Ne$_{cos}$ were the result of precompaction exposure while the grains were floating in the solar nebula, nominal precompaction exposure ages for solar and cosmic rays can be calculated from adjusted precompaction exposure concentrations (i.e., $c_{precompaction\ floating\ exposure} = c_{measured} - c_{meteoroid}$) of [3]He and [21]Ne using the present-day SCR and GCR production rates at 1 AU from [13]. The resulting precompaction exposure ages are 30±8 Ma and 13±5 Ma for [3]He and [21]Ne, respectively. As the maximum time between formation of CAIs and incorporation into the meteorite parent bodies is thought to be on the order of ~5 Ma, these ages are too high for free-floating hibonites. In this, perhaps less likely scenario, the enhanced [3]He and [21]Ne$_{cos}$ abundances would thus require

that cosmic ray fluxes were significantly higher in the early Solar System or that prolonged irradiation occurred close to the young Sun.

Conclusions and outlook: The high abundances of [3]He and [21]Ne found during the analysis of two Murchison hibonites indicate that at least one of the two grains experienced a precompaction exposure to cosmic rays that occurred in a currently unknown setting, either in the parent body regolith or while floating in the solar nebula before parent body formation. If exposure occurred within the solar nebula, the high gas abundances would require a significantly higher cosmic ray flux, e.g., due to higher activity of the young Sun (early active Sun) or in close proximity to the Sun, in an optically thin region of the nebula.

Additional work is planned for the near future to identify the setting of this precompaction exposure. In particular, we plan to analyze a larger number of individual Murchison hibonites for their He and Ne isotopic compositions to improve statistics and to look for variations in the noble gas concentrations among different grains. To explore whether the high gas abundances are due to regolith exposure, we also plan to analyze spinel grains from the same Murchison acid residue. A number of the selected hibonite and spinel grains have already been cut into two pieces using a focused ion beam to allow subsequent isotopic analyses (e.g., [26]Al-[26]Mg).

References: [1] Ireland T. (1990) *GCA, 54*, 3219-3237. [2] Liu M.-C. et al. (2009) *GCA, 73*, 5051–5079. [3] Hynes K. M. & Gyngard E. (2009) *LPS XL,* #1198. [4] Kööp L. et al. (2015) *LPI Contrib. 1856,* #5225 [5] Krot A. N. et al. (2014) *GCA, 145*, 206–247. [6] Hohenberg C. M. et al. (1990) *GCA, 54*, 2133–2140. [7] Baur, H. (1999) *EOS Trans. AGU*, 46, F1118. [8] Heck, P. R. et al. (2007) *ApJ*, 656, 1208–1222. [9] Heber V. S. et al. (2009) *GCA, 73*, 7414–7432. [10] Leya I. & Masarik J. (2009) *MAPS, 44*, 1061–1086. [11] Roth A. S. G. et al. (2011) *MAPS, 46*, 989–1006. [12] Riebe M. et al. (2015) *LPI Contrib. 1856,* #5030. [13] Trappitsch R. & Leya I. (2013) *MAPS, 48*, 195–210.

Investigating a Stellar Wind Origin for High ^{26}Al and Low ^{60}Fe in the Early Solar System. V. V. Dwarkadas[1,] N. Dauphas[2], and B. S. Meyer[3], [1]Department of Astronomy and Astrophysics, University of Chicago, 5640 S Ellis Ave, ERC 569, Chicago, IL 60637 (vikram@oddjob.uchicago.edu), [2]Origins Lab, Department of the Geophysical Sciences and Enrico Fermi Institute, University of Chicago (dauphas@uchicago.edu), [3]Department of Physics and Astronomy, Clemson University, Clemson, SC 29634-0978 USA (mbradle@clemson.edu),

Introduction: Understanding the formation of the solar system requires an astrophysical understanding of how, where and in what quantities extinct radionuclides are produced and transported. To study this, we have started a multi-scale investigation coupling stellar nucleosynthesis, high-resolution simulation of stellar wind-interstellar medium (ISM) interactions, and coarser scale simulation of mixing in molecular clouds, to track the fate of newly synthesized radionuclides.

A critical constraint on solar system formation is the high abundance of ^{26}Al ($t_{1/2}$=0.7 Myr), which exceeds by a factor of ~17 the average ISM abundance at solar system birth from gamma-ray astronomy [1,2,3]. ^{26}Al in meteorites is in too high abundance [4,5,6] to be accounted for by long-term chemical evolution of the Galaxy [7, 4, 8] or early solar system particle irradiation [9, 10]. Instead, ^{26}Al must have come from the direct injection from a nearby supernova [7,11,12], stellar winds from massive stars [5, 13, 14, 15, 16], or winds from an AGB-star [8]. The latter is unlikely, because of the remote probability of finding an evolved star at the time and place of solar system formation [6,17].

It has been suggested that 26Al in meteorites may have come from the injection of a nearby supernova that triggered the solar molecular cloud core into collapse [11, 18]. If correct, one would expect to also find high abundance of ^{60}Fe ($t_{1/2}$=2.6 Myr). Recent work found a ^{60}Fe/^{56}Fe ratio at solar system formation that is a factor of ~30 lower that the average ISM value, which is inconsistent with direct injection from a nearby supernova [6, 19]. We are thus confronted with the challenge of explaining both high ^{26}Al/^{27}Al and low ^{60}Fe/^{56}Fe ratios. An appealing possibility is that ^{60}Fe was derived from the Galactic background, while ^{26}Al was derived from winds of one or several massive stars [6]. Indeed in massive stars, ^{26}Al is produced in more external regions than ^{60}Fe.

We are carrying out theoretical modeling coupled with multi-scale high-resolution multi-dimensional ionization-gasdynamics simulations to test this scenario. Our team has adopted a multi-pronged approach to tackle this problem. One avenue is to investigate the evolution of the winds from massive stars, especially Wolf-Rayet stars (which are responsible for up to 50% of the production of ^{26}Al in the ISM [20]), and the mixing of stellar winds with the surrounding medium. This is followed by detailed computations of the su-

pernova ejecta expanding within this medium. The flux estimates resulting from these calculations are used in a 3D model of chemical evolution, in which nucleosynthesis, transport and radioactive decay of nuclides are tracked. This will allow us to investigate whether Sun-like stars can form from wind-contaminated material enriched in ^{26}Al and normal ^{60}Fe.

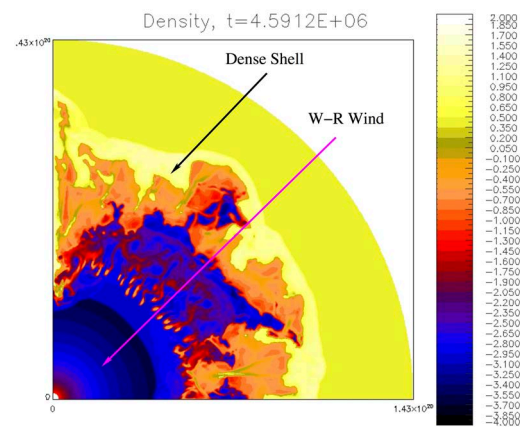Figure 1: Density snapshot from the evolution of a wind-blown bubble around a 40 solar mass star at ~4.6 Myr, using our ionization-gasdynamics code *Avatar*. The star spends most of its life as a main-sequence star. The size of the bubble is set in this phase. The interior is low density surrounded by a high-density shell. It leaves the main sequence to become a Red Supergiant star, followed by the Wolf-Rayet phase. The filamentary structure seen is a direct result of instabilities due to the mixing of layers of different densities. The Wolf-Rayet wind (innermost) has a very high momentum and mixes all the material ejected in the previous phases within the bubble, thus altering the composition of the material. Wind material from all phases is confined within the dense shell of the bubble, and not mixed with the ISM. The subsequent supernova shock wave can destroy the dense shell and mix the stellar ejecta with the surrounding ISM. An outstanding question is whether SN-driven bubble-ISM mixing can occur without delivering too much ^{60}Fe.

Formation of Wind-Blown Bubbles containing ^{26}Al around Massive Stars: A critical component of this investigation, and one that has not received much attention in the past, is the production and mixing of ^{26}Al from massive (> 8 solar masses) stars, especially Wolf-Rayet (W-R) stars. The main difficulty is that winds from massive stars form wind-blown bubbles around the stars, consisting of a low-density interior

surrounded by a high-density shell, and do not mix directly with the surrounding medium. Therefore, *the ^{26}Al that is being produced cannot be immediately mixed with the ISM, but is contained within the dense bubble (Figure 1).* Another mechanism is required to break up the dense shell and mix the contents of the bubble with the ISM, leading to a delay in the mixing. Instabilities within the bubble shell may lead to some leakage, but simulations and observations suggest this is not a large effect (Figure 1). The ^{26}Al and other products that are transported via mass-loss can only be mixed in with the ISM upon the impact of the subsequent shock wave that arises when the massive star collapses as a supernova (SN). The shock wave expands within the bubble until it collides with the dense shell, breaking it apart in most cases. In some scenarios, particularly when the shell has swept-up a large amount of interstellar material, the shock could become radiative and get trapped within the dense shell [21]; in these cases the ^{26}Al may never be released into the surrounding until the shock manages to emerge or the bubble dissipates over a much larger timescale.

In order to investigate these possibilities, we are carrying out a series of simulations investigating the various steps: (1) The formation of wind-blown bubbles around massive W-R stars of different initial masses, taking the evolution of the star and the stellar yields into account [22,23]. Abundance yields for massive stars were kindly provided by G. Meynet [24]. (2) The impact of the subsequent SN shock wave with the W-R shell and the release of the trapped wind-blown material, including ^{26}Al, as well as ^{26}Al synthesized in the SN explosion, into the surrounding medium. The SN ejecta also contribute the ^{60}Fe that will be found in the early solar system. (3) The subsequent mixing of the hot material with the cold surrounding medium to form the early solar system.

Analytic Solution for the Properties of Wind-Blown Bubbles: There exists a large parameter space of initial masses of stars, interstellar medium densities, SN shock parameters, mixing parameters and evolutionary variables, and it would be computationally prohibitive to simulate all of these with multi-dimensional simulations. We have therefore worked on a semi-analytic solution to describe the evolution of the wind bubbles. We have succeeded in deriving a solution that parameterizes the radius of the wind bubble in terms of the evolutionary parameters of the star, i.e. the star's mass, radius, temperature, luminosity, and Eddington parameter (which can be close to 1 for the very massive stars that may produce large amounts of ^{26}Al). This solution can be used in an evolutionary model to describe the radii of the bubbles evolving in a medium of given density, and can also provide the

pressure and density within the bubbles [25]. It can be used to give the size of the bubbles due to a distribution of stars of various masses, and, combined with the yields from stellar evolution models, the composition of the material within each bubble, especially the amount of ^{26}Al contained within the bubble. Furthermore, it can provide some parameters needed to investigate the evolution of the subsequent SN shock wave within the bubble. We are currently working on describing the latter in a semi-analytic manner.

This is a multi-year project, and we are currently developing the necessary infrastructure, including various tools and concepts, to tackle the question of the ^{26}Al/^{60}Fe ratio in the early solar system. One component is the contribution of massive star winds, and therefore W-R bubble formation and disruption. *At this conference we will show representative simulations that illustrate various facets of the bubble evolution and SN shock impact relevant to this problem. We will then outline the analytic solution that we have derived for the bubble properties, its derivation including the inherent assumptions, and illustrate its use.*

Multi-Zone Mixing Calculations: The analytic solutions mentioned above will be included in a multi-zone calculation of the chemical evolution of the ^{26}Al/^{60}Fe ratio in the ISM due to a large ensemble of stars in the interstellar medium [26] .

References: [1] Jacobsen et al. (2008) *EPSL, 272*, 353-364. [2] McPherson et al. (1995) *Meteoritics, 30*, 365-386. [3] Lee T. et al (1976), *Geo. Res. Let., 3*, 109-112. [4] Huss et al. (2009) *Geo. Et Cosmo. Acta., 73*, 4922-4945. [5] Diehl R et al. (2006), *Nature, 439*, 45-47. [6] Tang H. and Dauphas N. (2012) *EPSL, 359*, 248. [7] Meyer B. and Clayton D. (2000) *From Dust to Terrestrial Planets*, 133–152. Springer. [8] Wasserburg et al. (2006) *Nuc. Phys. A, 777*, 5-69. [9] Marhas K. et al. (2002) *Sci., 298*, 2182-2185. [10] Duprat J. and Tatischeff V. (2007) *ApJL, 671*, 69-72. [11] Cameron A., and Truran J. (1977) *Icarus, 30*, 447-461. [12] Boss A. and Keiser S. (2013), *ApJ, 717*, 51. [13] Arnould M. et al. (1997), *A&A, 321*, 452-464. [14] Gaidos E. et al. (2009) *ApJ, 696*, 1854. [15] Tatischeff V. et al. (2010), *ApJL, 714*, L26-29. [16] Gounelle M. and Meynet G. (2012) *A&A, 545*, A4. [17] Kastner J. and Myers P. (1994) *ApJ, 421*, 605-615. [18] Boss A. (2006) M&PS, 41, 1695-1703. [19] Tang H. and Dauphas N. (2015) *ApJ, 802*, 22. [20] Palacios A. et al. (2005) *A&A, 429*, 613P. [21] Dwarkadas V. (2005) *ApJ, 630*, 892 [22] Dwarkadas V. and Rosenberg D. (2013) *HEDP, 9*, 226. [23] Dwarkadas V. (2016a) *ApJ*, in preparation. [24] Ekstrom, S. et al (2012), *A&A, 537*, A146 [25] Dwarkadas V. (2016b) *ApJ*, in preparation. [26] Bojazi M. and Meyer B. (2016) *LPSC 47*.

RESOLVING THE ANCESTRY OF GEMS WITH CHILI. K. L. Villalon[1,2,3], H. A. Ishii[4], J. P. Bradley[4], T. Stephan[1,2,3], and A. M. Davis[1,2,3,5]. [1]Department of the Geophysical Sciences, The University of Chicago, Chicago, IL, USA, [2]Chicago Center for Cosmochemistry, [3]Robert A. Pritzker Center for Meteoritics and Polar Studies, Field Museum of Natural History, Chicago, IL, USA, [4]Hawaiʻi Institute of Geophysics & Planetology, University of Hawaiʻi at Mānoa, Honolulu, HI, USA, [5]Enrico Fermi Institute, The University of Chicago, Chicago, IL, USA. E-mail: kvillalon@uchicago.edu.

Introduction: Glass with Embedded Metal and Sulfides (GEMS) are amorphous silicate grains that are a common and abundant constituent of primitive interplanetary dust particles (IDPs) [1]. The question still remains as to their location and mechanism of formation. The similarities between the chemical and physical properties of GEMS and interstellar silicates—such as their sizes, shapes, structures, and chemical compositions—led to the proposition that GEMS are the interstellar products of isotopic and chemical (partial) homogenization of isotopically anomalous, circumstellar grains by sputtering due to heavy irradiation in conjunction with recondensation of previously sputtered material [1]. If this hypothesis is correct, GEMS are interstellar material and would therefore provide critical insight into processes acting on grains in the interstellar medium (ISM). They may potentially display a gradient of properties outlining the lives of such grains from the time they leave their host stars until they are incorporated into a protoplanetary disk. A competing hypothesis argues that GEMS formed in the solar nebula by late-stage, non-equilibrium condensation [2]. If this is the case, GEMS are instrumental in understanding early Solar System processes. In either case, they are an integral component of primitive solids.

Large isotopic anomalies verify presolar—and thus interstellar—origins, though solar isotopic composition does not preclude a presolar origin. Exposure to radiation can homogenize and effectively erase presolar isotopic signatures and some presolar grains may also initially condense with isotopically solar compositions. Some GEMS have mineral cores that have been interpreted as being either relict circumstellar material or solar nebula condensation nuclei. These mineral cores are primarily olivine or pyrrhotite and less commonly enstatite or kamacite [3]. If they are indeed relict, they may retain large isotopic anomalies. Several GEMS have been confirmed to be presolar based on their O isotopic compositions [2]; however, with sizes ranging from 100 to 500 nm with 5–10 nm inclusions, the majority of GEMS are too small to be spatially resolved from the highly abundant Solar System silicates with available techniques. It is therefore possible that the remaining GEMS are also presolar but their presolar signatures have been extensively homogenized or obscured due to analytical limitations. Furthermore, relict cores of pure iron sulfide or iron metal would not display anomalies in O isotopes. For these reasons, it is necessary to not only perform isotopic measurements with improved spatial resolution and sensitivity, but to expand the measurements to additional elements apart from O. To this end, we propose to measure the isotopic composition of GEMS from prescreened, minimally altered interplanetary dust particles using the recently completed CHILI instrument at the University of Chicago.

Instrumentation: The Chicago Instrument for Laser Ionization (CHILI) is a new nanobeam resonance ionization mass spectrometer (nano-RIMS) developed at the University of Chicago [4]. CHILI was designed to achieve an unprecedented lateral resolution of 10 nm and a useful yield of ~40%. CHILI has six tunable Ti:sapphire lasers that allow for the isotopic measurement of three elements simultaneously. With its higher spatial resolution coupled with its ability to eliminate isobaric interferences, the CHILI instrument will be far better equipped than current SIMS instruments to resolve the true isotopic composition of GEMS as well as presolar silicates, which may clarify the relationship, if any, between the two.

First analyses on natural samples were reported previously [5]. The Sr and Ba isotopic compositions were measured in presolar SiC grains by applying a 351 nm Nd:YLF desorption laser beam focused to ~1 μm. Though still being optimized, CHILI already outperforms previous generations of RIMS instruments. It is expected that CHILI will reach its design specifications within this year, and Fe and Ni isotopic measurements on natural samples are underway.

Scientific Considerations. If indeed presolar, the isotopic composition of GEMS with relict silicate cores should show a connection to presolar silicates. Oxygen isotope ratios are typically used to classify presolar silicates [6]; however, O cannot be analyzed using CHILI. Nevertheless, the stellar sources of many presolar silicates cannot be resolved by O isotopes alone. Unfortunately, their small size makes multi-element analyses difficult, so only a handful of other elements have been studied. Previous isotopic studies on the major elements Mg, Si, and Fe (see [7] and references therein) in presolar silicates have provided valuable insights but are sometimes ambiguous or conflict with nucleosynthetic models, likely owing at least in part to aforementioned limitations and thus should be revisited. Iron isotopic measurements by SIMS pose

an added problem as they suffer from isobaric interferences, a problem eliminated in RIMS.

The major elements (>1 at%) in GEMS are O, Si, Fe, Mg, S, Al, Ca, and Ni. Oxygen and S cannot be analyzed using CHILI. The remainder are favorable for analysis with CHILI due to their high elemental abundances. Minor and trace elements that have been measured in GEMS are Cr, Mn, and Ti [8]. Chromium and Ti, as well as yet undetected trace heavy elements such as Zr and Mo, may prove to be particularly diagnostic of the origins or conditions sustained by GEMS.

AGB stars are the most prolific producers of silicate dust and, correspondingly, most presolar silicates have O isotope ratios that reflect AGB origins with <10% coming from other sources such as supernovae [9]. Thus, elements that are sensitive to nucleosynthetic processes in AGB stars will be essential when analyzing presolar silicates and GEMS with CHILI, particularly main s-process elements. However, presolar GEMS with components reportedly originating from both low-mass AGB stars as well as supernovae (SNII) have been identified [2]. It is possible that many more GEMS than presolar silicates originate in supernovae or that the processing of GEMS in the ISM may have been uniquely shaped by frequent encounters in supernova shocks as proposed by [10]. These grains should instead show anomalies in the products indicative of explosive nucleosynthesis, such as large excesses in ^{28}Si. Though the exact site of the r-process is unknown, it likely occurs in core-collapse supernovae. Significant enrichments in r-process elements is therefore expected, particularly for A > 90 as a weak s-process signature may be present for A < 90 [11].

To date, no presolar silicates or GEMS have been analyzed for trace heavy elements such as Mo, Zr, Ba, or Sr. Previous RIMS work has been done on trace heavy elements in SiC grains, but O-rich grains such as silicates would probe different domains of star evolution than carbides and graphite. The s-process-only and r-process-only isotopes of such elements should be diagnostic of AGB and supernovae origins, respectively, and would provide important constraints on these nucleosynthetic processes. Zirconium, for example, would be a favorable element to study as it has four s-only isotopes (^{90}Zr, ^{91}Zr, ^{92}Zr, and ^{94}Zr) as well as one r-only isotope (^{96}Zr).

GEMS may store a memory of extinct short-lived radionuclides through their decay products, such as ^{60}Fe, ^{26}Al, and ^{44}Ti. Nickel-60 excesses due to the decay of ^{60}Fe have yet to be detected in presolar grains as a very high Fe/Ni ratio or very high-precision measurements are required. The enhanced Fe contents in presolar silicates and GEMS coupled with the advanced analytical capabilities of CHILI may make this detection more feasible [12]. Similarly, ^{26}Mg excesses due to extinct ^{26}Al or ^{44}Ca excesses due to extinct ^{44}Ti

may also be detectable. Titanium-44, a short-lived radionuclide that decays to ^{44}Ca with a half-life of 60 days, is only synthesized in supernovae. If GEMS formed in a supernova environment, excesses in ^{44}Ca would provide strong evidence for this.

Isotopic anomalies due to relict pyrrhotite grains would be an important discovery. Iron sulfides have been observed around pre- and post-main sequence stars but appear to be strongly depleted in ISM dust. Irradiation experiments have found that FeS, unlike silicates, is highly radiation resistant. Accordingly, presolar FeS should be close in abundance to presolar silicates [13]. The apparent depletion of FeS in ISM dust may simply be due an observational bias, yet no presolar iron sulfides have been discovered so far. It is possible that iron sulfides are not produced in appreciable quantities in stellar outflows or that another mechanism destroys them. It is also possible that GEMS are the hosts of the missing presolar iron sulfides.

Outlook: CHILI is nearing completion and will be prepared to measure the more abundant elements Fe and Ni in GEMS followed by trace heavy elements Sr, Zr, and Ba. At a later time, isotopes of other elements such as Mg, Al, Ca, Ti, Cr, and Mo will be considered. Complementary studies of the isotopic composition of presolar silicates will also be undertaken to clarify not only the stellar sources of these grains, but also the nature of their relationship to GEMS.

References: [1] Bradley J. P. (1994) *Science, 90*, 1151–1154. [2] Keller L. P. and Messenger S. (2011) *GCA, 75*, 5336–5365. [3] Bradley J. P. and Dai Z. R. (2004) *ApJ, 617*, 650–655. [4] Stephan T. et al. (2014) *LPS 45,* #2242. [5] Stephan T. et al. (2015) *LPS 46,* #2825. [6] Nittler L. R. et al. (1997) *ApJ, 483*, 475. [7] Zinner E. (2014) *Treatise on Geochemistry, 2nd Ed.*, 181–213. [8] Bradley J. P. and Dai Z. R. (2009) *M&PS, 44*, 10, 1627–1642. [9] Nguyen A. N. and Messenger S. (2014) *ApJ, 784*, 149. [10] Westphal A. J. and Bradley J. P. (2004) *ApJ, 617*, 1131. [11] Meyer B. S. et al. (1997) *Adv. Spac. Res., 19*, 729–738. [12] Davis A. M. and Gallino R. (2006) *MemSAIt, 77*, 885. [13] Keller L. P. et al. (2010) *LPS 41,* #1172.

OXYGEN ISOTOPE VARIATION WITH CRYSTAL GROWTH OBSERVED IN ALLENDE COARSE-GRAINED TYPE B CAI TS34 -REVISITED-.

N. Kawasaki[1], H. Yurimoto[1], S. B. Simon[2] and L. Grossman[2], [1]Natural History Sci. Hokkaido Univ., Sapporo 001-0021 Japan (yuri@ep.sci.hokudai.ac.jp), [2]Dept. of Geophysical Sci., Univ. of Chicago, Chicago, IL 60637 USA.

Introduction: The Allende type B1 CAI TS34 is one of the most well-studied CAIs in the solar system [1]. In typical CAI fashion, oxygen isotopes are distributed heterogeneously among the constituent minerals along a slope-1 line on an oxygen three-isotope diagram. Although TS34 has an igneous texture, oxygen isotope trends among the minerals do not follow the equilibrium crystallization sequence expected for CAI melt composition [2]. It is not easy to see how the oxygen isotope heterogeneity could have been caused by oxygen isotope exchange by solid-state diffusion after CAI solidification because of the oxygen self-diffusivities in the minerals [3, 4]. In fact, oxygen isotopes measured in Al-Ti-rich clinopyroxene in another coarse-grained type B CAI with intermediate ^{16}O-enrichment did not show any diffusion exchange profile for oxygen isotopes [5]. Evidence of oxygen isotope exchange during melting and recrystallization by temporal heating in the solar nebula is observed within melilite crystals in coarse-grained type A CAIs [6, 7]. Here, we revisit the TS34 CAI to measure the oxygen isotope distribution with careful petrographic control, and propose a new mechanism to form the oxygen isotopic distribution observed in the CAI.

Experimental methods: The Type B1 CAI, TS34, is included in a polished thin section of the Allende CV3 carbonaceous chondrite. The polished thin section was coated with a carbon thin film (~20 nm) for backscattered electron (BSE) imaging and elemental analysis using an energy dispersive X-ray spectrometer (EDS), and coated with a gold thin film (~70 nm) for oxygen isotope measurements using SIMS.

BSE images were obtained using a field emission type scanning electron microscope (FE-SEM; JEOL JSM-7000F) at Hokkaido University. Quantitative elemental analysis and X-ray elemental mapping were conducted using an energy-dispersive spectrometer (EDS, Oxford X-Max 150) installed on the FE-SEM.

Oxygen isotopic compositions of the minerals in TS34 were measured using the SIMS instrument (Cameca ims-1280HR) at Hokkaido University. A ^{133}Cs$^+$ primary beam (20 keV, 60 pA) with a diameter of 2–3 μm was used. Negative secondary ions were measured simultaneously in the multicollection mode. A normal incident electron flood gun was used for the electrostatic charge compensation. The mass resolution $M/\Delta M$ for ^{17}O$^-$ was set at ~6000, while that for ^{16}O$^-$ and

^{18}O$^-$ was ~2000. The intensity ratios measured were corrected to δ-SMOW values using terrestrial standards.

Results and Discussion: The TS34 CAI mainly consists of melilite, Al-Ti-rich clinopyroxene and spinel [1, 8-11] in an igneous texture. Oxygen isotopic compositions of the minerals plot along a slope-1 line (Fig. 1). Spinel is ^{16}O-rich, whereas melilite ^{16}O-poor, which are consistent with previous results [1, 9]. On the other hand, Al-Ti-rich clinopyroxene crystals have various degrees of ^{16}O-enrichments between O isotopic compositions of spinel and melilite. In order to clarify systematics of the oxygen isotopic variation, we mapped the spatial heterogeneity of the oxygen isotopes within a pyroxene crystal.

Blocky Al-Ti-rich clinopyroxene crystals are abundant in TS34 CAI. Chemical zoning of Ti reveals the direction of crystal growth. The pyroxene grew from Ti-rich to Ti-poor compositions with gradual chemical zoning as shown in the contour lines of Fig. 2. Oxygen isotopic compositions were measured along lines A-B and A-C traversing crystal growth contours. Point A corresponds to the start of crystal growth and points B and C correspond to the ends of crystal growth for the pyroxene.

The pyroxene crystal covers the entire variation range of oxygen isotopic compositions observed in the TS34 CAI. Crystal growth began with an ^{16}O-poor composition that is isotopically in equilibrium with
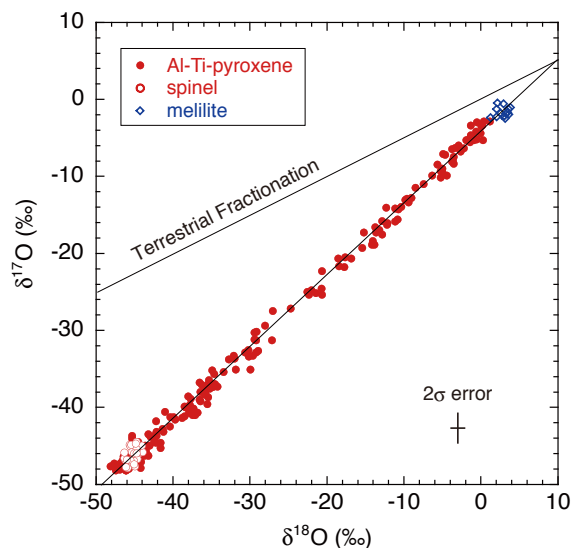

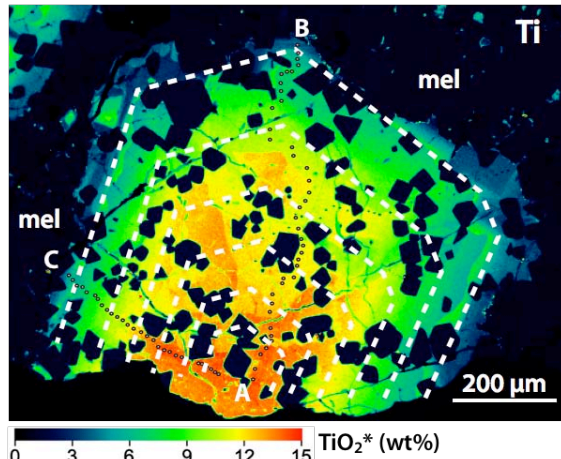Fig. 1. Oxygen isotope compositions of minerals in TS34.

Fig. 2. Ti elemental map of Al-Ti-rich clinopyroxene in TS34. The pyroxene contains spinel (black) inclusions and is surrounded by melilite (black). Dashed lines show growth contours. Small dots between A-B and A-C show measurement points for O isotope analysis.

Fig. 3. Oxygen isotope variation within the clinopyroxene crystal shown in Fig. 2. Lines A-B and A-C are shown in Fig. 2. The crystal started ^{16}O-poor (inside inner growth contour) and ended ^{16}O-rich (outside outer contour).

melilite (Fig. 3). As the crystal grew, the oxygen isotopic composition gradually became ^{16}O-rich along the slope-1 line and approached the solar O isotopic signature [12-14]. The bulk O isotopic composition of pyroxene is relatively ^{16}O-rich, consistent with results from mineral separates [1], because the volume proportion of ^{16}O-poor compositions is relatively small.

The oxygen isotopic distribution in pyroxene correlates with the O isotopic evolution of the liquid in the CAI. The oxygen isotopic composition of the liquid was ^{16}O-poor when the liquid equilibrated with melilite and the earliest pyroxene. The ^{16}O-rich spinel are relict crystals [2] that preserve a record of isotopic disequilibrium. As the temperature fell, the liquid crystallized pyroxene with increasingly ^{16}O-rich composition. The ^{16}O-rich signature must have been introduced from outside the CAI because there are no available reservoirs within the CAI. The surrounding gas is the most plausible candidate for the ^{16}O-rich source because O is the most abundant element in the gas after H and He. Oxygen isotopic variation of the gas surrounding CAIs is supported by measurements of directly condensed minerals of CAIs [15-19]. The oxygen isotopic variations observed in the TS34 CAI suggest that the gas changed cyclically from ^{16}O-rich (spinel), ^{16}O-poor (melilite, early pyroxene) and then ^{16}O-rich (late pyroxene) in the early solar system. Oxygen isotopic contrast between the Sun and the solar protoplanetary disk, i.e., having solar and planetary signatures, respectively, has been derived by a model [20]. A boundary between the contrasting reservoirs may have existed at the inner edge of the protoplanetary disk [21]. Preservation of oxygen isotopic variations requires melting and recrys-

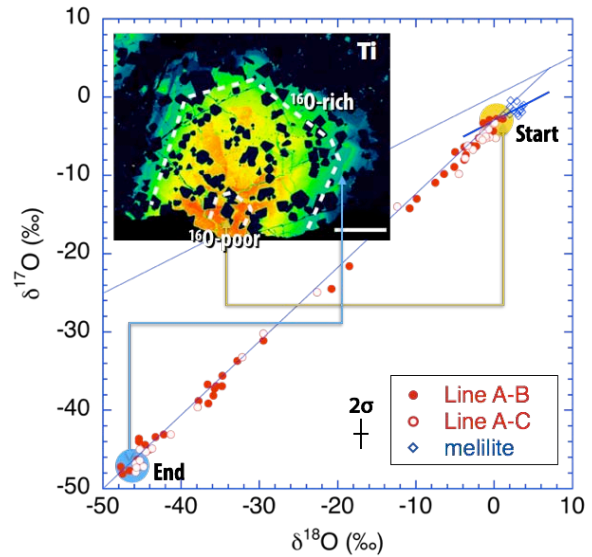tallization that may have been caused by giant flares from the protosun [22].

References: [1] Clayton, R.N. et al. (1977) *Earth Planet. Sci. Lett. 34*, 209-224. [2] Stolper, E. (1982) *Geochim. Cosmochim. Acta 46*, 2159-2180. [3] Yurimoto, H. et al. (1989) *Geochim. Cosmochim. Acta 53*, 2387-2394. [4] Ryerson, F.G. and McKeegan, K.D. (1994) *Geochim. Cosmochim. Acta 58*, 3713-3734. [5] Yurimoto, H. et al. (1994) *Earth Planet. Sci. Lett. 128*, 47-53. [6] Yurimoto, H. et al. (1998) *Science 282*, 1874-1877. [7] Aléon, J. et al. (2007) *Earth Planet. Sci. Lett. 263*, 114-127. [8] Simon, S.B. et al. (1991) *Geochim. Cosmochim. Acta 55*, 2635-2655. [9] Connolly, H.C. et al. (2003) *Meteorit. Planet. Sci. 38*, 197-224. [10] Simon, S.B. and Grossman, L. (2006) *Geochim. Cosmochim. Acta 70*, 780-798. [11] Paque, J.M. et al. (2013) *Meteorit. Planet. Sci. 48*, 2015-2043. [12] Kobayashi, S. et al. (2003) *Geochem. J. 37*, 663-669. [13] Fujimoto, K. et al. (2009) *Geochem. J. 43*, e11-e15. [14] McKeegan, K.D. et al. (2011) *Science 332*, 1528-1532. [15] Yoshitake, M. et al. (2005) *Geochim. Cosmochim. Acta 69*, 2663-2674. [16] Simon, J. I. et al. (2011) *Science 331*, 1175-1178. [17] Katayama, J. et al. (2012) *Meteorit. Planet. Sci. 47*, 2094–2106. [18] Kawasaki, N. (2012) *Meteorit. Planet. Sci. 47*, 2084–2093. [19] Park, C. (2012) *Meteorit. Planet. Sci. 47*, 2070–2083. [20] Yurimoto, H. and Kuramoto, K. (2004) *Science 305*, 1763-1766. [21] Yurimoto, H. et al. (2008) *Rev. Mineral. Geochem. 68*, 141-186. [22] Nakamoto, T. et al. (2005) in: Krot, A.N., Scott, E.R.D., Reipurth, B. (Eds.), *Chondrules and the Protoplanetary Disk*, pp. 883-892.

METEORITIC Nd ISOTOPE CONSTRAINTS ON THE ORIGIN AND COMPOSITION OF THE EARTH.

C. Burkhardt[1,2], L.E. Borg[3], G.A. Brennecka[2,3], Q.R. Shollenberger[2,3], N. Dauphas[1], T. Kleine[2], [1]Origins Laboratory, Department of the Geophysical Sciences and Enrico Fermi Institute, The University of Chicago, 5734 South Ellis Avenue, Chicago, IL 60637, USA (burkhardt@uni-muenster.de). [2]Institut für Planetologie, Westfälische Wilhelms-Universität Münster, Wilhelm Klemm-Strasse 10, 48149 Münster, Germany. [3]Lawrence Livermore National Laboratory, L231, Livermore, CA 94550, USA.

Introduction: Precise and accurate knowledge of a planet's bulk chemical and isotopic composition is essential for unraveling its geologic history by geochemical means. For a differentiated planet like the Earth, whose bulk composition cannot be determined directly, these values are approximated using chondrites – undifferentiated primitive meteorites that are thought to represent the building blocks of the terrestrial planets.

However, the discovery of excess ^{142}Nd in the Earth's mantle relative to primitive meteorites [1] challenged this "chondritic Earth" paradigm, because, if interpreted as a result of ^{146}Sm decay (^{146}Sm $\rightarrow$ ^{142}Nd; $t_{1/2}$ = 103 Ma), this offset seems to require evolution of the accessible Earth with a super-chondritic Sm/Nd since at least 4.53 Ga. Mass balance then requires the existence of a reservoir with sub-chondritc Sm/Nd; this reservoir has never been sampled and either has been lost to space by impact erosion of early-formed crust [2] or was sequestered to the deep Earth [1].

Both of these scenarios have far-reaching implications for our understanding of the Earth and initiated a complete re-assessment of how we think the Earth evolved through geologic time (*e.g.*, [2, 3]). However, all these prior studies relied on the assumption that the ^{142}Nd offset between Earth and chondrites is of chronological significance, *i.e.*, caused by an early Sm/Nd fractionation, followed by decay of ^{146}Sm to ^{142}Nd.

Here we investigate an alternative explanation for the ^{142}Nd excess in the Earth relative to chondrites, namely nucleosynthetic isotope heterogeneity between chondrites and the Earth. Using high precision Nd and Sm isotope measurements of planetary materials, we will quantify nucleosynthetic Nd isotope variations between chondrites and the Earth, with the ultimate goal to determine whether any of the difference in ^{142}Nd between the accessible Earth and chondrites is attributable to radiogenic ingrowth.

Materials and Methods: We analyzed a variety of ordinary and enstatite chondrites, the carbonaceous chondrite Allende, the ungrouped primitive achondrite NWA 5363, as well as a Ca,Al-rich inclusion (CAI) from the Allende meteorite. In order to avoid potential artifacts associated with the incomplete dissolution of refractory presolar components and to minimize disturbances through terrestrial alteration, only equili-brated chondrites (petrologic classes 4-6, except Allende CV3) from observed falls were selected for this study. Compared to previous studies, we digested larger sample sizes (~2 g), which allowed us to obtain higher precision isotope data, particularly for the non-radiogenic Nd isotopes.

All measurements were performed by TIMS at LLNL. Neodymium isotope ratios were measured using a two mass-step procedure that calculates ^{142}Nd/^{144}Nd and ^{148}Nd/^{144}Nd dynamically, while measuring the other Nd isotopes statically. Fractionation was corrected relative to ^{146}Nd/^{144}Nd = 0.7219 using the exponential law. The absence of analytical artifacts in our procedures is demonstrated by the analyses of terrestrial standards (BHVO-2, BIR-1, JNdi-1), which were processed along with the samples and whose measured isotope compositions are indistinguishable from the unprocessed JNdi-1 Nd and AMES Sm standards.

Results: Most samples show well-behaved ^{147}Sm-^{143}Nd systematics and fall on a 4.568 Ga isochron. The mean ^{147}Sm/^{144}Nd and ^{143}Nd/^{144}Nd values defined by the chondrites are in good agreement with the current best estimate of the average chondritic values [4]. The ^{142}Nd/^{144}Nd data of the meteorites fall mostly below a 4.568 Ga isochron constructed through the accessible Earth and a chondritic ^{147}Sm/^{144}Nd = 0.1960, and only poorly correlate with Sm/Nd. After correction to a common ^{147}Sm/^{144}Nd = 0.1960, the µ^{142}Nd (ppm deviation relative to the JNdi-1 standard) values range from -9±5 (95% c.i.) for enstatite chondrites to -31±1 for the Allende carbonaceous chondrite. This is consistent with prior observations [5-7] and indicates that the ^{142}Nd/^{144}Nd of chondrites does not only reflect Sm/Nd fractionation and ^{146}Sm decay. Evidence for the process responsible for the ^{142}Nd variations in chondrites comes from the non-radiogenic Nd isotopes, for which our new data show resolved systematic and positively correlated anomalies (Fig. 1). These anomalies were not resolved in previous studies because the measurements were of insufficient precision. The anomalies increase in the order: enstatite chondrites, carbonaceous chondrites, ordinary chondrites, NWA 5363.

Discussion: The anomalies in non-radiogenic Nd isotopes plot along mixing lines between terrestrial Nd and *s*-process Nd as obtained from *s*-process model
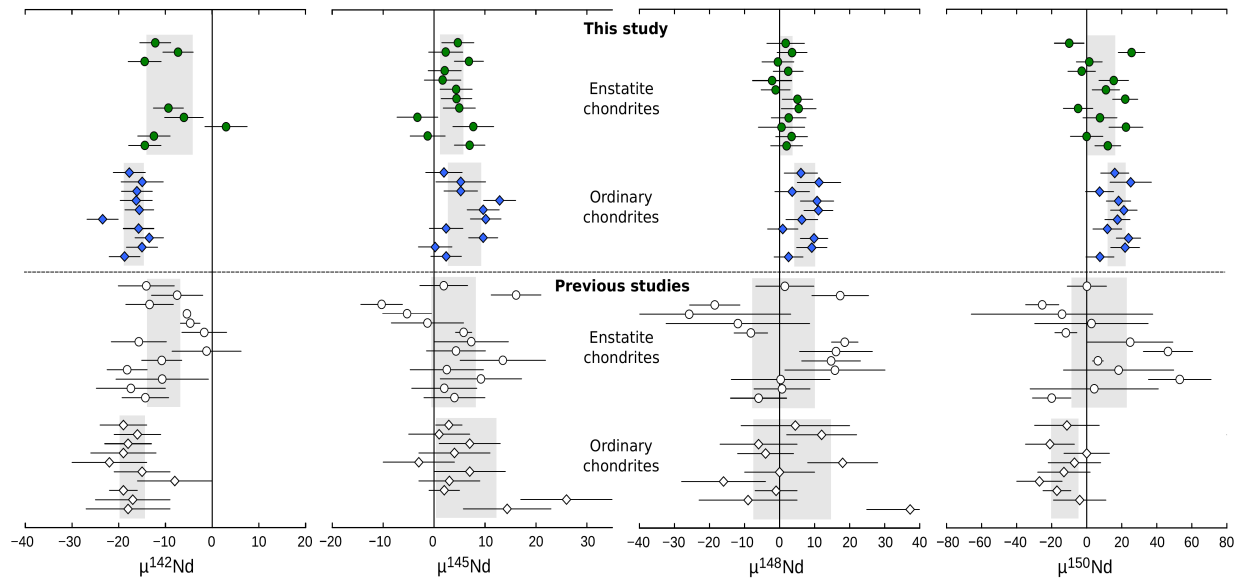
Fig. 1: $\mu^{142}Nd$, $\mu^{145}Nd$, $\mu^{148}Nd$ and $\mu^{150}Nd$ values of enstatite and ordinary chondrites from this study (solid symbols) compared to data from previous studies (open symbols) [1, 5-7]. Our new data show much less scatter, particularly in the non-radiogenic Nd isotopes, and hence, more precisely defined mean values. Grey bars represent 95% c.i. of mean of each chondrite group.

calculations, data from presolar SiC grains, or chondrite leachates. This implies that the meteorites are characterized by variable depletions in *s*-process Nd relative to the Earth, an observation that is consistent with inferences from other isotope systems, *e.g.*, Mo, Ru and Zr [8-10]. However, while for these other systems the nucleosynthetic anomalies are typically largest in carbonaceous chondrites, the $\mu^{145}Nd$, $\mu^{148}Nd$ and $\mu^{150}Nd$ values of Allende are similar to those of enstatite and ordinary chondrites. These subdued Nd anomalies in Allende can be explained by the presence of CAIs, which host about half of all the Nd (and Sm) in Allende and are characterized by an *s*-excess in the non-radiogenic Nd isotopes [11]. A CAI-free carbonaceous chondrite composition obtained by mass balance, therefore, exhibit significantly larger $\mu^{145}Nd$, $\mu^{148}Nd$ and $\mu^{150}Nd$ anomalies.

The information obtained from the non-radiogenic Nd isotopes allows quantification of nucleosynthetic contributions to measured $\mu^{142}Nd$ anomalies in the chondrites. The $\mu^{142}Nd$ values of the meteorites are inversely correlated with $\mu^{145}Nd$, $\mu^{148}Nd$ and $\mu^{150}Nd$. Enstatite and ordinary chondrites, as well as NWA5363, plot on mixing lines between the terrestrial composition and *s*-process Nd. Allende deviates from this lines due to admixture of CAIs. Mass balance indicates that a CAI-free carbonaceous chondrite source composition also plots well on the *s*-process correlation line defined by the other chondrites. Regressions of the bulk mete-

orite data yield slopes that are indistinguishable from those obtained for *s*-process mixing lines, and their $\mu^{142}Nd$ intercept values are indistinguishable from the terrestrial value at the current level of precision.

Conclusion: Our data indicates that compared to chondrites, the Earth accreted from material enriched in Nd isotopes produced by the *s*-process of nucleosynthesis. Once this nucleosynthetic effect is taken into account, the Earth and chondrites seem to have indistinguishable ^{142}Nd compositions. This suggests that the Earth has a chondritic Sm/Nd ratio and as such supports the long-standing paradigm of a chondritic composition of the Earth. Thus, our results obviate the need for collisional erosion of early-formed crust or the presence of a hidden reservoir within the deep Earth.

References: [1] Boyet M. and Carlson R.W. (2005) *Science* 309, 576-581. [2] Campbell I.H. and O'Neill H.S.C. (2012) *Nature* 483:553-558. [3] Jellinek A.M. and Jackson M.G. (2015) *Nature Geoscience* 8:587-593. [4] Bouvier A. et al., (2008) *EPSL* 273:48-57. [5] Carlson R.W. et al., (2007) *Science* 316:1175-1178. [6] Andreasen R. and Sharma M. (2006) *Science* 314, 806-809. [7] Gannoun A. et al., (2011) *PNAS* 108:7693-7697. [8] Burkhardt C. et al., (2011) *EPSL* 312:390-400. [9] Fischer-Gödde et al., (2015) *GCA* 168:151-171. [10] Akram W. et al., (2015) *GCA* 165:484-500. [11] Brennecka G.A. et al., (2013) *PNAS* 110:17241-17246.

INVESTIGATIONS INTO THE FORMATION MECHANISMS OF CM HIBONITES AT THE MICRO-TO NANOSCALE USING THE SEM AND TEM L. Kööp[1,2,4], A. M. Davis[1,2,3,4], S. S. Rout[2,4], K. L. Villalon[1,2,4], and P. R. Heck[1,2,4], [1]Department of the Geophysical Sciences, [2]Chicago Center for Cosmochemistry, [3]Enrico Fermi Institute, University of Chicago, Chicago, IL, [4]Robert A. Pritzker Center for Meteoritics and Polar Studies, Field Museum of Natural History, Chicago, IL (E-mail: koeoep@uchicago.edu)

Introduction: Hibonite (Hib)-rich CAIs from CM chondrites such as PLACs (platy hibonite crystals), SHIBs (spinel-hibonite inclusions), and fractionated Hib-rich objects show a remarkable variety of isotopic properties [1,2], indicating that they record snapshots of the isotopic homogenization of the early solar nebula. For example, PLACs and related Hib-rich CAIs are [26]Al-depleted and show a large range of nucleosynthetic anomalies (>100‰) [1,2]. In contrast, SHIBs and highly fractionated Hib-rich CM CAIs show a range of inferred [26]Al/[27]Al ratios (0–supracanonical), with smaller nucleosynthetic anomalies than in PLACs [1,2,3].

Contrary to many other types of CAIs, there is a fairly good relationship between the isotopic character and petrologic features of Hib-rich CAIs [e.g., 1]. For example, (1) PLACs rarely contain spinel (Sp) and (2) the MgO and TiO_2 abundances are more restricted and on average lower in PLACs than in SHIB Hibs. While these petrological differences are likely indicative of different formation conditions, the formation processes of Hib-rich CAIs have remained controversial. In particular, both melt [4] and direct condensation [5] origins have been considered for PLACs. The nature of their formation mechanism(s) is an important consideration for the interpretation of isotopic data, as it could help distinguish between mass-dependent and nucleosynthetic variations (e.g., for O isotopes [6]).

Taking advantage of an isotopically well-characterized set of Hib-rich CM CAIs [e.g., 3,6–8], we have started to investigate the structure and chemistry of these CAIs on a finer scale. Our goal is to evaluate if distinct petrologic differences exist that might help to identify the formation mechanism(s) of these CAIs. Here, we present initial results for a PLAC and a SHIB.

Samples and methods: CAI 2-7-1 is a PLAC and appears as a single crystal of Hib in the polished section (Fig. 1a). It was chosen for this study because of its margin, which consists of Sp and perovskite (Pv; Fig. 1a). FeO-rich silicate material is present along one edge of the CAI (likely matrix or an altered rim; Fig. 1a). This CAI has no resolvable radiogenic [26]Mg excess, and no resolvable anomalies in Ti or Ca isotopes [7,8].

CAI 1-9-5 (Fig. 1b) is a SHIB with a $\Delta^{17}O$ value of ~−23‰, with no significant displacement from the CCAM line [6]. It was chosen for this study because it contains multiple refractory metal nuggets (RMNs; compositions were presented in [9]).
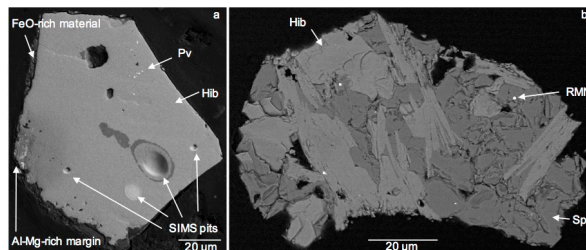
Figure 1. BSE images of PLAC 2-7-1 (a) and SHIB 1-9-5 (b).

Both CAIs were separated from the Murchison meteorite (2-7-1 from ME 2644, 1-9-5 from ME 2752, both from the Field Museum collection) by freeze-thaw disaggregation and density separation. ME 2752 was also treated with HF-HCl. The CAIs were mounted in epoxy and polished. The scanning electron microscopy (SEM) and focused ion beam (FIB) work presented here was performed with a JEOL JSM-5800LV SEM and a Tescan LYRA3 FIB-SEM at the University of Chicago, the latter is equipped with Oxford Nordlys-Max[2] electron backscatter diffraction (EBSD) and Oxford XMax energy-dispersive x-ray spectroscopy (EDS) detectors. In addition to EBSD, which was performed at a 70° sample tilt angle, the system allows transmission Kikuchi diffraction (TKD), which was performed at a 20° tilt.

Electron transparent lamellae were extracted from both samples by FIB lift-out. For 2-7-1, a protective layer of Pt was deposited prior to lift-out, and the lamella was attached to a copper grid using Pt. The lamella extracted from 1-9-5 was attached to a copper grid using C to avoid Pt contamination of the RMNs. Both lamellae were thinned to electron transparency using a 30 keV Ga^+ beam and final polishing was done with a 2 keV Ga^+ beam. The lamella of 1-9-5 was imaged with a 300 kV FEI Tecnai F30 G2 transmission electron microscope (TEM) at the University of Chicago.

Results and discussion: *2-7-1:* Figure 2a shows that the margin of 2-7-1 consists of Sp (confirmed by EBSD on polished mount and by TKD on the extracted lamella), which is pervaded by interwoven bands of submicron-sized Pv (confirmed by TKD on the extracted lamella). An EBSD map obtained on the polished mount shows the same orientation for Sp in this region. The boundary between Hib and the Sp is irregular (Fig. 2a) and the lamella reveals that the depth of the Sp-Pv assemblage is shallow (<1 μm; Fig. 2b). Below the assemblage is more Hib, followed by FeO-rich silicate

material that is similar to the material that is exposed at a different location in the polished mount (Fig. 1a). The silicate extends into the CAI, possibly along a grain boundary or cleavage plane.
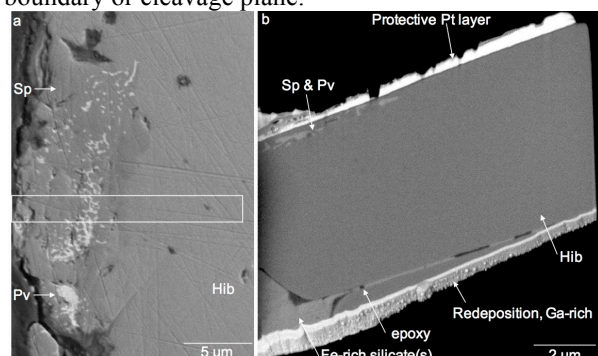

Figure 2. BSE images of the Sp- and Pv-bearing margin of PLAC 2-7-1 (a) and the lamella lifted out of 2-7-1 (b). The white box in (a) indicates the area that the lamella was lifted out from. The lamella is tilted relative to the post of the grid due to a problem with the gas injection system.

The Sp-Pv assemblage at the margin of this PLAC is of interest because it could be a result of high-temperature gas-solid reactions between Hib and the cooling solar nebula gas. Condensing Mg may have reacted with Hib to form Sp (taking up Al), while Pv formed to accommodate the other abundant cations not taken up by spinel, i.e., Ca and Ti. The interwoven texture of Pv and Sp may support such a scenario. A reaction between Hib and the gas was also favored by [10] for the origin of Sp-Hib-bearing CAIs from a CO chondrite, but Pv grains in these CAIs are usually larger and not part of a pervasive network as observed here. If 2-7-1 is a condensate, the lack of resolvable anomalies in Ca and Ti in this [26]Al-depleted CAI may indicate that isotopic anomalies were efficiently homogenized in the gas phase before condensates formed.

1-9-5: The lamella lifted out of SHIB 1-9-5 contains multiple Hib and Sp crystals as well as one RMN enclosed within a single Sp crystal (Fig. 3a). Sp crystals are anhedral, with rounded Sp-Sp boundaries. Bright-field TEM images of the Hib grains in 1-9-5 commonly show straight lines parallel to the elongation direction of the crystals (Fig. 3b), which could be the result of lattice stacking faults as observed by [10]. The diameter of the RMN is ~300 nm (Fig. 3c), but it was larger before final thinning of the lamella. EDS analyses of this RMN (in wt%: Mo 20, Ru 18, Os 17, Ir 14, Pt 12, Fe 8, Rh 4, W 3, Re 3, Ni 1) are within the typical range of RMNs in SHIBs [9]. TKD shows that the studied RMN has a hexagonal structure (Space Group $P6_3/mmc$). The RMN does not appear uniform in bright-field (Fig. 3c); instead, it shows small dark areas towards the edge of the RMN. At this point, it is not clear whether this is a

preparation artifact or a result of chemical heterogeneity within the RMN.
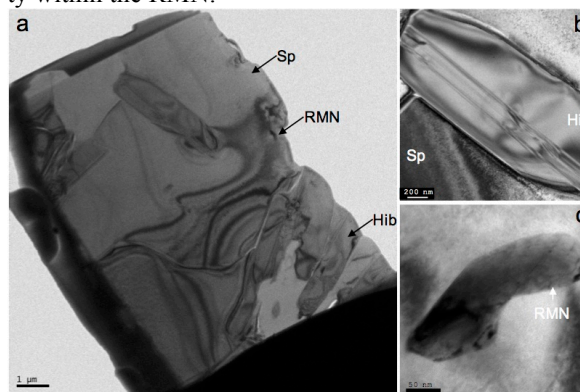
Figure 3. TEM bright-field images of the lamella from SHIB 1-9-5. a) Overview. b) Magnification of a hibonite grain. c) The RMN, set within a Sp grain.

Conclusion and outlook: The relationship between Hib, Sp and Pv in PLAC 2-7-1 may be indicative of a gas-solid reaction between Hib and the cooling solar nebula gas. Further TEM work is planned to look for traces of melilite, which is expected to occur before Sp during equilibrium condensation and could be present on the TEM scale as observed for CO CAIs by [10].

A condensation origin of 2-7-1 could support a scenario in which condensate CAIs are isotopically homogenized due to efficient mixing in the gas phase. However, additional work is needed, for example, to evaluate whether condensation features are absent in isotopically anomalous PLACs.

The hexagonal structure inferred from TKD for the RMN in SHIB 1-9-5 is in agreement with the structure of RMNs inferred by TEM [11]. This suggests that TKD is a useful tool for microstructural investigations of RMNs. We plan to apply TKD to other RMNs, especially from mass-fractionated Hibs, which have refractory compositions but are devoid of Mo and W [9].

We further plan to extend the study of the lamella lifted out of SHIB 1-9-5. The presence of RMNs in this CAI may indicate that it formed by melting [9], making it suitable for comparing and contrasting it to possible gas-solid condensate Hibs.

References: [1] Ireland T. (1990) *GCA, 54*, 3219-3237. [2] Liu M.-C. et al. (2009) *GCA, 73*, 5051–5079. [3] Kööp L. et al. (2015) *LPI Contrib. 1832,* #2750. [4] Ireland T. et al. (1988) *GCA, 52*, 2841-2854. [5] Hinton et al. (1987) *ApJ, 312*, 420–428. [6] Kööp L. et al. (2014) *LPI Contrib., 1777,* #2508. [7] Kööp L. et al. (2014) *LPI Contrib., 1800,* #5384. [8] Kööp L. et al. (2015) *LPI Contrib., 1856,* #5225. [9] Schwander D. et al. (2015) *GCA, 168*, 70–87. [10] Han J. et al. (2015) *MAPS, 50*, 2121–2136. [11] Harries D. et al. (2012) *MAPS, 47,* 2148–2159.

TRACING SOLIDS AND VAPOR DURING PARTICLE GROWTH: COMMUNICATION BETWEEN THE MIDPLANE AND SURFACE LAYERS IN A PROTOPLANETARY DISK.

S. Krijt[1] and F. J. Ciesla[1], [1]Department of the Geophysical Sciences, The University of Chicago, 5734 South Ellis Avenue, Chicago IL 60637 (Email: skrijt@uchicago.edu)

Introduction: Protoplanetary disks around young stars serve as analogs for our own solar nebula, the cloud of dust and gas that circled the Sun after its formation and provided the raw materials for constructing the planets. A major issue in developing our models for planet formation is reconciling the astronomical observations of protoplanetary disk surfaces with meteoritic materials which presumably were sampling the solar nebula midplane. Differences in gas densities, temperatures, and photon fluxes would lead to differences in the physical and chemical evolution of materials in these environments. It is thus critical to understand not only how efficiently materials mix from one region to the other, but also how materials are processed and altered during transit.

Materials at the disk surface will be brought down to the disk midplane via a combination of diffusion and gravitational settling, while midplane materials can be lofted to the disk surface by diffusion. Here we extend the particle-tracking methods developed by [1] to explore how particle growth affects the ability of small grains to be transported from these different regions in the disk. We also explore how the vertical transport of grains leads to the vaporization/freeze-out of water ice on more refractory solids and the impact this has on the water vapor distribution in the disk.

Particle Growth: The vertical distribution of solids of a given size in a disk is described by the scale-height of the solid distribution, h_d, which is found by balancing the upward diffusive flux with the downward flux due to gravitational settling. For very small particles that are well coupled to the gas, $h_d \sim h_g$, where h_g is the scale-height of the gas. This implies that small particles will be distributed at a constant (small) dust-to-gas ratio throughout the height of the disk.

The consideration outlined above assumes that the distribution of solids is controlled by the two processes described. However, interactions with other particles has thus far been ignored. Small particles can collide with other solids and stick, forming increasingly larger aggregates. As these aggregates grow larger in size, their aerodynamic properties change, resulting in more efficient settling and less diffusion. This would lead to solids concentrating at the disk midplane, enhancing the dust-to-gas ratio locally, while depleting the dust from the disk surface layers.

Collisions between dust aggregates can also result in fragmentation or disruption, liberating small particles allowing them to again follow paths that have them strongly coupled to the gas. These fragmenting collisions are the primary source of small grains in more evolved protoplanetary disks and are necessary to explain the observed abundance of small grains in such systems [2].

While the coagulation of dust aggregates has been investigated previously [2-5] to determine the vertical distribution of particles as a function of size, we have developed a method to examine how individual particles are transported through the vertical height of the disk [6]. We use the particle-tracking methods of [1] to follow the dynamics of a given dust grain. Assuming a steady-state dust distribution as described by [5], for every displacement step a particle experiences, we determine a collision probability with the background dust distribution. When a collision occurs, we randomly select with which sized particle the grain collides. If the collision is deemed to be accretional, the dust grain is incorporated into a corresponding larger aggregate. If a collision occurs that results in fragmentation, we track one of the fragments, randomly chosen from the size distribution resulting from the collision. We then follow the dynamics and collisional history of the collision product, repeating the dynamical-collisional procedure.

Figure 1 shows the background dust population taken from the dust growth models of [4] used in our calculations. Here we consider a region of the disk at 5 AU, a gas surface density of 180 g/cm^2, a vertically-integrated dust-to-gas mass ratio of 0.01, a turbulent parameter of $\alpha=10^{-3}$ and a fragmentation velocity of 5 m/s. Figure 2 shows the dynamical and collisional lifetime of one of our tracked particles. The particle begins as a 0.1 μm grain at the disk midplane. Almost immediately, the monomer is incorporated into a larger grain, and in less than 1000 years finds itself in a grain ~1 mm in size. Over the 20,000 years of simulation, the monomer spends most of its time in objects of this size or larger, only occasionally being released as a small fragment as a result of an energetic collision. The lifetime of the small grains is short though (especially in the dense midplane), and it does not take long before the grain is incorporated into a larger aggregate again.

The large fraction of time spent in large bodies combined with the relatively short durations spent as a small grain limit the ability for the monomer to diffuse to high altitudes in the disk. Having run a large num-

ber of similar calculations, we find that for those bodies released at the disk midplane, all small particles (those which should be well coupled to the gas) have distributions with scale heights of $h_d \sim 0.7 h_g$, or 30% less than predicted when collisions are not taken into account. The discrepancy is greater in areas of low turbulence and high dust-to-gas ratios. Thus, transport of fine particles from the midplane to the disk surface is less efficient than previously recognized.

Ice Sublimation/Freeze-out: We are also exploring how the vertical distribution of volatiles in the gas phase may be affected over regions of condensation fronts. In passive protoplanetary disks, the lower temperatures and higher densities at the disk midplane would lead to volatiles, like water, freezing out onto grains while remaining as a gas in the lower density, warmer regions closer to the atmosphere that are heated by incident radiation from the star. Vapor may diffuse downward to freeze-out near the disk midplane, while being replenished as dust grains diffuse to the disk surface and desorb volatiles. The volatile abundance at the disk surface will be determined by the balance of these two processes.

We have begun exploring this issue by expanding our approach, allowing water molecules to desorb from/adsorb onto grains as they move through a vertical slice of the disk. Frozen out molecules then move with the grains that they adsorb onto, while molecules in the gas are diffused throughout the vertical extent of the disk, with their concentration tracked as a function of height.

The vapor concentration in the upper altitudes of a disk is intimately tied to the dynamical and collisional evolution of the dust at lower altitudes. As grains grow, fewer are lofted to heights where the water can desorb and return to the gas. As a result, water vapor concentrations would be depleted in regions of significant grain growth and settling. High vapor concentrations could then imply lack of dust growth/settling, or the absence of a condensation front at the disk midplane. Such depletions have been inferred for the surfaces of the ~10 Myr old disk TW Hya where a significantly evolved dust population is expected [7].

Discussion: The methods we have developed here show how both solids and volatiles are transported between the disk midplane, where meteorites formed, and the disk surface which is what is seen in astronomical observations. Such information is critical for finding ways of linking the data for these two fields as we can evaluate how processes operating in one region impact what is seen in another.

References: [1] Ciesla F. J. (2010) *ApJ, 723,* 514 [2] Dullemond C. P. and Dominik C. (2005), *A&A, 491,* 663 [3] Weidenschilling S. J. (1997), *Icarus, 127,*

29 [4] Ciesla F. J. (2007), *ApJ, 654,* L159 [5] Birnstiel T., Ormel C. W. and Dullemond C. P. (2011), *A&A, 525,* A11 [6] Krijt and Ciesla (2016), *ApJ, in prep.* [7] Du F., Bergin E. A., and Hogerhijde M. R. (2015), *ApJ, 807,* 32.
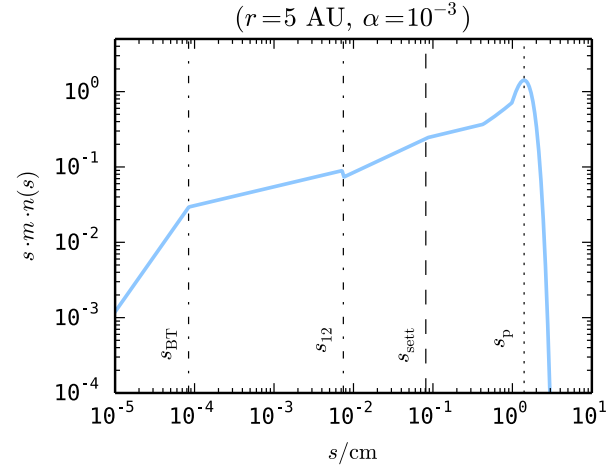

Figure 1: Normalized steady-state dust size distribution resulting from fragmentation-limited growth at 5 AU assuming a fragmentation velocity of 5 m/s. The largest aggregates, those with sizes ~1 cm, dominate the solid mass budget.
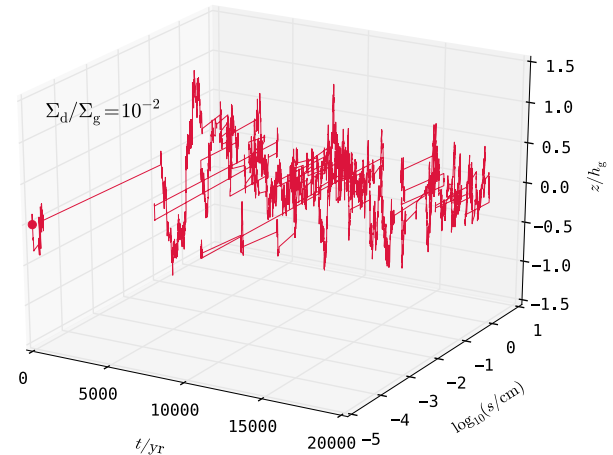

Figure 2: Simulated history of a 0.1 μm grain released at the midplane of a typical protoplanetary disk experiencing settling, diffusion and collisions with other aggregates. During the simulated 20,000 years, the monomer spends most of its time inside large mm- to cm-size aggregates and in a region relatively close to the disk midplane.

ORIGIN OF SEDIMENTARY-ROCK MOUNTAINS ON MARS CONSTRAINED BY LAYER-ORIENTATION DATA.

Jonathan Sneed[1], David P. Mayer[1], Kevin W. Lewis[2], Edwin S. Kite[1] (kite@uchicago.edu).
[1]University of Chicago, [2]Johns Hopkins University.

Summary: The tallest sedimentary-rock mountains on Mars sit within Valles Marineris. We use 200 HiRISE DTM layer orientation measurements to show that layers within the mountains systematically dip away from the mountain crest-lines. These data are not consistent with with tilting of initially horizontal sediments by compaction, flexure, or crustal-flow. The data are also not consistent with delta-foreset deposition (with sediment sourced from canyon walls). The data are consistent with: upwarping of the mountains by linear canyon-centered diapirs, with selective dissolution/dehydration of outer layers during mountain formation, or with enhanced erosion by slope winds.

Predictions:
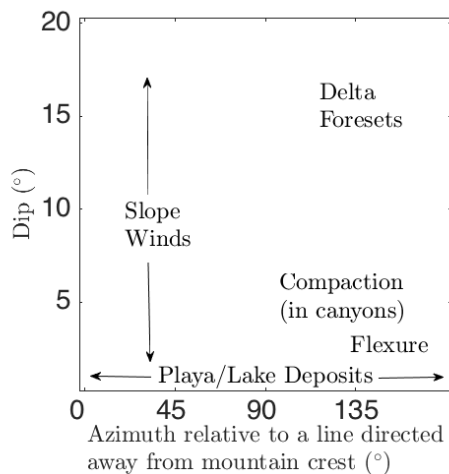
Observations:
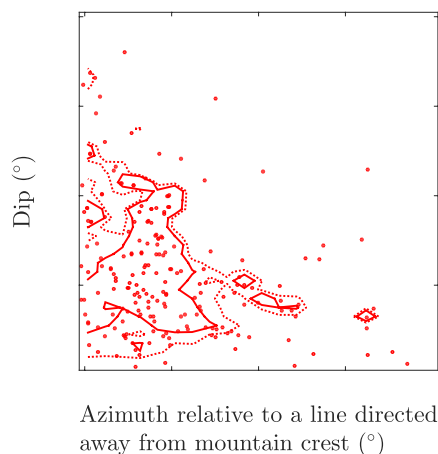
Fig. 1. Summary of results, for measurements above the interpolated basal surface of the mountains. Dots are individual measurements with ≤2° pole error. Inner and outer contours enclose 50% and 68% of measurements.

Background: Malin and Edgett [1] divided Mars sedimentary rocks into three classes of unit. The youngest, dark-toned "thin mesa" units, and unconformably drape all other rocks. The surfaces defined by interpolating "thin mesa" outliers are similar to modern mound topography. Therefore, sedimentary-rock deposition continued after mound shapes were defined. [2] used a basic physical model of wind erosion to interpret the outward tilts of layers at Mt. Sharp. They proposed that Mt. Sharp grew by draping, with erosion by slope-winds defining a moat around the growing mound (a syndepositional moat). Alternatively, [3] and [4] propose the mountains contain lacustrine/playa sediments, in which case layer tilts must correspond to postdepositional tilting mechanisms such as compaction or flexure. Using layer-tilt data obtained from HiRISE DTMs, we set out to test the contrasting predictions of these mountain-formation models.

Methods: Bedding plane traces were carried out by visual inspection using 1m-pixel orthorectified digital elevation models and paired HiRISE images in Ceti Mensa, Nia Mensa, Juventae Mensa, Coprates Mensa, and Melas Mensa, plus Mt. Sharp, according to the methods used in Ref. [11]. Our DEM production process used the Ames Stereo Pipeline; comparison of our DEMs to PDS-released DEMs showed ≤0.2° relative tilt. Strike and dip were calculated for the r^2 best fit planar interpolation of each bed trace. Error was calculated using the methed of [11], with samples rejected if pole error was >2°. In addition to the stereo DEMs, digital models of each sedimentary mound were built from existing MOLA data at ~400m per pixel. Mound boundaries, and the crest lines of elongate mounds, were drawn by visual inspection of THEMIS mosaics. A mound basal surface was defined using cubic polynomial interpolation within mound edges. Elevation above mountain base is calculated as the difference between measured elevation and the basal surface.

**How we know that our measurements are not biased downslope:** Errors in tracing a layer on a slope on an orthorectified image will produce a downslope bias in plane-fits to the trace using the corresponding DEM. A decisive test for this bias is to compare our measurements using a DEM derived from a HiRISE stereopair to those made on a simultaneously-acquired CTX stereopair. If downslope bias affects the HiRISE layer orientations, then the same layers traced on CTX will suffer a bias that is proportionally more severe. For the region covered by the ESP_013540_1745/ESP_012907_1745 stereopair (where layers typically dip at right angles to the local downslope), we found that CTX measurements are similar to HiRISE measurements (Fig. 2). We did not find

a large systematic bias downslope in the CTX traces relative to the HiRISE traces. This shows that the downslope bias of HiRISE layer-orientation data is small.

If the layers are initially horizontal, and dips are produced by downslope slumping in a near-surface mobile layer, then we would see larger dips for traces with a smaller range of absolute elevations. We found the opposite trend, excluding this potential source of error.

We also found consistency between measurements by workers using the same procedure, both within our lab and between labs. For example, at Gale, outward dips have been independently confirmed by [2,4,5,6].
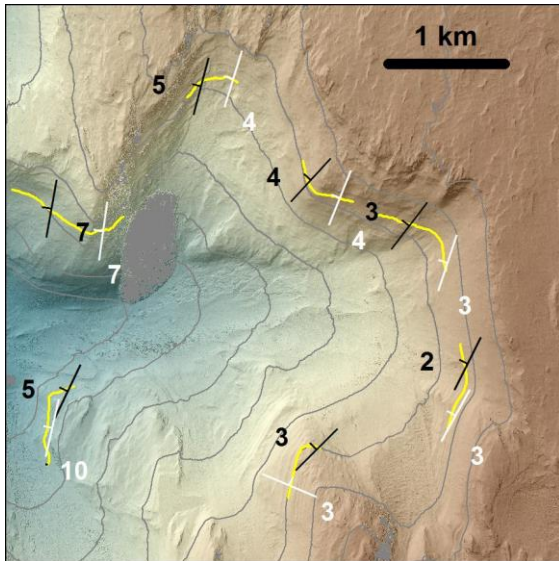
Fig. 2. Examples of layers (yellow), showing similar dips whether traced on CTX DTMs (white) or HiRISE DTMs (black). Contour interval 100m, red is high, backdrop is HIRISE DTM shaded relief.

Results: Bedding planes usually dip away from mound centerlines (Fig. 1). For layers above the mountain base, the dip azimuth of measured beds falls within 90° of the vector directly away from the nearest mound crest in 90% of measured beds, and within 45° in 64%. Bedding plane angles ranged from ~0-18 ° from the horizontal, with a tendency towards steeper angles as elevation increases. Systematic outward dips have also been reported for Hebes Mensa [7] and Ganges Mensa [8].

Independent evidence from landslides and unconformities: R.P. Sharp noted [9] that gravity-slide deposits, when stratigraphically encapsulated, reflect the location of paleo-highs on unconformity surfaces. Landslides in Ceti Mensa [10], around Juventae Mensa, at Mt. Sharp, and possibly at Melas Mensa, are directed away from the mountain crest and stratigraphically overlain by sedimentary rocks. This shows that sedimentary-rock deposition continued after the moats were defined.

Fitting quadratic surfaces to previously-mapped [7,13-16] large unconformities at W Candor, Ophir and Gale shows that most of the unconformity surfaces, regardless of who mapped them, are domes. Best-fit paleo-highs are located close to modern topographic highs. This is a third independent line of evidence for syndepositional moats.

Implications: Because Valles Marineris graben have flat, noncompactible floors (away from sediment mounds), sediment compaction would produce flat or inward dips. However, we see outward dips in the Valles Marineris mountains, ruling out differential compaction as the cause of the tilts. The data are consistent with mound formation by draping interspersed with moat-deepening (i.e., a syndepositional moat).

Our data span a range of elevations, from the base of the mountains up to the summits. At the conference, we will discuss the relationship between layer orientations and stratigraphic elevation. Fig. 3 shows that the trend for layers to dip away from the mountain crest is more pronounced at higher elevations above ther interpolated basal surface, although it remains significant even for beds at <0.5 km. We will also discuss the relationship between layer orientations and presence/absence of aqueous-mineral detections.
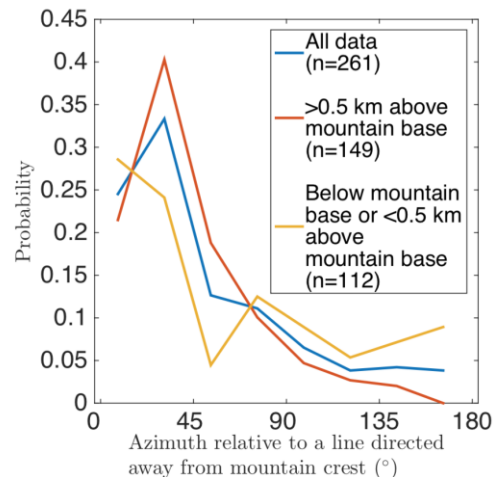
Fig. 3. Distribution of layer orientations relative to elevation above mountain base. Includes 61 data from [2].

References: [1] Malin & Edgett (2000) *Science* [2] Kite et al. (2013) *Geology*, 41(5), 543-546. [3] Murchie et al. (2009) *J. Geophys. Res.* 114 E00D05. [4] Andrews-Hanna (2012) *J. Geophys. Res.* 117, E06002. [5] Lewis & Aharonson (2014) *J. Geophys. Res.* 119, 1432-1457. [6] Fraeman et al. (2013) *Geology*, 41(10), 1103-1106. [7] Le Deit et al. (2013) *J. Geophys. Res.* 118, 2439-2473. [8] Stack et al. (2013*) J. Geophys. Res.* 118(6), 1323-1349. [9] Timmins et al. (2014) *45th LPSC.* [10] Hore (2014), MSc Thesis, Brock University. [11] Sharp (1940), *Am. J. Sci.* vol. 238. [12] C. Okubo (2014), USGS Scientific Investigations Map 3309. [13] Anderson & Bell (2010) *Mars Journal* 4, 76-128. [14] Thomson et al. (2011) *Icarus* 214, 413-432. [15] Lucchita (2015) *46th LPSC.* [16] Wendt (2011) *Icarus* 213, 86-103.

IMPACT INDUCED HEATING OF OCCATOR CRATER ON ASTEROID 1 CERES. T. J. Bowling[1], F. J. Ciesla[1], S. Marchi[2], B. C. Johnson[3], T. M. Davison[4], J. C. Castillo-Rogez[5], M. C. De Sanctis[6], C. A. Raymond[5], and C. T. Russell[7]. [1]University of Chicago, Chicago, IL (tbowling@uchicago.edu), [2]Southwest Research Institute, Boulder, CO, [3]Brown University, Providence, RI, [4]Imperial College, London, UK, [5]Jet Propulsion Laboratory, Caltech, Pasadena, CA, [6]National Institute of Astrophysics, Rome, IT, [7]University of California, Los Angeles, CA.

Introduction: Dwarf planet Ceres, the current target of NASA's Dawn mission and the inner solar system's last remaining 'wet protoplanet', is thought to be composed of a mixture of silicates and ices [1]. One of Ceres' most intriguing features revealed by the Dawn spacecraft is the 92-km diameter crater Occator [2]. This crater is expected to be 10s-100s Myr old and contains some of the highest albedo features on the asteroid, which are possibly salt deposits [2]. Occator's longitude is also compatible with the putative source region for previously detected H_2O outgassing from Ceres [3], and may contain a diurnally periodic dust haze [2] driven by near surface volatile sublimation. To better understand the nature and possibility of post-impact hydrothermal systems in Occator, which may determine the distribution of salts and water ice in the crater's near surface, we use a suite of numerical models to investigate the initial temperature structure and subsequent cooling of the crater.

Methods: We model the formation of Occator using the iSALE-2D shock physics code [4-6] in order to obtain an initial temperature structure for the crater. Ceres is represented as a half space composed of a 50%/50% intimate mixture of hydrated silicate [7] and H_2O ice [8]. Material thermodynamics are modeled using the ANEOS equation of state package, and material mixing assumes an intimate combination of species in thermal and physical equilibrium following [9]. Because the simple-complex crater transition on Ceres is consistent with an icy target [10], we employ an ice rheology [11] modified to include ice-like visco-elastic-plastic behavior [12,13]. The pre-impact thermal structure of the target is taken from [14] with a surface temperature of 200K. Spherical impactors, composed of dunite [15] and with diameters of 3.7 and 5 km, collide with this target at Ceres' mean (4.8 km s^{-1}) and above average (7.5 km·s^{-1}) impact velocities.

Results: Both simulations result in the formation of an ~80-km diameter central peak crater with maximum depth of ~5 km. The initial central peak is tall enough to be gravitationally unstable, and subsequent collapse concentrates hot material into a subsurface locus at the base of the peak [Fig. 1]. This locus, with a maximum temperature of 305 K (4.8 km·s^{-1}) and 340 K (7.5 km·s^{-1}) is the only region of the target to meet temperature and pressure thresholds required to melt

H_2O ice, although the inclusion of impurities may lower the melting temperature considerably [16]. In both simulations, the central peak is composed of material uplifted from considerable (15-30 km) pre-impact depth. Because of its provenance, this material may have been sheltered from heating and subsequent devolatilization from both previous impacts as well as the Occator forming impact, and subsequently may be more volatile rich than average for the crater. During the subsequent thermal evolution of the crater this unaltered, volatile rich material may be heated above the melting point of water by the conductive thermal pulse from the hot locus at the base of the central peak. Assuming a typical thermal diffusivity of 10^{-6} m^2·s^{-1} and a characteristic length scale of 10 km, temperatures within the hot locus and central peak should decay below the melting point of water on a timescale of ~3 Myr, much shorter than the suspected age of the crater even when neglecting advective heat transfer within hydrothermal systems. Details of Occator's post-impact thermal evolution will be investigated numerically following [17] with thermal boundary conditions taken from [14, 18].

Discussion: Today, Occator does not have a central peak, but is instead fairly flat with a central pit [2]. The most commonly accepted explanation for the formation of central pit craters in icy targets relies on the formation of an impact-induced melt pond which subsequently drains into fissures in the crater floor [19]. Because our target is composed of an intimate mixture of ice and rock, as opposed to pure ice, the collapse process is likely slightly different: 1) the crater forms with a central peak of heated ice-rock mixture, some of which may exceed the melting point of H_2O. 2) subsequent outgassing of water [20], possible loss of water through liquid water eruptions, and drainage into the subsurface removes volume from the central peak. 3) as ice is lost the central peak begins to slump, which, along with visco-elastic relaxation of the crater [21] results in a relatively flat floor and central pit. It should be noted that the initial prominence of the central peak may be lower than seen in our simulations, as the acoustic fluidization [22] parameters for ice were derived for icy satellites at much higher impact velocities [23], so further simulations exploring this parameter space will be run.

The subsurface locus of >273K material seen in Fig. 1 represents the only region in which hydrothermal circulation may occur. Melted subsurface material may percolate or effuse onto the floor of the crater, where it will subsequently sublime and build a lag deposit (possibly involving dissolved salts). Such outflows may be the origin of the 'bright spots' observed within Occator. Bright spots observed elsewhere on Ceres [2] may be recently exposed material originating from a similar process in subsequently erased craters.

The possible detection of a diurnal dust haze within Occator by the Dawn spacecraft implies that subsurface H_2O is currently subliming within the crater and subsequently being lost from the body. Because the thermal skin depth of the diurnal wave should be extremely shallow (<0.1 m), the periodic nature of this haze implies a driving H_2O source in the very near surface. Assuming a daytime H_2O loss rate of 1 kg·s^{-1} [3], a 10 km diameter source region (comparable to the size of Occator's central pit) should become depleted of volatiles in ~2000 yr. A 100 m diameter source region (comparable to the highest resolution obtained by Dawn instruments [24]) should become depleted in ~0.2 yr, shorter than the temporal baseline over which water production has been observed on Ceres [3,25]. As such, the source region must be either very young or continually recharged via hydrothermal circulation. Because the current temperatures beneath Occator should have decayed well below the melting point of water, we consider the possibility of active hydrothermal recharge extremely unlikely. High resolution imagery currently being obtained by the Dawn spacecraft will determine if there is a sufficiently young source within Occator (such as a small, recent crater which has exposed fresh volatile rich material) to explain the presence of the putative haze.

References: [1] McCord, T. B. and Sotin, C. (2005) *JGR*, *110*, E05009. [2] Nathues, A. et al. (2015) *Nature, 528,* 237-240. [3] Küppers, M et al. (2014) *Nature*, *505*, 525-527. [4] Amsden, A. et al. (1980) *LANL Report*, LA-8095. [5] Collins, G. S. et al. (2004) *MAPS*, *39*, 217. [6] Wünnemann, K. et al. (2006) *Icarus*, *180*, 514. [7] Brookshaw, L. (1998) *Working Paper Series SC-MC-9813*, 12pp. [8] Turtle, E. P. and Pierazzo, E. (2001) *Science*, *294*, 1326-1328. [9] Pierazzo, E. et al. (2005) *GSA Special Papers*, *384*, 443-457. [10] Schenk, P. (2015) *AGU Fall Meeting*, P23E-2186. [11] Senft, L. E. and Stewart, S. T. (2008) *MAPS*, *43*, 12. [12] Elbeshausen, D., *personal communication*. [13] Durham, W. B. et al. (1992) *JGR*, 97, E12. [14] McCord, T. B. and Sotin, S. (2005) *JGR*, 110, E05009. [15] Benz, W. et al. (1989) *Icarus*, *81*, 113-131. [16] Stillman, D. E. et al. (2016) *Icarus*, *265*, 125-138. [17] Davison, T. M. et al. (2012) *Geochimica et Chosmochimica Acta*, *95*, 525-26. [18] Hayne, P. O. and Aharonson, O. (2015) *JGR Planets*, *120*, 1567-1584. [19] Elder, C. et al. (2012) *Icarus*, *221*, 831-843. [20] Fanale, F. P. and Salvail, J. R. (1989) *Icarus*, *82*, 97. [21] Bland, M. T. (2013) *Icarus*, *226*, 510-521. [22] Melosh, H. J. (1979) *JGR*, *84*, B13. [23] Bray, V. J. et al. (2014) *Icarus*, *231*, 394-406. [24] Rayman, M. et al. (2006) *Acta Astronautica*, *58*, 605. [25] A'Hearn, M. F. and Feldman, P. D. (1992) *Icarus*, *98*, 54-60.
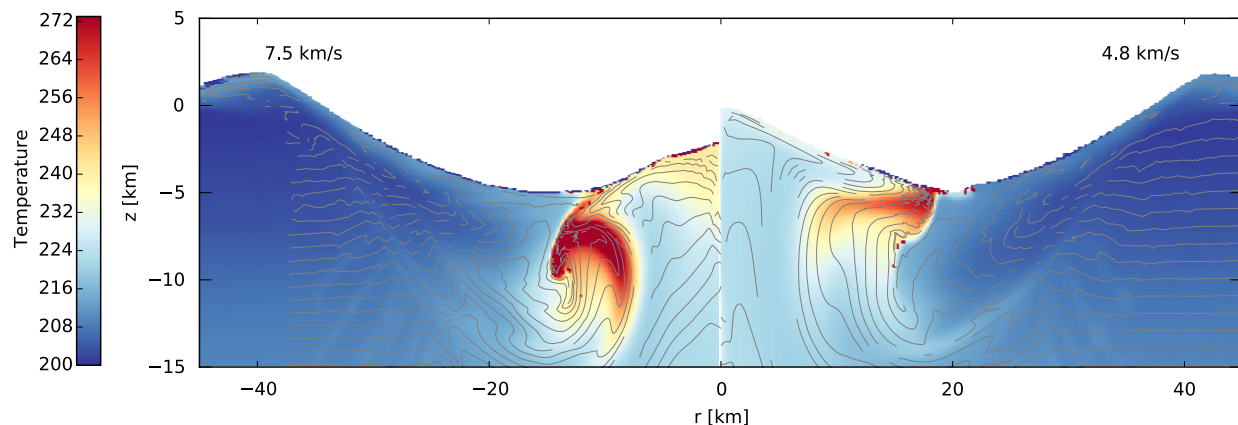
Figure 1: Thermal structure of an Occator-like crater 1500 s after impact for impact velocities of 4.8 and 7.5 km·s^{-1}.

^{36}Cl-^{36}S SYSTEMATICS IN *CURIOUS MARIE*: A ^{26}Mg-RICH U-DEPLETED FINE-GRAINED CAI FROM ALLENDE. H. Tang[1], M-C. Liu[1], K.D. McKeegan[1], F.L.H. Tissot[2,3] and N. Dauphas[2], [1]Ion Probe Group, Department of Earth, Planetary, and Space Sciences, UCLA; [2] Origins Lab, Department of the Geophysical Sciences and Enrico Fermi Institute, the University of Chicago; [3]Department of the Earth, Atmospheric and Planetary Sciences, MIT, Cambridge. (haolantang@ucla.edu).

Introduction: Chlorine-36 ($t_{1/2}$=0.3 Myr) decays to either ^{36}Ar (98%, β^-) or ^{36}S (1.9%, ε and β^+). This radionuclide can be produced either by local irradiation of gas and/or dust of solar composition [1-2] or by stellar nucleosynthesis in AGB stars or Type II supernovae [3]. Evidence for the presence of ^{36}Cl in the early Solar System (ESS) comes from radiogenic excesses of ^{36}Ar [4] and/or ^{36}S [5-9] in secondary phases (*e.g.*, sodalite and wadalite) in ESS materials such as Calcium, Aluminum-rich inclusions (CAIs) and chondrules. Though the presence of ^{36}Cl in the ESS has been demonstrated, the inferred initial ^{36}Cl/^{35}Cl ratios vary a lot (from 1.0×10^{-7} to 2×10^{-5}) from one inclusion to another [5-9]. Interestingly, all secondary phases measured so far lack resolvable ^{26}Mg excesses that could be due to the decay of ^{26}Al ($t_{1/2}$ = 0.7 Myr), implying that ^{36}Cl and ^{26}Al may not have been derived from the same source. Given that ^{26}Al could have come from a stellar source [10] and that secondary phases should have formed late, we are left with either a very high ^{36}Cl/^{35}Cl initial ratio ($\sim 10^{-2}$) in the ESS, or a late (> 3 Myr after CAI formation) irradiation scenario for the production of ^{36}Cl [9]. ^{36}Cl/^{35}Cl $\sim$ 10^{-2} far exceeds the predictions from any model (stellar nucleosynthesis or irradiation); therefore, a late irradiation scenario producing ^{36}Cl at the observed level is favored. In this framework, ^{36}Cl is produced in the early solar nebula and incorporated into CAIs via aqueous activities, which could also lead to the formation of sodalite.

The Allende *Curious Marie* fine-grained (non-FUN) CAI is a special sample. It is characterized by an extremely large ^{235}U excess (δ^{235}U $\sim$59 ‰ rel. to CRM-112a) [11], providing strong evidence that ^{247}Cm was alive in the ESS, as previously suggested by [12]. This CAI lacks primary refractory phases, but instead contains a wide distribution of chlorine-rich phases (sodalite and nepheline), which are characterized by large, yet uniform, ^{26}Mg excesses (δ^{26}Mg*) of $\sim$43‰ over a large range of ^{27}Al/^{24}Mg values [Fig 1A; 13]. This observation contrasts largely with previous findings and implies that ^{26}Al could have still been alive when sodalite formed, and the homogeneous δ^{26}Mg* found in all spots measured could have resulted from later closed-system resetting [13]. Therefore, this CAI offers an excellent opportunity to investigate the relationship between ^{26}Al and ^{36}Cl, as well as the evolution of this strange CAI. We performed isotopic analysis for the ^{36}Cl-^{36}S systematics, and the preliminary results are reported here.

Method: Secondary minerals such as nepheline, sodalite, Fe-rich pyroxene, and Fe-rich spinel were observed in *Curious Marie*. Analyses for the Cl-S system were performed on the new Cameca ims-1290 ion probe in UCLA. Sulfur isotopes (^{33}S, ^{34}S, and ^{36}S) as well as chlorine isotopes (^{35}Cl and ^{37}Cl) in sodalite were measured in a peak jumping mono-collection mode, with the mass sequence of 32.8, ^{33}S, ^{34}S, ^{35}Cl, ^{36}S and ^{37}Cl. Negative secondary ions were produced by a 0.6 nA Cs$^+$ primary ion beam focused to a <10 μm spot. A long pre-sputtering time was required (>20 mins) to minimize the surface S contamination. A mass resolving power of 5000 was used to resolve interferences from the peaks of interest. Besides, of special importance in the measurement of ^{36}S is the potential contribution from the scattered ions of ^{12}C$_3$ and ^{35}ClH, but this did not appear to be a problem under our analytical condition. The instrumental mass fractionation (IMF) was internally corrected by using standards of Balmat pyrite, Canyon Diablo troilite, CAR 123 pyrite, and NIST 610 glass. The transmission was decreased to avoid QSA effect (Quasi-Simultaneous Arrival) in pyrite and troilite standards and data were reduced from total counts. The excesses of ^{36}S were calculated by following a linear law with a mass fractionation exponent of -0.489 obtained from standards. In addition, a terrestrial sodalite (^{35}Cl/^{34}S = 15,000) was applied to verifying the validity of mass spectrometry. The relative sensitivity factor of ^{35}Cl/^{34}S ($\sim$0.93) used throughout this study was determined from NIST 610 glass (Cl/S=1).

Results and discussion: Significant excesses in ^{36}S are clearly resolved in *Curious Marie* over a large range of ^{35}Cl/^{34}S values (from 500 to 20,000). However, the ^{36}S excesses are uniformly elevated, with a weighted average of 95±28‰ (2σ error, reduced χ^2 = 3), independent of the Cl/S ratio. Therefore, no isochron is observed and no initial ^{36}Cl/^{35}Cl ratio can be inferred for this CAI.

In our previous study we proposed that the presence of homogeneous δ^{26}Mg* to be 43±6‰ (2σ error, reduced χ^2 = 3) and negative δ^{25}Mg (from $\sim$-9‰ to -19‰) in *Curious Marie* indicates that Mg isotope exchange must have taken place in a closed system to avoid dilution with chondritic Mg [13]. Although the uniform ^{26}Mg excess independent of Al/Mg precludes the determination of an isochron, a model ^{26}Al/^{27}Al ratio = $(6.2\pm0.9) \times 10^{-5}$ can still be inferred by using the bulk ^{27}Al/^{24}Mg ratio ($\sim$95, measured by solution ICPMS; [11]) and assuming δ^{26}Mg$_0$ = 0. This suggests

that either the secondary phases in the *Curious Marie* CAI formed while [26]Al was still at the canonical level, or the CAI remained intact until a late-alteration event, which took place after [26]Al had completely decayed away, homogenized the [26]Mg excesses and formed sodalite. The latter scenario would be less likely as the elevated uniform δ^{26}Mg* requires closed-system homogenization, contrary to the fact that the formation of sodalite requires an external Cl-rich fluid. Besides, the significant Mg loss resulted from this alteration can achieve a higher bulk [27]Al/[24]Mg ratio in this CAI relative to the normal range (~2-10) with the δ^{26}Mg* value similar to or lower than that in the primary mineral (<5‰). Therefore, we propose that alteration resulting in the formation of sodalite in *Curious Marie* must have taken place extremely early, probably right after the condensation of this CAI, so that the Cl-rich fluid involved in this process can wash Mg (and perhaps U) away without diluting δ^{26}Mg*.
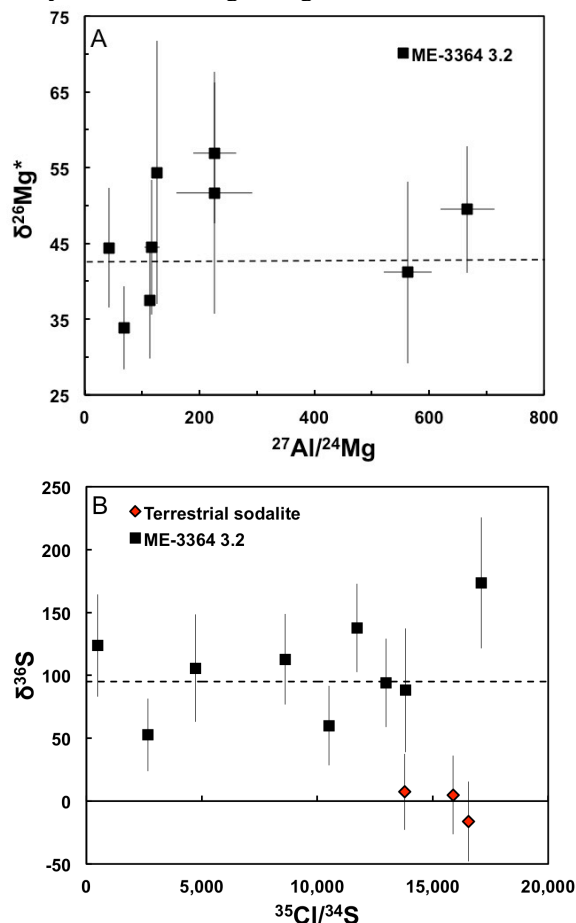

The Cl-S result can also be understood in the context of the aforementioned alteration scenario. Although it is impossible to form an isochron, and thus an initial [36]Cl/[35]Cl ratio, based on the CAI's Cl-S isotopic results, the [36]S excesses in the sodalite would still require the presence of [36]Cl. This radionuclide can be introduced into the CAI via a Cl-rich fluid involved in the formation of secondary phases or be produced by late local irradiation on the sodalite. The former interpretation implies that [36]Cl was present in the early solar nebula at the time of CAI condensation, which would require that [36]Cl originated from a stellar source or early local irradiation. In the context of the latter explanation, [36]Cl would be produced in-situ inside sodalite by late irradiation, similar to the proposed scenarios in [5-9]. However, knowledge about the Cl and S elemental abundances is required to estimate the [36]Cl/[35]Cl production ratio for *Curious Marie*. The final event would be that both δ^{26}Mg and δ^{36}S were homogenized in the entire CAI in a closed system after the complete extinction of [26]Al and [36]Cl.

Conclusion: We find elevated and uniform excesses in [36]S, similar to those for [26]Mg excesses, in the U-depleted fine-grained CAI *Curious Marie*, implying a complicated multi-stage history. The CAI precursor condensed with the [26]Al/[27]Al canonical ratio and might have experienced an extremely early alteration process with a Cl-rich, Mg-free fluid to form the secondary phases including sodalites and nephelines. The presence of [36]S excesses can be interpreted as a decay product of [36]Cl, which was either introduced from a Cl-rich fluid in early alteration or produced through in situ local irradiation on the CAI after sodalite formed. Further studies of the Al-Mg and Cl-S systematics in other fine-grained CAIs are ongoing to investigate their condensation in the early solar nebula and alteration in the chondritic parent bodies as well as the origin of [36]Cl in different early-formed objects.

References: [1] Leya et al., (2003) *APJ* **594,** 605. [2] Gounelle et al., (2006) *APJ* **640,** 1163. [3] Wasserburg et al., (2006) *Nucl. Phys. A,* **777,** 5. [4] Murty et al., (1997) *APJ* **475,** L65. [5] Lin et al., (2005) *PNAS* **102,** 1306. [6] Hsu et al., (2006) *APJ* **640,** 525. [7] Ushikubo et al., (2007) *MAPS* **42,** 1267-1279. [8] Nakashima et al., (2008) *GCA* **72,** 6141-6153. [9] Jacobsen et al., (2011) *APJ* **731,** L28. [10] Villeneuve et al., (2009) *Science* **325,** 985. [11] Tissot F. L. H. et al. (2016) *Science Advances* In press. [12] Brennecka et al., (2010) *Science,* **327,** 449-451. [13] Tang, et al., 2015. *78th MetSoc.* #5263.

Fig. 1. (A) [26]Al-[26]Mg and (B) [36]Cl-[36]S systematics in Allende CAI *Curious Marie* (2σ error). The black dash line in A indicates the average δ^{26}Mg of ~43‰ in *Curious Marie*. The black dash line in (B) represents the average δ^{36}S of ~95‰.

LATE-STAGE WEATHERING AND CHLORAPATITE DISSOLUTION AS A POSSIBLE SOURCE FOR CHLORIDES ON THE MARTIAN SURFACE.

M. Melwani Daswani[1] and E. S. Kite[1], Department of the Geophysical Sciences, University of Chicago (5734 S Ellis Ave., Chicago, IL 60637, melwani@uchicago.edu).

Introduction: Chlorides could potentially preserve biosignatures, and their presence in sediments indicates past aqueous activity. Local chloride-bearing deposits are widely distributed in the southern highlands on Mars [1]. Their formation is inferred from spectroscopy, topography and geological context to result from ponding surface fluids, and salt concentration by evaporation [e.g., 2]. Assuming the chlorides are NaCl, volumetric calculations of a chloride-bearing deposit and its paleolake near Miyamoto crater in Meridiani Planum were used to estimate a lake salinity of ~ 4 g/kg H_2O [2]. The source of chlorine for the deposits is unknown, but could be: 1) the martian soil, containing ~ 0.5 wt. % Cl [3] (possibly as perchlorates), 2) subsurface dissolution of previously deposited chlorides, or 3) from Cl-bearing igneous minerals leached by fluids.

Here we use mass balance calculations and one-dimensional (1D) reaction-transport fluid-rock geochemical modeling to constrain the mass of water and reactant rock required to produce the Meridiani Planum chloride deposit near Miyamoto crater studied by [2]. We also compute the composition of the dissolved reactant rock, secondary mineral precipitates and fluid composition along the reaction path. Fig. 1 represents the geological setting.
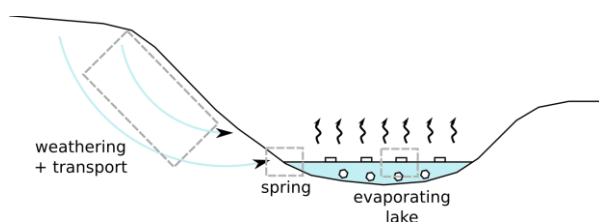
Figure 1 Schematic profile of the geological context of the possible chloride-bearing lake. We hypothesize that fluids permeate and alter the crust, producing secondary minerals (Figure 2), and spring at the lake bearing ions (Figure 3). The lake evaporates, precipitating evaporites.

Methods: Geochemical fluid-rock reaction modeling was carried out with CHIM-XPT, using modified Debye-Hückel theory to calculate mass balance, mineral, gas and liquid compositions at varying P-T conditions [4]. The composition of the basaltic clasts in Amazonian martian breccia meteorite Northwest Africa (NWA) 7034 was used as the host reactant rock in the 1D reaction model because of its similarity to martian

surface compositions [e.g., 5, 6]. Temperature was kept at 273 K, pCO_2 was 60 mbar (higher than the current atmosphere [e.g., 7], but lower than estimates for the Noachian [e.g., 8]), and total pressure was 1 bar.
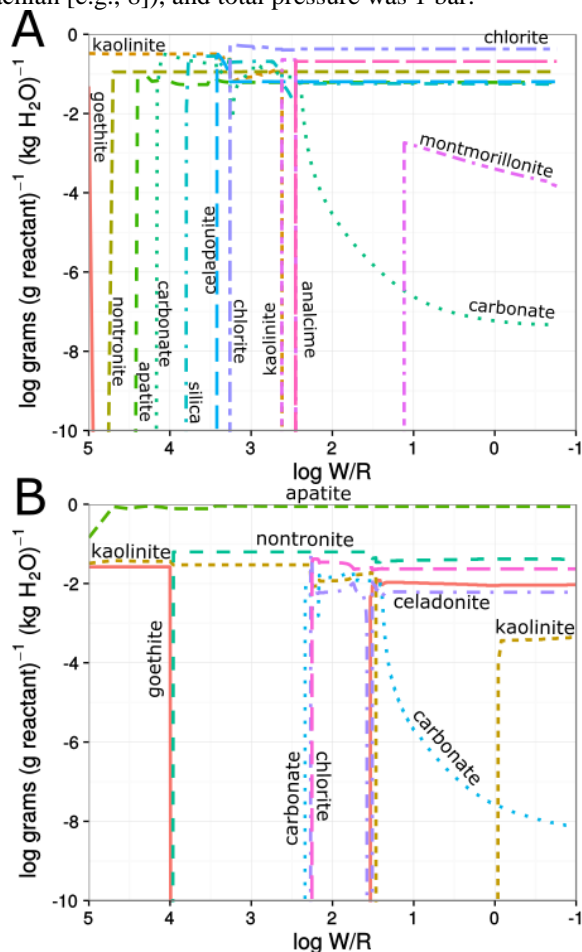

Figure 2 Secondary minerals precipitated along the weathering path leading to the lake (read from left to right, as fluid infiltrates further). A) Congruent weathering of NWA 7034 basalt clasts, and b) weathering 90 wt. % (F-Cl-OH) apatite + 10 wt. % NWA 7034 basalt clasts.

Chlorapatite as a reactant. Apatite in NWA 7034 (~ 6 wt. % of the basaltic clasts) is Cl-rich [e.g., 5], and its abundance in the reactant rock has an impact on the resulting fluid and secondary mineral composition. Apatite also dissolves more quickly than silicates like olivine and pyroxene [e.g., 9] and so the incongruent dissolution of the rock was approached by forward reaction-transport models with different initial apatite

contents, from 1 to 90 wt. % apatite, amounting to 0.05 – 4.1 wt. % Cl in the reactant (here we show 6 and 90 wt. % apatite for simplicity).

Results: Dissolution of NWA 7034 leads to different secondary mineral precipitates depending on the water to rock ratio (W/R) and the relative masses of minerals dissolved (i.e., congruent vs. incongruent dissolution, Fig. 2).
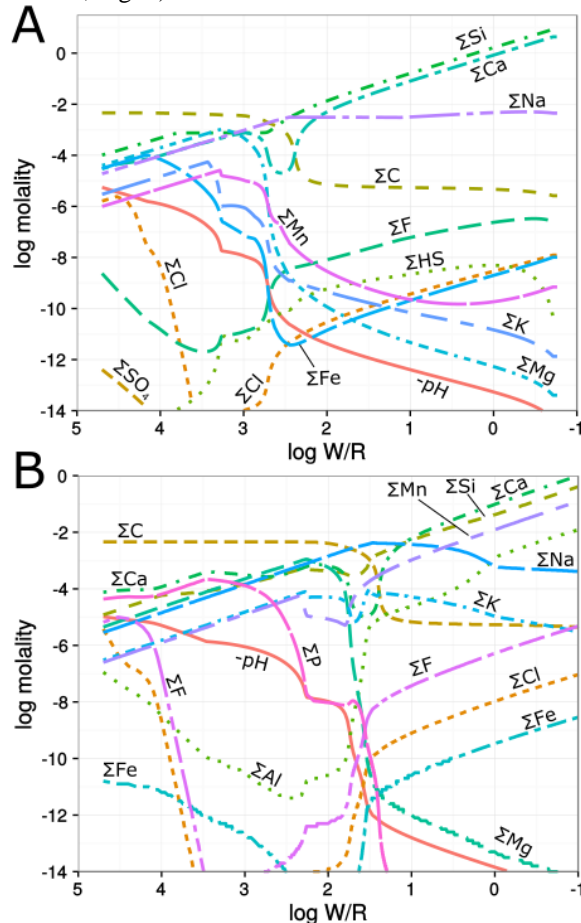
Figure 3 Composition of the water at the spring (sums of aqueous species, note the negative sign for pH), after weathering NWA 7034 basalt clasts a) congruently, and b) with 90 wt. % apatite.

Si-bearing phases dominate the secondary assemblage when NWA 7034 basalt clasts are altered congruently (Fig. 2a), including chlorite and smectites which have been detected on Mars from orbit [e.g., 10]. F-Cl-OH apatite is the most abundant precipitate when accounting for the higher dissolution rate of apatite (Fig. 2b). In both scenarios, pH, Si, Ca and Na increase in the solution as the host rocks dissolve (Fig. 3). Notably, incongruent reaction (with higher amounts of apatite) leads to more oxidized solutions than congruent reaction with the NWA 7034 basalt clasts (Fig.

3). Surprisingly, at $1000 > W/R > 100$, Cl in solution is higher under congruent dissolution than incongruent dissolution (Fig. 3). This is because Cl-bearing apatite is a stable secondary mineral which removes Cl from the solution when phosphate is available (Fig. 2b and 3b).

Discussion: At W/R = 10, congruent dissolution releases 1.3×10^{-11} kg Cl/kg H_2O into solution, while 90 wt. % apatite in the reactant releases 2.8×10^{-11} kg Cl/kg H_2O. To produce the chloride deposit at Meridiani (a ~ 0.12 km^3 deposit in a ~ 35 km-wide basin[2]), ~ 2.5×10^5 kg rock/m^2 (~ 15 m depth) were leached if dissolution was congruent, or ~ 1.7×10^3 kg rock/m^2 if the fluid composition was derived mostly from the apatite dissolution. (Assuming the chlorides are NaCl with 45 % porosity, and a reactant rock density of 1650 kg/m^3.) The required depth of leaching is greater than the annual thermal skin depth, and improbably high volumes of water are needed to leach the Cl in both cases ($10^{10} - 10^{11}$ km^3).

Others [2] noted the relationship between chloride deposits in paleolakes and chloride deposits in their feeding valleys, suggesting that the deposits in paleolakes were mobilized from upstream. On Earth, chlorides commonly originate from seawater or are dissolved and re-precipitated from marine deposits [11]. We have shown that preferential dissolution of apatite at low W/R in a single wetting event cannot reasonably account for the inventory of chlorides observed at the deposit studied. Alternatively, multiple dissolution events and kinetic inhibition of apatite re-precipitation may satisfy mass balance. We will carry out further work to constrain the required amounts of rock and water to form other observed chloride deposits, and the fluid and rock composition. We will also compare our results to water volumes independently estimated from geomorphology.

References: [1] Osterloo M. M. et al. (2010) *J. Geophys. Res. 115*, E10012. [2] Hynek B. M. et al. (2015) *Geology 43*, 787 – 790. [3] Keller J. M. (2007) *J. Geophys. Res.: Planets 111*, E3. [4] Reed M. H. (1998) *Rev. Econ. Geol.10*, 109 – 124. [5] Santos A. R. et al. (2015) *Geochim. Cosmochim. Acta 157*, 56 – 85. [6] Beck P. et al. (2015) *Earth Planet. Sci. Lett. 427*, 104 – 111. [7] Mahaffy P. R. et al. (2013) *Science 341*, 263 – 266. [8] Kite E. S. et al. (2014) *Nat. Geosci. 7*, 335 – 339. [9] Hurowitz J. A. and McLennan S. M. (2007) *Earth. Planet. Sci. Lett. 260*, 432 – 443. [10] Ehlmann B. L. and Edwards C. S. (2014) *Annu. Rev. Earth. Planet. Sci. 42*, 291 – 315. [11] Warren J. K. (2010) *Earth-Sci. Rev. 98*, 217 – 268.

Further Evidence of Beryllium-10 Heterogeneity in the Early Solar System Inferred from Be-B Systematics of Refractory Inclusions in a Minimally Altered CR2 Chondrite.

E. Dunham[1], M. Wadhwa[1], R. Hervig[1], S. Simon[2], L. Grossman[2] [1]School of Earth and Space Exploration, Arizona State University, Tempe AZ, 85287 (email: etdunham@asu.edu), [2]Dept. of the Geophysical Sciences, The Univ. of Chicago, Chicago IL, 60637.

Introduction: Determining the initial abundances and distributions of short-lived radionuclides in the solar protoplanetary disk is key to understanding the astrophysical birth environment of our Solar System ([1], and references therein). Beryllium-10, which decays to ^{10}B with a half-life of 1.4 Ma, is of particular interest since it is produced almost exclusively by irradiation reactions. Previous studies have demonstrated that this short-lived radionuclide was present in the early Solar System with an initial $^{10}Be/^9Be$ ratio in the range of ~10^{-4}-10^{-2} [2-8]. Although this wide range may in part be due to significant analytical uncertainties, the initial $^{10}Be/^9Be$ ratio inferred from these analyses is substantially higher than the value expected from the galactic background, ~10^{-5} [2].

There are two possible astrophysical settings in which the enhanced abundance of ^{10}Be in the early Solar System may have originated. One possible setting is the dense protosolar molecular cloud core where ^{10}Be may have been enhanced by trapping of galactic cosmic rays [9] or by spallogenesis during energetic particle irradiation [2]. An alternative setting is within the solar nebula, where irradiation of gas and/or refractory solids during an early active phase of the Sun may have produced ^{10}Be [2, 10, 11].

In this context, the prediction is that if the ^{10}Be enhancement occurred prior to Solar System formation, then processes involved in molecular cloud collapse and formation of the solar nebula would likely have resulted in a homogeneous ^{10}Be distribution. In contrast, local irradiation within the nebula could have produced significant temporal and spatial variations in ^{10}Be abundances in the early Solar System. The wide range in the initial $^{10}Be/^9Be$ ratio inferred from previous studies [2-8] is more consistent with the latter. However, with few exceptions (e.g., [6, 8]), the Be-B systematics reported thus far have been from refractory inclusions in CV3 chondrites [2-5, 7] that have experienced exposure to thermal and shock processes [12, 13]. Therefore, it is possible that some of the observed variation in the initial $^{10}Be/^9Be$ ratio could be due to disturbance by these processes. The CR2 chondrites are thought to be among the least altered based on petrological, geochemical and isotopic characteristics (e.g., [14]). In this study, we report for the first time the Be-B systematics in two calcium-aluminum-rich inclusions (CAIs) from a CR2 chondrite, Northwest Africa (NWA 5028). We additionally report the Be-B systematics of a CAI from the CV3 chondrite Allende, which allows us to compare our results with those of previous studies on CAIs from this same meteorite.

Analytical Methods: Sample characterization, including mapping of mineral phases and determination of mineral chemistries, was performed using electron microprobe techniques. The Allende CAI was analyzed with the Cameca SX-50 instrument at the University of Chicago [15], while the NWA 5028 CAIs were analyzed with the Cameca SX100 at the University of Arizona and the JEOL JXA-8520F at Arizona State University (ASU).

The samples were then thoroughly cleaned with mannitol (ultrasonication and soaking) to remove surface boron contamination; this allowed us to have confidence that the subsequent measurements were conducted under ideal conditions. Analyses of the B isotopic composition and the Be/B ratios were obtained with the Cameca IMS-6f secondary ion mass spectrometer at ASU using an $^{16}O^-$ primary beam. The primary accelerating voltage was 12.5 kV and the primary beam current ranged from 15 to 40 nA (resulting in a beam diameter of ~20-30 um). We chose to focus our Be-B analyses on melilite since it is the major carrier of Be in CAIs and typically has higher Be/B ratios than other phases in refractory inclusions [3,5]. Our analysis spots on the melilites in each inclusion were chosen based on backscattered electron images to avoid possible cracks and fine inclusions. We operated the mass spectrometer at a mass resolving power of ~1000 to resolve and avoid hydride and Al^{3+} interferences. We measured ^9Be (8s), ^{10}B (16s) and ^{11}B (4s) between 20 and 150 times for each measurement. At the end of each analysis, ^{28}Si was additionally measured; the (B or Be)/Si ratios were used, in addition to standard measurements, to determine B and Be concentrations. Because the standard (IMT-1 illite with known B content and isotope ratio) was placed as a suspension on the thin sections, analyses of unknowns and standards were obtained without the requirement to replace the sample with a standard block. Beryllium was calibrated against NIST 610, analyzed after (or before) the meteorite sections.

Results: *Sample Description.* One inclusion, TS68, is a lightly altered, compact type A CAI from Allende previously studied by [15]. The two other CAIs (designated 5028_1 and 5028_2) are from the CR2 chondrite NWA 5028. Both have irregular shapes. Inclusion 5028_1 is ~5 mm across, and is dominated by alumi-

nous diopside that encloses patches of melilite (<100 μm across; $Åk_{1-85}$) and anhedral spinel. There are minimal alteration products in CAI 5028_1. Inclusion CAI 5028_2 is ~1 mm across and contains anhedral spinel, typically 10 μm across, enclosed in melilite ($Åk_{4-18}$). The inclusion is surrounded by a pyroxene rim ~40 um thick. There is a small area of secondary anorthite in this inclusion, but it was avoided during analyses.
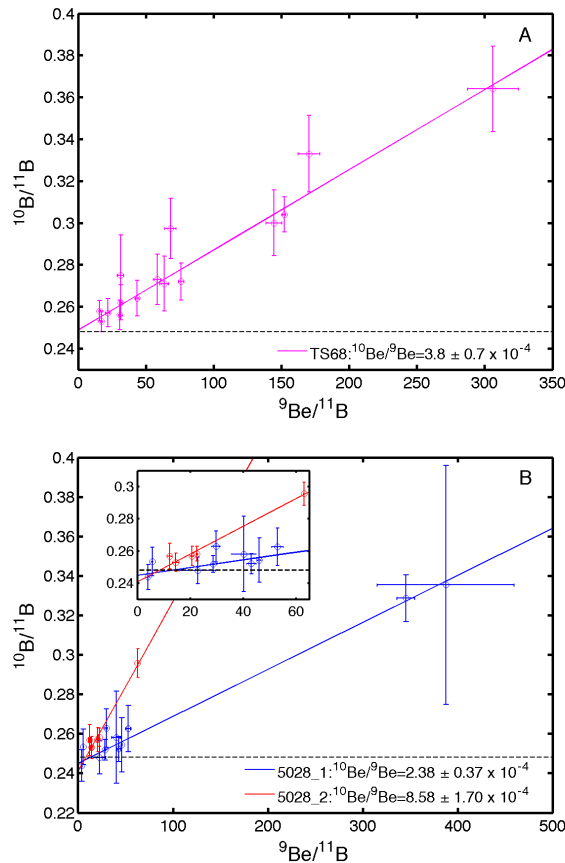
Figure 1: Be-B isochron diagrams for melilite in (A) a CAI (TS68) from Allende; and (B) two CAIs (5028_1 and 5028_2) from the CR2 chondrite NWA 5028. The inset in (B) shows the lower left portion of the figure in greater detail. The horizontal dashed line in each figure represents the chondritic value of $^{10}B/^{11}B$ (=0.2481; [16]). The error bars are 2 sigma, calculated from counting statistics.

Be-B Systematics. Figure 1 shows the Be-B isochron plots for the three CAIs that were analyzed here. The data for the Allende CAI TS68 (Fig. 1A) define a slope corresponding to a $^{10}Be/^{9}Be$ ratio of (3.8 ± 0.7) × 10^{-4} (mean square weighted deviation, MSWD = 1.8) and an initial $^{10}B/^{11}B$ ratio of 0.249 ± 0.004. The data for the NWA 5028 CAI 5028_1 yield a $^{10}Be/^{9}Be$ ratio of (2.4 ± 0.4) × 10^{-4} (MSWD = 1.07) and an ini-

tial $^{10}B/^{11}B$ ratio of 0.246 ± 0.003; those for the CAI 5028_2 yield an isochron with a slope corresponding to a $^{10}Be/^{9}Be$ ratio of (8.6 ± 1.7) × 10^{-4} (MSWD = 0.97) and an initial $^{10}B/^{11}B$ ratio of 0.241 ± 0.005.

Discussion: In previous studies of Allende CAIs, the inferred initial $^{10}Be/^{9}Be$ ratio ranged from 4.8 to 9.5 × 10^{-4} [2-5]. The $^{10}Be/^{9}Be$ ratio that we have obtained for TS68 falls towards the lower end, but is still within the range of these previously reported values when analytical uncertainties are considered. We note that the Be-B systematics in the Allende CAI TS68 show slightly greater scatter (MSWD = 1.8; Fig. 1A) than those in the two NWA 5028 CAIs (MSWD ~1) and may reflect a slight disturbance by secondary processes (involving fluid-rock interactions and thermal effects) on the Allende parent body [13].

The data for the two CAIs from the CR2 chondrite NWA 5028 define good isochrons (MSWDs close to ~1; Fig. 1B). This is also consistent with our petrographic and mineralogic characterization, which indicates a minimal degree of alteration of these two CAIs. In this context, it is interesting to note that CAI 5028_2 has a $^{10}Be/^{9}Be$ ratio (8.6 × 10^{-4}) that is a factor of ~3 higher than that of CAI 5028_1. Since CR2 chondrites are thought to have largely escaped alteration and reheating on their parent body, we believe that the variation in the $^{10}Be/^{9}Be$ ratio observed here for the two NWA 5028 CAIs cannot be attributed to secondary processes and is indicative of gross heterogeneity in the distribution of ^{10}Be in the solar nebula. This, in turn, presents a strong argument in support of ^{10}Be production by local irradiation of nebular gas or dust.

References: [1] Davis A.M. & McKeegan K.D. (2014), *Treatise on Geochemistry (2nd Ed.),* p.361. [2] McKeegan K. et al. (2000) *Science 289,* 1334. [3] Sugiura N. et al. (2001) *MAPS, 36* 1397. [4] MacPherson G. et al. (2003) *GCA, 67,* 3165. [5] Chaussidon M. et al. (2006) *GCA, 70,* 224. [6] Liu M.-C. (2009) *GCA, 73,* 5051. [7] Wielandt D. et al. (2012) *ApJ, 748,* 25. [8] Gounelle M. et al. (2013) *ApJ, 763,* 33. [9] Desch S. et al. (2004) *ApJ, 602,* 528. [10] Gounelle M. et al. (2001) *ApJ, 548,* 1051. [11] Bricker G. & Caffee M. (2010) *ApJ, 725,* 443. [12] Krot A. N. et al. (1995) *MAPS, 30,* 748. [13] Scott E. R. D. et al. (1992) *GCA, 56,* 4281. [14] Aléon J. et al. (2002) *MAPS, 37,* 1729. [15] Simon S. et al. (1999) *GCA, 63,* 1233. [16] Zhai M. et al. (1996) *GCA, 60,* 4877.

THE ROLE OF DIFFERENTIATION PROCESSES IN MARE BASALT IRON ISOTOPE SIGNATURES.
K. B. Williams[1], M. J. Krawczynski[1], N. X. Nie[2], N. Dauphas[2], H. Couvy[1], M. Y. Hu[3], and E. E. Alp[3], [1]Department of Earth and Planetary Sciences and McDonnell Center for the Space Sciences, Washington University, 1 Brookings Dr., St. Louis, MO 63130 (k.b.williams@wustl.edu), [2]Origins Laboratory, Department of the Geophysical Sciences and Enrico Fermi Institute, The University of Chicago, [3]Advanced Photon Source, Argonne National Laboratory.

Introduction: A distinct dichotomy exists between the bulk Fe-isotopic compositions of the high titanium and low titanium mare basalts [1-5]. High-Ti basalts have an average $\delta^{56}Fe=+0.191\pm0.020$‰, while low-Ti basalts have an average $\delta^{56}Fe=+0.073\pm0.018$‰ [4]. To date, there is no satisfactory explanation for the difference in Fe-isotopic composition, and the question remains as to which high-temperature processes could lead to such large fractionation. Here, we assess the potential role of igneous differentiation processes in producing the observed Fe-isotope dichotomy.

Isotopic compositions of olivine and ilmenite mineral separates were measured previously in lunar basalts, dunites, and troctolites [5,6]. [5] found $\delta^{56}Fe_{ilmenite}$ to be between +0.16 to +0.24 ‰ for low-Ti basalts, and +0.20 to +0.42 ‰ for high-Ti basalts. Comparison of the isotopic compositions from each ilmenite sample and its bulk rock shows that ~2/3 of the ilmenites measured by [5] are isotopically "heavy" ($\delta^{56}Fe_{ilmenite} > \delta^{56}Fe_{bulk}$), while the remaining 1/3 of the analyzed ilmenites are isotopically "light" ($\delta^{56}Fe_{ilmenite} < \delta^{56}Fe_{bulk}$). [6] measured similar isotopic compositions for lunar ilmenites ($\delta^{56}Fe_{ilmenite} = +0.18$ to +0.32 ‰), however all ilmenites are isotopically heavy compared to the bulk sample composition. In contrast, previous Mössbauer studies of ilmenite and basalt vibrational properties predict ilmenite to be isotopically light [7]. Olivines from lunar dunites analyzed in [6] have $\delta^{56}Fe_{olivine}$ between -0.43 to -0.23 ‰, and are considerably lighter than the mare basalts. These values, if representative of equilibrium fractionation from a mare basalt-like parent melt, differ significantly from the predicted Fe-isotope fractionation determined by Nuclear Resonant Inelastic X-ray Scattering (NRIXS) in [8], which found no significant fractionation between olivine and basaltic melt at lunar-like fO_2.

The results from [5-8] suggest crystallization of olivine and ilmenite changes the isotopic composition of the residual melt. This fractionation may explain the iron isotope dichotomy between high-Ti and low-Ti basalts if each experienced different degrees of ilmenite and/or olivine fractionation. However, the discrepancy between mineral separate analyses and NRIXS interpretations generates uncertainty as to *how* the melt would evolve with the crystallization of each mineral.

The major distinction between high-Ti and low-Ti basalts is Ti content; this suggests the dichotomy may

Table 1. Force constant, <F> (N/m), and 2σ error derived from NRIXS data in this work.

|	<F>	error
Green Glass	189	9
Yellow Glass	195	12
Orange Glass	203	11
Black Glass	191	11
Ilmenite	156	10
Fo$_{82}$ Olivine [8]	197	10

be an effect of melt composition. In order to investigate the effect of melt composition on Fe-isotope fractionation, we have obtained NRIXS data on synthetic lunar volcanic glasses. We have combined our results with those of previous studies to model fractionation of ilmenite and olivine from lunar melt compositions.

Experimental and Analytical Methods: We synthesized lunar volcanic glasses from oxide powders according to the Apollo green, yellow, orange, and black glass compositions in [9]. In order to perform the NRIXS measurements, we used ^{57}Fe-enriched Fe_2O_3 powder (96.64% ^{57}Fe). Samples were fused to rhenium loops and glassed at 1400ºC for 3 hours in a vertical gas-mixing furnace using a controlled flow of H_2 and CO_2 gases to buffer the oxygen fugacity at IW-0.06. Each glass sample composition was confirmed by electron microprobe analysis at Washington University in St. Louis. The NRIXS method measured the inelastic X-ray scattering of nuclear energy transitions in ^{57}Fe, giving information about the vibrational properties of the iron in each sample. With NRIXS we obtain the force constant, which quantifies the strength of the bonds holding iron in position. [8], [10], and [11] have previously characterized the force constants in mineral and glass phases using NRIXS spectra.

NRIXS results: Table 1 presents the force constants calculated from the NRIXS spectra on our synthetic lunar glasses. Additionally, we have obtained NRIXS spectra on a synthetic ilmenite to supplement the Mössbauer derived data in [7]. Within error, the lunar glasses have the same force constant, suggesting the Fe-isotope fractionation is not a function of melt composition. Furthermore, the force constants for the lunar glasses are similar to the force constants generated for reduced (fO_2 = IW) terrestrial basalts in [8].

Comparison of Equilibrium Isotope Partition Coefficients: Using the force constants in Table 1, we predict the equilibrium fractionation factors (α) for

Figure 1. β-factors calculated as a function of temperature from the measured force constants for synthetic Apollo glasses, ilmenite, and olivine [8].
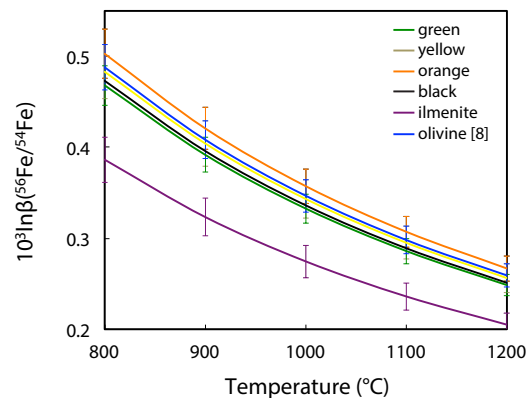
olivine and ilmenite crystallization from each lunar volcanic glass [8]. Our results suggest ilmenite would be isotopically light compared to the parent melt composition (Figure 1). In contrast, olivine shows no significant fractionation. Both of these results conflict with the Fe-isotope fractionations interpreted from analyses of mineral separates [i.e., 6].

To model the isotopic evolution during near-fractional crystallization, we used an olivine-melt Fe-Mg partitioning coefficient (K_D) of 0.3 and an average ilmenite-melt K_D of 1.78 [12,13]. We defined an initial $\delta^{56}Fe_{melt}$, and then tracked the $\delta^{56}Fe_{melt}$, $\delta^{56}Fe_{olivine}$, and $\delta^{56}Fe_{ilmenite}$ during crystallization using the equation:

$$\alpha_{(mineral-melt)} = (\delta^{56}Fe_{mineral} + 1000)/(\delta^{56}Fe_{melt} + 1000) \quad (3)$$

and α values calculated from [5], [6], and this work. Mass balance is considered in each fractionation step of our closed-system model. Figure 2 illustrates the effect of $\alpha_{(mineral-melt)}$ on the isotopic evolution of the residual melts. Our data indicate mineral fractionation will slightly change the residual melt Fe-isotopic composition, but not to the magnitude needed to reach the heavy values of the high-Ti mare basalts.

Ongoing Investigation: Experimental work is being conducted to verify the equilibrium fractionation factors predicted by the NRIXS measurements. In addition, dynamic crystallization experiments are investigating possible kinetic controls on the isotopic fractionation between olivine, ilmenite, and basalt.

NRIXS measurements indicate olivine is not a likely source for the Fe-isotope dichotomy between the low- and high-Ti basalts. However, the NRIXS measurements were taken on glass phases, which may not accurately reflect the iron bonding properties in a high-temperature melt structure. Different degrees of ilmenite fractionation between the two basalt types presents

a more likely alternative; but, the fractionation factors predicted by NRIXS measurements do not produce the magnitude of heavy Fe-isotope enrichment observed in the high-Ti basalts and lunar ilmenite separates. It also seems unlikely that the measured heavy isotope values in ilmenite, a mineral that appears late in the crystallization sequence of mare basalts, represent equilibrium fractionation from a parent melt with mare basalt isotope composition. Ilmenite may be in equilibrium with a significantly fractionated melt prior to crystallization, and may also be affected by diffusive re-equilibration subsequent to crystallization.

Quenched phases in our experimental samples are crushed, sieved, and then hand separated for Fe-isotopic analysis with a Thermo Scientific Neptune Plus MC-ICPMS in the Origins Lab at the University of Chicago. When combined with the isotopic data from mare basalts, the results from these experiments will better constrain the lunar magmatic history and chemical differentiation processes that created the observed Fe-isotope dichotomy.

Figure 2. $\delta^{56}Fe$ evolution of a high-Ti basalt liquid during near-fractional crystallization of olivine (F < 0.4) and ilmenite (F > 0.4). $\delta^{56}Fe$ calculated using α values in [5,6] (blue), and NRIXS-based α for 800°C (green) and 1200°C (red).
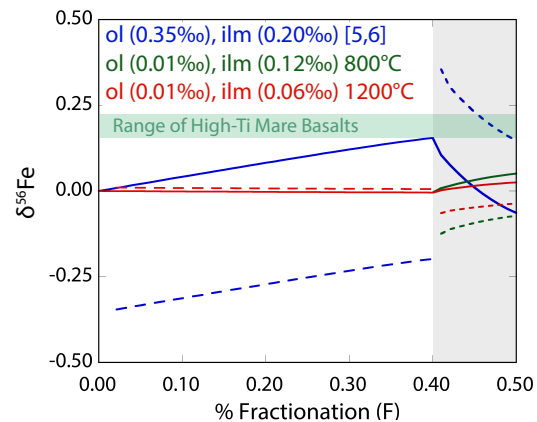
References: [1] Wiesli et al. (2003) *EPSL, 216,* 457-465. [2] Poitrasson et al. (2004) *EPSL, 223,* 253-266. [3] Weyer et al. (2005) *EPSL, 240,* 251–264. [4] Liu et al. (2010) *GCA, 74,* 6249–6262. [5] Craddock et al. (2010) *LPSC XLI,* Abstract #1230. [6] Wang et al. (2015) *EPSL, 430,* 202-208. [7] Polyakov and Mineev (2000) *GCA, 64,* 849-865. [8] Dauphas et al. (2014) *EPSL, 398,* 127-140. [9] Delano (1986) *JGR, 91,* D201-213. [10] Dauphas et al. (2012) *GCA, 94,* 254-275. [11] Polyakov et al. (2007) *GCA, 71,* 3833-3846. [12] VanOrman & Grove (2000) *MaPS, 35,* 783-794. [13] Krawczynski & Grove (2012) *GCA, 79,* 1-19.

CHILI—ACHIEVING ULTIMATE PERFORMANCE FOR THE ANALYSIS OF STARDUST.
T. Stephan[1,2], R. Trappitsch[1,2], A. M. Davis[1,2,3], M. J. Pellin[1,2,3,4], D. Rost[1,2], and C. H. Kelly[1,2], [1]Department of the Geophysical Sciences, The University of Chicago, Chicago, IL 60637, USA, [2]Chicago Center for Cosmochemistry, [3]The Enrico Fermi Institute, The University of Chicago, Chicago, IL 60637, USA, [4]Materials Science Division, Argonne National Laboratory, Argonne, IL 60439, USA. (tstephan@uchicago.edu)

Introduction: After several years of designing and building the Chicago Instrument for Laser Ionization (CHILI) [1, 2], we presented the first analytical results from presolar grains last year [3]. CHILI is a resonance ionization mass spectrometry (RIMS) instrument designed to achieve unprecedented performance with regard to sensitivity (~40 % useful yield), lateral resolution (~10 nm), and number of photoionization lasers (six, allowing measurement of isotopic compositions of several elements at once). As an initial demonstration, we had analyzed presolar SiC grains for the isotopic compositions of Sr, Zr, and Ba, three elements that are particularly important for understanding the *s*-process in asymptotic giant branch stars [3]. Subsequently, we focused our interest on the analysis of Fe and Ni isotopes and developed a unique laser timing scheme that facilitates measuring all stable isotopes of these elements simultaneously whilst avoiding isobaric interference at mass 58 u. First results for Fe and Ni isotopes measured with CHILI in presolar SiC grains are reported in an accompanying abstract [4].

Complementing previous reports [1–3], the following gives a summary of the measures taken to make such analyses possible, reviews recent technical developments with CHILI, and outlines improvements currently in preparation or underway.

RIMS analysis of Fe and Ni: Measuring all Fe and Ni isotopes usually suffers from unresolvable isobaric interference between ^{58}Fe and ^{58}Ni. Chromium-54 and ^{64}Zn also have to be considered since they interfere with ^{54}Fe and ^{64}Ni, respectively. Therefore, in secondary ion mass spectrometry (SIMS) analysis of presolar grains, only ^{56}Fe, ^{57}Fe, ^{60}Ni, ^{61}Ni, and ^{62}Ni are measured directly, whereas ^{54}Fe is corrected for ^{54}Cr, assuming solar ^{54}Cr/^{52}Cr ratios, ^{58}Ni is corrected for ^{58}Fe, assuming solar ^{58}Fe/^{56}Fe ratios, and ^{64}Ni is not measured at all [5]. RIMS usually circumvents isobaric interferences by only ionizing elements that do not have isotopes with the same nominal mass.

We developed resonance ionization schemes using three lasers each for simultaneously ionizing Fe and Ni (Fig. 1). Nickel usually requires four lasers since a significant fraction of the neutral atoms are in a low lying excited state just above the ground state. When removing sample material by using a 351 nm UV desorption laser, slightly less than half of the neutral atoms are in the ground state and therefore not accessible for the

chosen ionization scheme (Fig 1). The sensitivity is thus relinquished by about 30–50 %.

Isobaric interferences between ^{58}Fe and ^{58}Ni are avoided by delaying the Ni ionization lasers by 200 ns compared to the Fe ionization lasers. This time difference corresponds to a mass difference of ~0.5 u in the time-of-flight mass spectra at the specific mass range. As shown in Fig. 2 (top three spectra), Fe and Ni peaks are clearly resolved, and both ^{58}Fe and ^{58}Ni can be measured simultaneously. We applied this method to eleven presolar SiC grains and performed the first simultaneous analyses of all stable Fe and Ni isotopes in presolar grains. As an example, one mass spectrum from a presolar SiC is also shown in Fig. 2 (bottom). These analyses already outperform all previous measurements of Fe and Ni isotopes, with RIMS [7] and SIMS [5], with regard to analytical precision [4].

Developments achieved over the last 12 months:

New reflectron. The first design of the reflectron in CHILI's time-of-flight mass spectrometer turned out to have some imperfections, and the reflectron was poorly aligned with the rest of the system. We therefore redesigned and replaced the reflectron, and performed a precise mechanical alignment. This successful operation allowed us to increase the acceleration voltage for the photoions and lead to higher mass resolution, higher transmission, less noise on the detector, and an overall increase in instrument stability.

Electromagnetic interference mitigation. To minimize electromagnetic interference, passive shielding and an active electromagnetic field cancelation system were installed in the CHILI laboratory.

Raw data acquisition. We developed software for single shot data acquisition, recording detector arrival times for each individual photoion.

Data evaluation. We developed software for evaluating such raw data, which turned out to be necessary for a proper correction of fluctuating signal intensities, which could lead to major dead time effects [6].

Current developments: In order to finally achieve the performance CHILI is designed for, several technical developments are underway that should be finished within this year. Since CHILI already outperforms previous instruments, these developments are done in parallel to analyzing more samples.

Motionless blanking. CHILI has not achieved the high lateral resolution it is designed for. This is mostly

due to the fact that the Ga primary ion beam is swept over the sample when blanking the beam. Together with Orsay Physics, the manufacturer of our liquid metal ion gun, we have begun a collaborative effort to develop a motionless blanking system for our gun.

Neutral background. This redesign will also prevent neutrals, which are produced in the gun, from reaching the sample and causing substantial background signals.

Multiple reflection prisms. We are about to finish the design of a pair of prisms that will let the laser light pass eight times through the analysis chamber in order to significantly increase the sensitivity.

References: [1] Stephan T. et al. (2013) *LPS 44,* #2536. [2] Stephan T. et al. (2014) *LPS 45,* #2242. [3] Stephan T. et al. (2015) *LPS 46,* #2825. [4] Trappitsch R. et al. (2016) *LPS 47,* this conference. [5] Marhas K. K. et al. (2008) *ApJ, 689,* 622–645. [6] Stephan T. et al. (1994) *JVST A, 12,* 405–410. [7] Trappitsch R. et al. (2012) *LPS 43,* #2497.
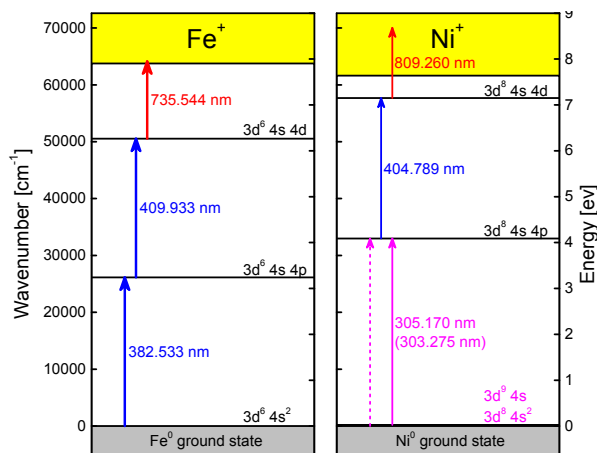

Fig. 1: Resonance ionization scheme for Fe and Ni. Most of the neutral Ni atoms are in a low lying state (3d⁹ 4s) just above the ground state. Therefore, and since CHILI provides only six Ti:sapphire lasers, Ni atoms in the ground state are omitted.
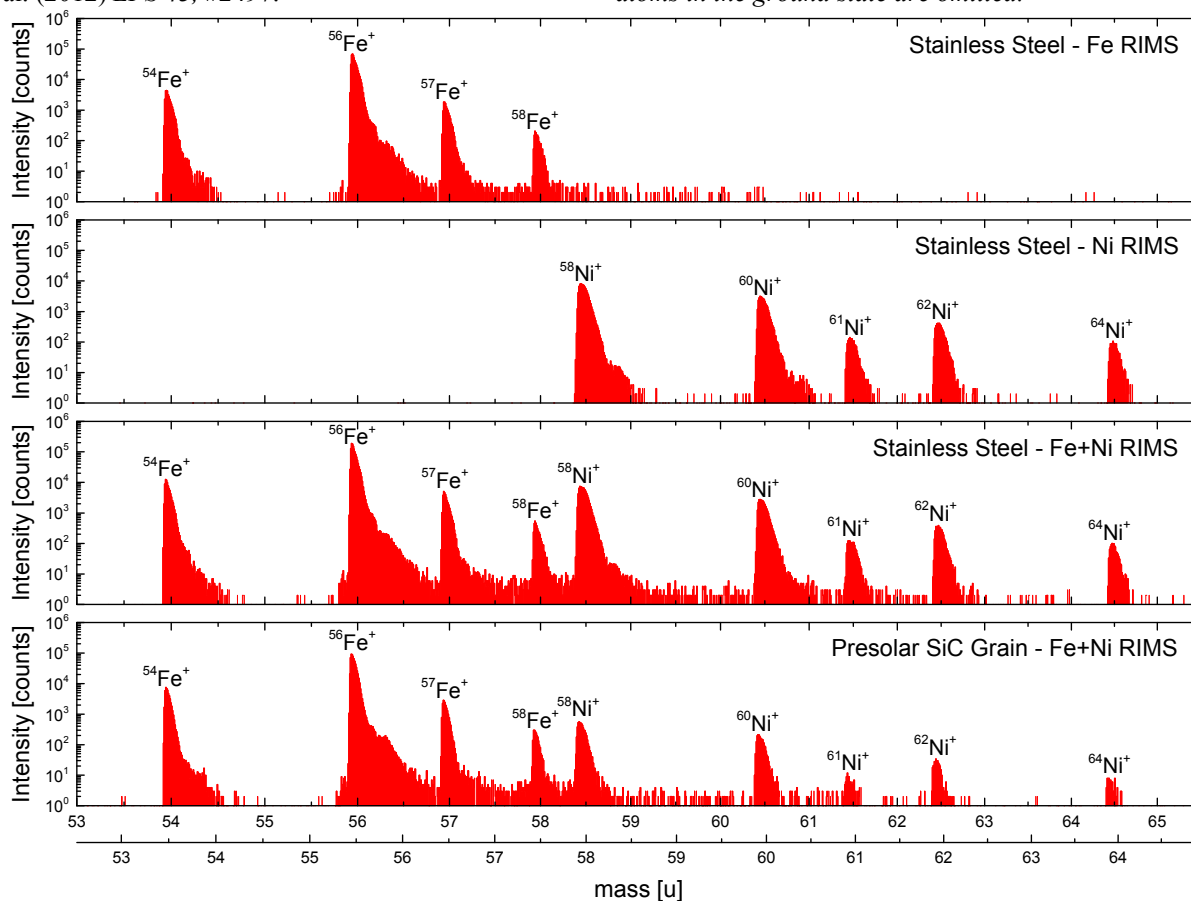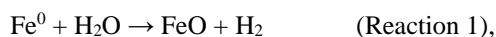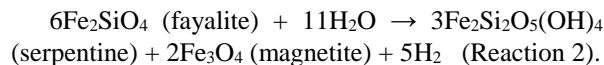

Fig. 2: RIMS spectra measured with CHILI. The first three spectra are measured on a stainless steel sample, first, by only using three lasers that were tuned for resonance ionization of Fe, then, by using three lasers tuned for Ni. The third spectrum, eventually, was measured using all six lasers combined. The fourth spectrum shows an Fe-Ni spectrum from a presolar SiC grain [4]. In order to avoid isobaric interference at mass 58 u, firing of the lasers tuned for Ni was delayed by 200 ns compared to firing of the Fe lasers. This time difference corresponds to a mass difference of ~0.5 u in this mass range. This can be seen in the two mass scales shown; the upper mass scale was calibrated using the Fe mass peaks, the lower mass scale was calculated from the Ni mass peaks.

CONSTRAINTS ON H_2O AND H_2 PROPORTIONS IN THE VOLATILE ENVELOPES OF YOUNG, H_2-PRODUCING, SMALL-RADIUS EXOPLANETS.

M. Melwani Daswani[1] and E. S. Kite[1], Department of the Geophysical Sciences, University of Chicago (5734 S Ellis Ave., Chicago, IL 60637, melwani@uchicago.edu).

Introduction: Small-radius exoplanets with low densities discovered by *Kepler* could have either accreted their volatiles from the nebular disk, or produced them via outgassing, i.e., through water-rock interaction. In the simplest scenario, *Kepler* exoplanets can be interpreted as rocky Earth-like core compositions, under a low molecular weight enveloping layer dominated by H_2. Two main reactions can generate H_2 in planetary formation conditions: elemental Fe oxidation [e.g., 1]:

$$Fe^0 + H_2O \rightarrow FeO + H_2 \qquad \text{(Reaction 1)},$$

and Fe-silicate hydration [e.g., 2]:

$$6Fe_2SiO_4 \text{ (fayalite)} + 11H_2O \rightarrow 3Fe_2Si_2O_5(OH)_4 \text{ (serpentine)} + 2Fe_3O_4 \text{ (magnetite)} + 5H_2 \quad \text{(Reaction 2)}.$$

In order to test the potential for small-radius exoplanets to generate the entire volatile inventory of their envelopes from water-rock interaction, we must first constrain the equilibrium H_2O/H_2 for plausible fO_2 conditions that existed during planetary formation, since the upper weight limit of the envelope is ~ 1.7 wt. % for terrestrial-like rocky core compositions [3, 4, 5].

Methods: H_2O/H_2 was calculated for 5 log units below the iron-wüstite (IW) fO_2 buffer to 2 log units above IW, at pressures of 1 and 10 kbar, and varying temperatures using the van Laar gas mixing model [6], and the compensated-Redlich-Kwong ("CORK") equation of state and CHO program by T. Holland [7] for H_2O and H_2 molar volumes in mixed gases. Low H_2O/H_2 would signify that a low molecular weight envelope could be achieved at planet-forming conditions and may be achieved by outgassing, whereas high H_2O/H_2 would produce a high molecular weight envelope – a "water-world" different from the two-layer (core + envelope) models of e.g., [8, 9].

Results: Fig. 1 summarizes the H_2O/H_2 calculations for the studied range of conditions. Overall, for fO_2 from IW-2 to IW+2, H_2O/H_2 increases at 10 kbar compared to 1 kbar, while at IW-5 to IW-3, H_2O/H_2 is comparable at both pressures. Temperature also has a more marked effect on the ratio at 10 kbar than at 1 kbar, with IW-2 to IW+2 decreasing H_2O/H_2 sharply from 200 to 1000 °C.
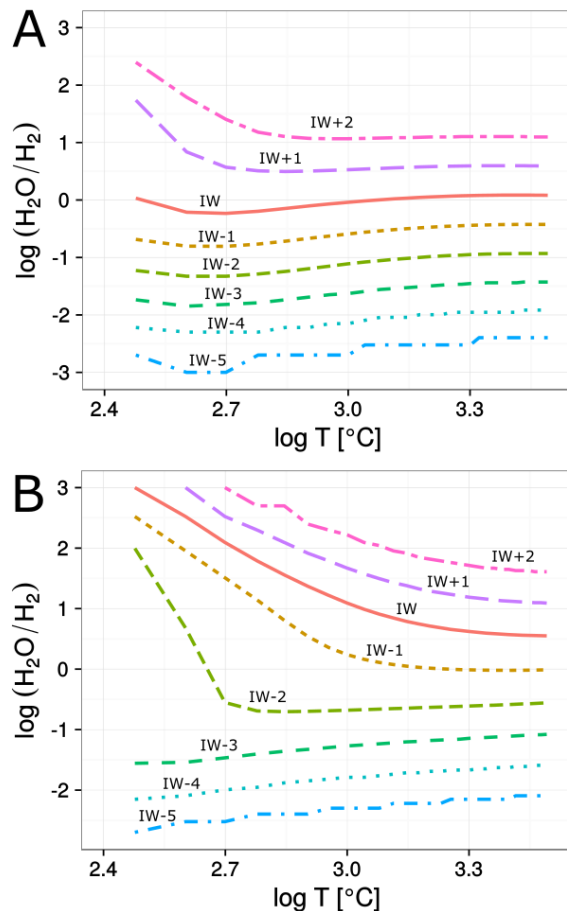
Figure 1. $\log_{10}(H_2O/H_2)$ as a function of ($\log_{10}$) temperature at specified fO_2 conditions, calculated for A) 1 kbar pressure, and B) 10 kbar.

Discussion and further work: Constraints can now be placed on the fO_2 conditions during planetary formation if outgassing produced the low molecular weight envelopes of small-radius exoplanets. Further refinements to the H_2O/H_2 could be carried out by calculating the ratio with different equations of state (e.g., Pitzer-Sterner [10]) and extending the range of H_2O/H_2 values to higher temperatures.

In future work, we will integrate these constraints with calculations of H_2 production in a thermally evolving planet using a dynamical model incorporating nebular disk migration. The model will account for H_2 accretion and loss to space, water-rock interactions during planetary accretion and up to the planetary embryo stage, and surface-interior recycling of volatiles.

The model results will be compared to constraints for the abundance of volatiles on small-radius planets discovered by *Kepler* and *K2*, using mass constraints from Radial Velocity and Transit-Timing Variation analyses.

References: [1] Lange M. A. and Ahrens T. J. (1984) *Earth Planet. Sci. Lett. 71,* 111 − 119. [2] McCollom, T. M. and Bach W. (2009) *Geochim. Cosmochim. Acta 73,* 856 − 875. [3] Elkins-Tanton L. T. and Seager, S. (2008) *Astrophys. J. 685*, 268 − 288. [4] Elkins-Tanton L. T. and Seager, S. (2008) *Astrophys. J. 688*, 628 − 635. [5] Rogers L. A. et al. (2011) *Astrophys. J. 738:59*, 16pp. [6] Holland T. and Powell R. (2003) *Contrib. Mineral. Petrol. 145*, 492 − 501. [7] Holland T. and Powell R. (1991) *Contrib. Mineral. Petrol. 109*, 265 − 273. [8] Howe A. R. et al. (2014) *Astrophys. J. 787:173*, 22pp. [9] Jontoff-Hutter et al. (2014) *Astrophys. J. 785:15*, 14pp. [10] Pitzer K. S. and Sterner S. M. (1994) *J. Chem. Phys. 101*, 3111.

CHEMICAL AND ISOTOPIC FRACTIONATION DURING EVAPORATION OF SYNTHETIC AOA- and FOB-LIKE MATERIALS.

R. A. Mendybaev[1,2] and F. M. Richter[1,2], [1]Department of the Geophysical Sciences, [2]Chicago Center for Cosmochemistry, University of Chicago, Chicago, IL (ramendyb@uchicago,.edu).

Introduction: Forsterite-bearing Type B (FoB) Ca-, Al-rich inclusions (CAIs) have igneous textures and consist of pyroxene, spinel, åkermanitic melilite, anorthite and abundant forsterite grains, which distinguish them from other types of CAIs (e.g., [1–4]). Chemically, they are enriched in magnesium and silicon compared to Type A and Type B CAIs. Some FoBs (e.g., Vigarano 1623-5, Allende CG-14 and TE) are characterized by very large mass-dependent isotopic fractionations in magnesium, silicon and oxygen isotopes (with $\delta^{25}Mg$ and $\delta^{29}Si$ up to ~18‰ and ~7‰ in CG-14 [1] or ~30‰ and ~10‰ in 1623-5 [3], indicating high degrees of melting of forsterite-rich precursors and evaporative loss of these moderately volatile elements. Most FoBs, however, show only small isotopic fractionations, and are characterized by continuous forsterite-free outer mantles surrounding forsterite-rich cores. Based on textural, chemical (Fig. 1) and isotopic characteristics, Bullock et al. [4] argued that FoBs could have formed only by partial melting of forsterite-rich amoeboid olivine-rich aggregates (AOAs), which are believed to be aggregates of solar nebular condensates (e.g., [5, 6]).

Here we present the results of our experiments in which forsterite-rich compositions were evaporated in vacuum and in hydrogen-rich gas at various temperatures in order to test the proposition that AOAs are precursor of FoBs.

Results and Discussion: Fig. 2 shows MgO and SiO_2 contents of AOAs and FoBs along with compositions of residues produced by evaporation of AOA-like (FUN1, FUN2 and FUNC) and FoB-like (CAI4) melts in vacuum at 1900°C. It shows that, after initial, faster evaporation of Si relative to Mg (FUNC) or Mg relative to Si (FUN1), evaporation trajectories of AOA-like melts converge to a single trend which evolves toward the Type A and Type B CAIs and away from typical FoBs. The same trend was also observed when extremely Mg-rich (60 wt% MgO and 30 wt% SiO_2) or Si-rich (50 wt% SiO_2 and 30 wt% MgO) melts were evaporated at the same conditions [7]. Another important feature of Fig. 2 is that chemical compositions of FUN and FUN-like CAIs (C1, CMS-1, CG-14, 1623-5) plot on or very close to the evaporation trajectories of synthetic AOA-like melts. Silicon, magnesium and oxygen isotopic compositions of the experimental evaporation residues with chemical compositions close to those of C1, CMS-1 and 1623 are within few permil of those measured in the inclusions [3, 7-10].

Fig. 2 shows that chemical compositions of residues produced by evaporation of FoB-like melt (CAI4) follow the same trend established by evaporation of significantly Mg- and Si-rich compositions. The CAI4 evaporation produces residues with chemical compositions very close to those of C1 and CMS-1 FUN CAIs, but with significantly less isotopic fractionation: e.g., $\delta^{25}Mg$ ~ 8‰ and $\delta^{29}Si$ ~ 7‰ in the evaporation residue compared to $\delta^{25}Mg$ ~30‰ and $\delta^{29}Si$ ~ 15‰ in C1 and CMS-1.
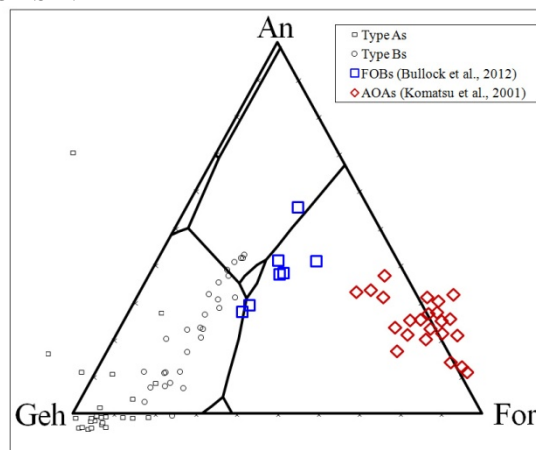

Fig. 1. Bulk chemical compositions of FoBs [4] and AOAs [5] projected onto the anorthite-gehlenite-forsterite ternary diagram.
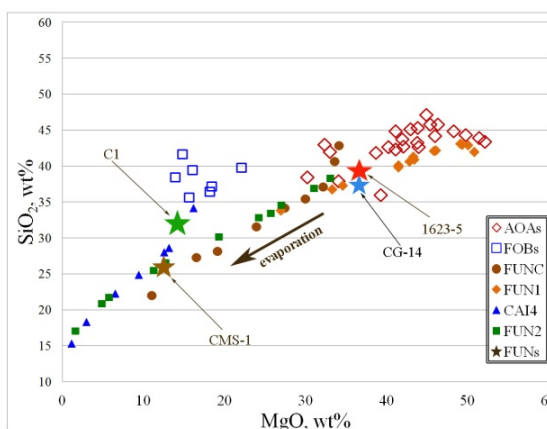

Fig. 2. Bulk chemical compositions of AOA, FoB and FUN (and FUN-like) CAIs in MgO-SiO₂ space. Also shown are compositions of residues produced by evaporation of AOA-like (FUN1, FUN2 and FUNC) and FoB-like (CAI4) melts in vacuum at 1900°C.
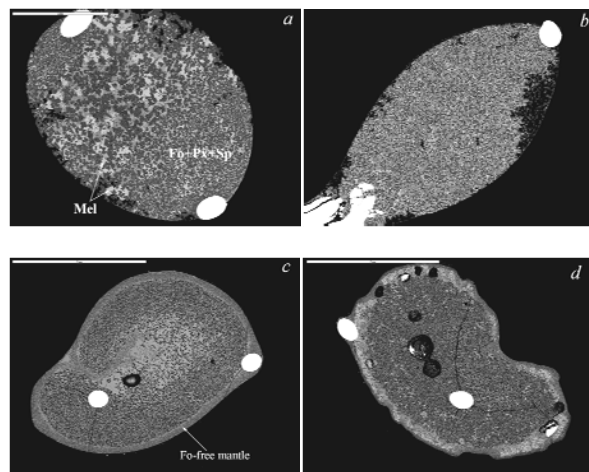
Fig. 3. Backscattered electron images of evaporation residues: a) the starting material was evaporated in vacuum at 1600ºC for 2 hr followed by cooling to 1500ºCº at 60ºC/h; the furnace temperature was then dropped to 1000ºC at which the sample was annealed for ~10 hr and then reheated to 1300ºC and cooled to 900º at 30ºC/hr (total weight loss ~4%); b) the starting material was cooled in vacuum from 1500ºC to 900ºC at 30ºC/hr (total weight loss ~1%);c) the starting material was cooled in 1 atm hydrogen from 1500ºC to 1350ºC at 50ºC/hr, then to 1200ºC at 25ºC/hr and to 1100ºC at 10ºC/hr (total weight loss ~13%); d) sample with the same initial cooling history as sample shown in panel c (weight loss ~12.5%), but later the sample was annealed at 1300ºC in 1 atm hydrogen for ~215h (additional weight loss of ~11.5%). Scale bars in panels a and b are 1 mm, and in panels c and d are 2 mm.

Fig. 3 shows typical textures produced when an AOA-like starting material with a chemical composition close to that of 1623-5 FUN CAI was cooled at subliquidus temperatures in vacuum (panels *a* and *b*) and in 1 atm hydrogen (panels *c* and *d*). When heated and cooled in vacuum at subliquidus temperatures, very little weight loss was observed: ~4% for sample cooled from 1600ºC (Fig. 3a) and less than 1% for sample cooled from 1500ºC (Fig. 3b). Fig. 3a and 3b show that there are no textural differences between the inner and outer parts of these once partly partially molten droplets. The sample shown in panel *a* consists of melilite-rich (with forsterite + pyroxene + spinel) and melilite-poor parts (as 1623-5 FUN CAI). It has a somewhat more coarse-grained texture than the sample shown in panel *b*, which consists of forsterite, pyroxene and spinel. Lack of melilite in this sample is due to the difficulty of rystallizing melilite from melts heated significantly above the melting temperature of melilite, which destroy its nucleation sites [11-13]. Formation of melilite in the sample shown in panel *a*, which was heated to even higher temperatures, is due to annealing

at 1000ºC, which recreates melilite nucleation sites and makes its crystallization possible.

When the same AOA-like starting material is melted at the same temperatures as in vacuum experiments but in 1 atm of hydrogen, significant weight loss caused by evaporation of silicon and magnesium is observed. Moreover, a forsterite-free outer mantle consisting of pyroxene and spinel, similar to that in natural FoBs [4] was observed in all experiments when partially molten droplets were exposed to hydrogen (Fig. 3c and 3d). Formation of forsterite-free mantles in hydrogen-rich gas is caused by faster evaporation of magnesium and silicon from the surface of the partially molten droplet compared to their diffusion rates in the droplet. Evaporation of magnesium and silicon from such droplets in a low-pressure, hydrogen-dominated, solar nebular gas would result in both chemical and isotopic fractionation. The thickness of forsterite-free mantle in experimental charges was observed to vary from ~10 µ to ~100 µm depending on temperature and cooling rates.

Conclusions: The experimental data presented here suggest that AOAs are very plausible precursors of FOBs: 1) high-temperature evaporation of AOA-like compositions produces residues with chemical and isotopic compositions like those observed in FUN (and FUN-like) FoBs; 2) subliquidus evaporation of AOA-like compositions in 1 atm hydrogen produces residues with textures and chemical compositions very similar to those of typical FoBs. In a low-pressure, hydrogen-dominated, solar nebular gas, evaporation of magnesium, silicon and oxygen will also result in their isotopic fractionation.

References: [1] Clayton R. N. et al. (1984) *Geochim. Cosmochim. Acta, 48,* 533–548. [2] Wark D. A. et al. (1987) *Geochim. Cosmochim. Acta, 51,* 607–622. [3] Davis A. M. et al. (1991) *Geochim. Cosmochim. Acta, 55,* 621–638. [4] Bullock E. S. et al. (2012) *Meteoritics & Planet. Sci., 47,* 2128–2147. [5] Komatsu M. et al. (2001) *Meteoritics & Planet. Sci., 36,* 629–641. [6] Krot A. N. et al. (2004) *Chem. Erde, 64,* 185–239. [7] Mendybaev R. A. (2014) *LPS XXXV,* Abstract #2782. [8] Mendybaev R. A. et al. (2013)) *Geochim. Cosmochim. Acta, 123,* 368–384. [9] Williams C. D. et al. (2014). *LPS XXXV,* Abstract #2146. [10] Clayton R. N. (1988) *Phil. Trans. Roy. Soc. London, 325,* 483–501. [11] Stolper E. (1982) *Geochim. Cosmochim. Acta, 46,* 2159–2180. [12] Beckett J. R. (1986) *Ph. D. thesis*, University of Chicago. [13] Mendybaev R. A. et al. (2006)) *Geochim. Cosmochim. Acta, 70,* 2622–2642.

LOSS OF CERES' ICY SHELL FROM IMPACTS: ASSESSMENT AND IMPLICATIONS. J. C. Castillo-Rogez[1], T. Bowling[2], R. R. CR. Fu[3], H. Y. McSween[4], C. A. Raymond[1], N. Rambaux[5], B. Travis[6], S. Marchi[7], D. P. O'Brien[6], B. C. Johnson[8], S. D. King[9], M. T. Bland[10], M. Neveu[11], M. C. De Sanctis[12], O. Ruesch[13], M. V. Sykes[6], T. H. Prettyman[6], R. S. Park[1], C. T. Russell[14]. [1]JPL/CalTech, Pasadena (Julie.C.Castillo@jpl.nasa.gov). [2]Dept. of Geophysical Sciences, University of Chicago. [4]Lamont-Doherty Earth Observatory, Columbia University, New York. [4]Department of Earth and Planetary Sciences, University of Tennessee, Knoxville. [5]IMCCE, Observatoire de Paris, UPMC, France. [6]Planetary Science Institute, Tucson. [7]Southwest Research Institute, Boulder. [8]Brown University, Providence. [9]Department of Geoscience, Virginia Tech. [10]US Geological Survey, Flagstaff. [11]SESE, Arizona State University. [12]Istituto Nazionale di Astrofisica, IAPS, Rome, Italy. [13]NASA GSFC (ORAU), Greenbelt. [14]Department of Earth and Space Sciences, UCLA.

Conundrum: If Ceres formed as an ice-rich body, as suggested by its low density and the detection of ammoniated phyllosilicates [1], then it should have formed an icy shell, analogous to large icy satellites [2]. Instead, *Dawn* observations reveal a weakly differentiated body with a shell dominated by rocky material [3]. Here we argue that Ceres may have lost its original ice shell when it migrated inwards from a cold accretional environment to the warm outer main belt [1], or when the solar nebula dissipated (if formed in situ), as a consequence of frequent exposure by impacting. This hypothesis implies that Ceres' current surface represents the base of the original shell, a region that is extremely rich from a chemical evolution standpoint. This leads to specific predictions that may be tested during *Dawn*'s low-altitude mapping orbit (LAMO). If confirmed, then the contribution of *Dawn* to better understanding other icy worlds will be unprecedented.

Observations: *Dawn* has obtained Ceres' topography and gravity with sufficient accuracy to render previous predictions of its interior structure obsolete. Combined with gravity data [4] and geological observations [5], a new picture of Ceres' internal evolution and current state arises. It challenges earlier predictions for a thick shell dominated by ice [6] or even a dirty ice shell [7], and instead suggests a high-density shell dominated by rocky material.

Previous studies modeled Ceres based on our understanding of large icy satellites [2, 6]. Ceres is expected to have had a deep liquid layer that provided an environment for the aqueous alteration of its rocky material in hydrothermal conditions and led to the observed mineralogy [1]. That ocean froze over a few 10s of My leading to a shell mostly devoid of rocky material [6]. Indeed, large icy satellites exhibit little authigenic silicates on their surfaces. This is also consistent with terrestrial observations of ice sheets that are slowly freezing top-down and tend to reject hard particles and salts [8, 9].

A critical clue to understanding Ceres' current state is its bulk density [4], which points to a (anhydrous) rock to ice volume ratio of 0.85. If Ceres formed in the outer Solar system and preserved its full volatile makeup, its rock to ice volume ratio should be <0.5 [e.g., 10], which implies that Ceres would have lost the

equivalent of a 50-km thick water shell. The original fraction of volatile is expected to be lower if Ceres formed in situ from local rocky material and volatile-rich planetesimals that migrated inwards from the outer Solar System [11].

An Volatile-Rich Body in a Warm Environment: None of the aforementioned models explored the fate of a volatile-rich Ceres exposed to the (relatively) warm environment of the outer main belt, either following migration or when the solar nebula dissipated. It has been generally assumed that a lag deposit would protect Ceres' shell from sublimation, but impact models [12] and the heavily cratered surface of Ceres itself indicate significant disturbance during Ceres' history. During periods of intense impacts Ceres did not have time to rebuild a protective lag layer, leading to ice sublimation and volatile loss. A variety of scenarios lead to the removal of a few tens of kilometers provided that that event happened early in Ceres' history when (a) impact rate was fast and (b) Ceres' icy shell was warm and/or partially molten. Furthermore, if Ceres migrated inward, early impact velocities could have been considerably higher than today as the impacting population was dynamically hot. This could have greatly increased the volume of ice melted/vaporized during impact and the residual temperatures within the craters, accelerating the sublimation.

A New Interior Model for Ceres: We argue here that the "icy satellite" physical analog assumed by [2, 6] could still apply to Ceres, but with a major caveat. Kirk and Stevenson [13] pointed out that when an icy body is undergoing separation of rock from a volatile phase in the liquid state, a fraction of the silicate phase remains in suspension in the ocean. This idea was explored in more detail by [7] who assumed that the particles would become homogeneously trapped in Ceres' shell. However [13] noted that a slowly freezing ice shell does not incorporate rocky particles, even fines. Instead those particles sink at the bottom of the icy shell, helped by solutes that promote flocculation. The porosity of mud so produced, and hence its thickness, is a function of pressure. Oceanic sediments may be taken as an analog; they usually show a porosity of ~ 40% at pressures of 10-40 MPa [e.g., 14]. We infer a thickness of ~160-200 km for Ceres' (current) outer

shell. Pores are filled with ice and salts (anhydrous and hydrated, including carbonates, sulfates) and possibly clathrates hydrates. The salt chemistry is complex but dominated by chloride compounds with minor sulfate species. Combined geochemical (using *Geochemist's Workbench*) and freezing chemistry modeling (with *FREZCHEM* [15]) yields a compositional gradient across that layer, with more ice at the top and more chloride salts at the base. In practice, impacting and convection [16] likely altered the original stratification and introduced lateral heterogeneities in the relative rock to ice and salt content.

Implications for Ceres: The resulting structure (Figure 1) can be represented, to first order, by a core with a density of 2700-2900 kg/m^3 and a ~180 km thick outer shell with a density between 1900-2100 kg/m^3. This model is consistent with gravity observations [4] and hydrothermal evolution modeling [17]. It also explains the absence of very large (>300) km craters. The composition of the rocky component is consistent with the VIR observations, and especially Mg-phyllosilicates, ammoniated clays, and carbonates [1]. Geochemical modeling suggests that the basal layer should also contain salt species such as chlorides and sulfides. This layer plays an important role in moderating heat loss from Ceres' interior owing to the salt low thermal conductivity and the concentration of potassium leached from the rock. Preliminary models indicate that it could remain warm until present, at least warm enough to host the source of the cryovolcanic features inferred by [5], promote global relaxation [3], and provide a context for explaining the production of ammoniated phyllosilicates [18].

Big Picture: Partially differentiated interiors may be a common feature of mid-sized icy bodies that went through a phase of ice melting and hydrothermal activity [e.g., 13, 19]. Dawn's GRaND instrument has the capability to detect markers of hydrothermal environments [20], which can help test the proposed model. High-resolution images obtained during LAMO would help link geological features and small-scale color variations to interior composition. Clathrates, ices, and rock mixtures find an analog with permafrost, and evidence for destabilization patterns (e.g., pitted terrains) may be observable at high resolution.

The implications of seeing the base of the original ice shell in an object believed to have undergone hydrothermal processes similar to those predicted for icy satellites [e.g., 21, 22] are profound. If confirmed, this would open a new dimension in our quest to assess the astrobiological significance of these objects: the *z*-dimension. Also, it would underscore Ceres as a new playground for exobiology research, just a couple AU away from Earth.

References: [1] De Sanctis M. C. et al. (2015) *Nature* 528, 241. [2] McCord, T. B. and C. Sotin (2005) JGR 110, E05009. [3] Fu, R., et al. (2015) *AGU Fall Meeting*. [4] Park, R., et al. (2016) this conference; [5] Ruesch, O., et al. (2016) this conference. [6] Castillo-Rogez J. and McCord T. B. (2010) *Icarus* 205, 443. [7] Neveu M. and Desch S. J. (2015) *GRL*, in press. [8] Lake, R. A. and E. L. Lewis (1970) JGR 75, 583. [9] Schmidt, G. and D. Dahl-Jensen (2003) *Ann. Glac.* 37, 129. [10] Castillo-Rogez, J., et al. (2012) *Icarus* 219, 86. [11] Turner, N., et al. (2012) *ApJ* 794, 92. [12] Bowling, T. J., et al. (2015) *AbSciCon*, 7878; [13] Kirk, R. L. and D. J. Stevenson (1987) *Icarus* 69, 91. [14] Nafe, J. E. and C. L. Drake (1961) DTIC AD0466981; [15] Marion, G. (2009) Wkshp on Modeling Martian Hydrous Environments, #40-41. [16] King, S. D., et al. (2016) this conference. [17] Travis, B., et al. (2015) *AGU Fall Meeting*. [18] McSween, H. Y., et al. (2016) this conference. [19] Roberts, J. H. (2015) *Icarus* 258, 54.; [20] Prettyman, T. H., et al. (2016) this conference, #2228; [21] Ransford (1981) *Science* 289, 21-24. [22] McKinnon, W. B. and M. E. Zolensky (2003) *Astrobiology* 3, 879-897.

Figure 1. Interior evolution model suggested for Ceres, constrained by Dawn observations.
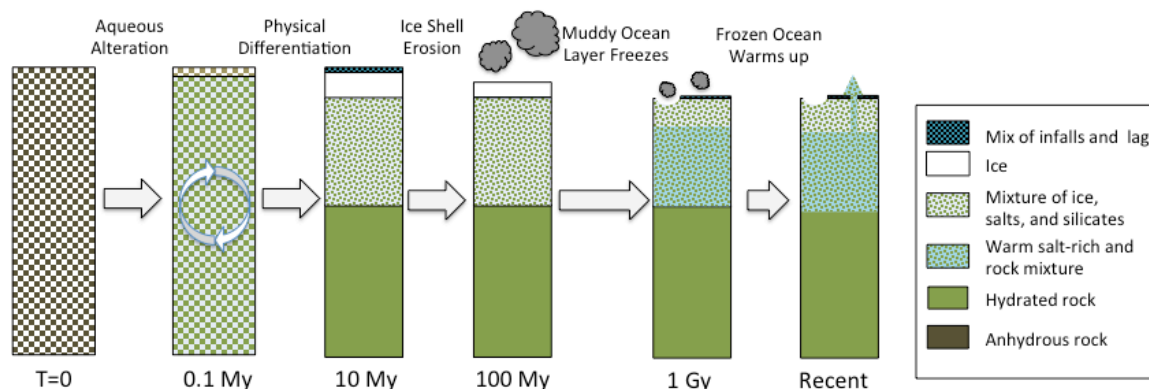
Titanium isotopic anomalies, titanium mass fractionation effects, and rare earth element patterns in Allende CAIs and their relationships. A. M. Davis[1,2,3], J. Zhang[1,3,*], J. Hu[1,3], N. D. Greber[1,3], and N. Dauphas[1,2,3], [1]Department of the Geophysical Sciences, [2]Enrico Fermi Institute, [3]Chicago Center for Cosmochemistry, The University of Chicago (a-davis@uchicago.edu); [*]Present address: Hong Kong.

Introduction: Mass fractionation effects in Mg, Si, and Ca in CAIs have been known for several decades [1] Non-mass-dependent anomalies in ^{50}Ti in CAIs and bulk meteorites have also been known for decades, but have received renewed interest in recent years with the development of multicollector inductively coupled mass spectrometry (MC-ICPMS). Although ^{50}Ti variations have been well known for some time, a correlated anomaly in ^{46}Ti in bulk meteorites has been found [2,3]. We report here both mass-dependent fractionation (MDF) and non-mass-dependent (NMD) Ti isotopic compositions of 32 Allende CAIs. We also measured rare-earth element (REE) patterns of many of the samples, since a correlation between the magnitude of Ca mass fractionation effects and volatility controlled REE patterns has been reported [4].

Methods: The CAIs are from four Allende slabs (*AL8,S8*; *AL10,S2*; *AL3,S5*; *AL,ASU*). They were drilled out using a microdrill system, with the drilling diameter of 500 μm and the drilling depth of ∼250 μm. One or two spots were drilled for each CAI. After sample digestion, Ti was separated via a two-stage procedure using TODGA and AG1-X8 resins [5]. The full procedural blank is ~10 ng. Ti isotopic analyses were obtained with a Thermo Neptune MC-ICPMS using sample-standard bracketing technique at high resolution [5]. The bracketing standard is natural rutile from Krageröe, Norway purified by column chemistry. The measured Ti isotopic compositions including both Ti MDF and NMD effects are expressed in δ′ notation. Ti NMD effects are reported in ε notation after normalization to ^{49}Ti/^{47}Ti = 0.749766 [5] and correcting for MDF using an exponential law.

In order to test the precision of Ti mass fractionation measurements by sample-standard bracketing, we measured Ti isotopes in seven sample solutions by double spiking using a newly developed method [6]. For these measurements, an aliquot of the solution obtained after dissolution of the CAI was double-spiked and chemically purified. There is a good correlation between double-spiked and sample-standard bracketing measurements (Fig. 1), indicating that the latter have uncertainties of about 0.5‰, much smaller than the overall range of 7‰.

The solutions from the first ten samples were consumed in the initial Ti isotopic analyses, but the solutions from the remaining 22 samples were used to measure rare earth element patterns by MC-ICPMS [7]. Since the microdrilled samples were not weighed (in order minimize sample loss), we assumed that all analyzed CAIs contained 1.28 wt% Ti, the average Ti content of CAIs. This

leads to uncertainties in overall REE concentrations of at least a factor of two, but does not affect REE patterns.
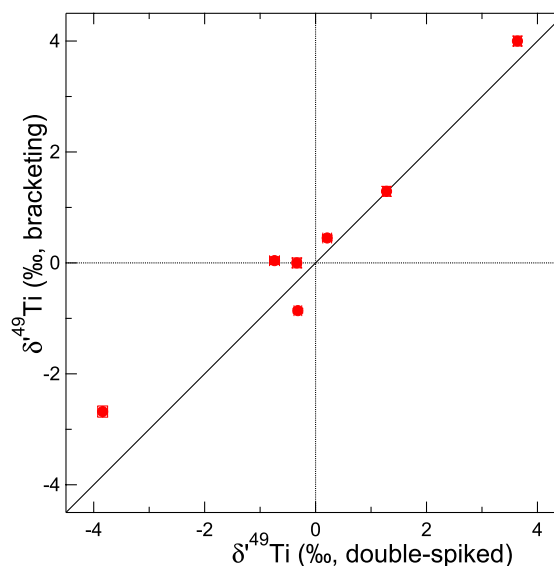

Fig. 1. Data measured by sample-standard bracketing are well correlated with double spiked data.

Each CAI was x-ray mapped and imaged in backscattered electrons in the slab surface. We further examined the slab after microdrilling to identify minerals by x-ray microanalysis. This clearly did not provide a thorough petrographic description of each CAI, but did allow classification into coarse- and fine-grained types and subdivision of coarse-grained CAIs into Types A and B.

Results and discussion: CAIs have δ′^{xx}Ti/^{47}Ti values following or paralleling the MDF lines determined by evaporating perovskite [8], depending on whether there are NMD effects. The range in MDF effects is quite large, extending from δ′^{49}Ti/^{47}Ti of –3 to +4‰. This is in contrast to Ca, where MDFs range from near normal to isotopically light compositions; isotopically heavy Ca only occurs in FUN CAIs [1]. After internal normalization to ^{49}Ti/^{47}Ti, we found that the Ti anomalies of ε^{50}Ti and ε^{46}Ti in CAIs are highly correlated, but variable in magnitude, in contrast to the constant magnitude anomalies reported two Allende and two Efremovka CAIs [2]. The linear correlation between ε^{50}Ti and ε^{46}Ti extends the same correlation seen among bulk solar system objects. This observation provides constraints on the dynamic mixing of the solar disk.

The CAIs have a variety of REE patterns, but basically can be subdivided into relatively unfractionated Group I and volatility fractionated Group II patterns (Fig. 2). There are some interesting features in the light REE

that are controlled by volatility also, but these will not be explored in detail here.
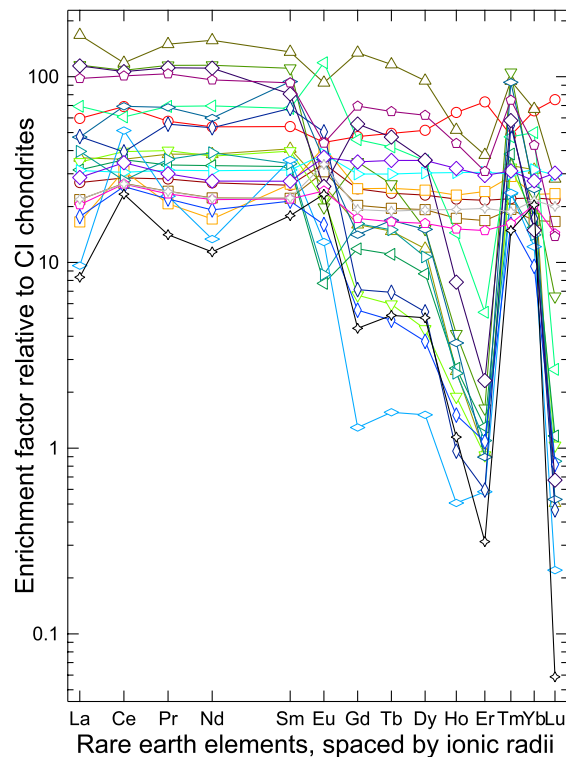

Fig. 2. REE patterns in 22 of the 32 CAIs analyzed for Ti isotopes, normalized to CI chondrite abundances [7].

A correlation has been reported between REE patterns and Ca MDF isotopic effects, with CAIs having Group II REE patterns having more isotopically light Ca. Despite Ti showing a somewhat wider range of MDF effects, no such correlation was found between REE patterns and (Fig. 3). Here we plot $\delta'^{49}Ti/^{47}Ti$ vs. CI normalized Lu/La ratios, as Lu is strongly depleted relative to La in Group II CAIs and undepleted in Group I. There does seem to be a wider range of $\delta'^{49}Ti/^{47}Ti$ values among Group II CAIs, suggesting kinetically controlled volatility fractionation of Ti during REE fractionation. This makes sense as high temperatures are required for both kinds of fractionation, but it is not clear why both isotopically heavy and light Ti is found in Group II CAIs. Formation of Group II REE patterns requires removal of an ultrarefractory dust followed by condensation of the remaining gas [9,10].

There is also no correlation between $\varepsilon^{50}Ti$ and REE patterns (Fig. 4). This is perhaps less surprising than the lack of correlation between REE patterns and Ti MDF effects. There is a significant range in the magnitude of $\varepsilon^{50}Ti$ among CAIs, in contrast to the relatively constant values found in four Allende and Efremovka CAIs [2].
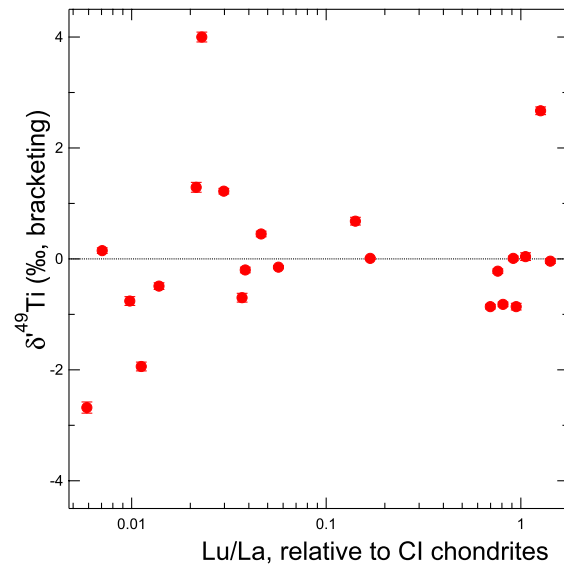

Fig. 3. There is no correlation between Ti MDF effects and REE patterns, although Group II CAIs. have a wider range of MDF effects.
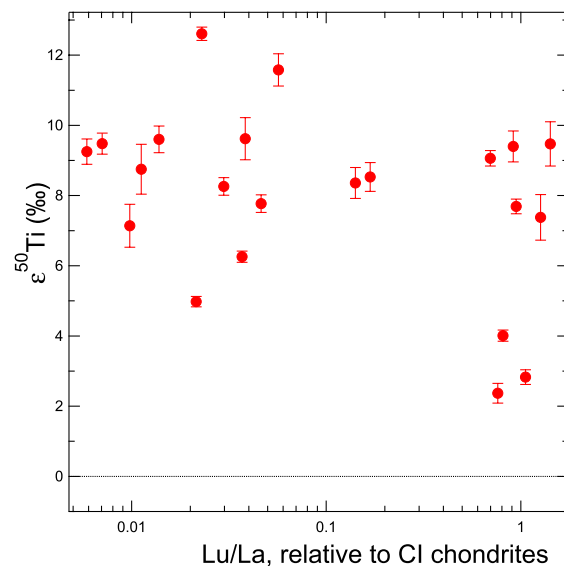

Fig. 4. There is no correlation between 50Ti anomalies and REE patterns.

References: [1] Clayton R. N. et al. (1988) *Phil. Trans. R. Soc. Lond., A325*, 483. [2] Trinquier A. et al. (2009) *Science, 324*, 374. [3] Zhang J. et al. (2012) *Nature Geosci., 5*, 251. [4] Huang S. et al. (2011) *Geochim. Cosmochim. Acta, 77*, 252. [5] Zhang J. et al. (2011) *J. Anal. At. Spectrom., 26*, 2197. [6] Millet M.-A. (2014) *J. Anal. At. Spectrom., 29*, 1444. [7] Pourmand A. et al. (2012) *Chem. Geol., 291*, 38. [8] Zhang J. et al. (2014) *Geochim. Cosmochim. Acta, 140*, 365. [9] Boynton W. V. (1975) *Geochim. Cosmochim. Acta, 39*, 569. [10] Davis A. M. & Grossman L. (1979) *Geochim. Cosmochim. Acta, 43*, 1611.

SIMULTANEOUS ANALYSIS OF IRON AND NICKEL ISOTOPES IN PRESOLAR SIC GRAINS WITH CHILI.

R. Trappitsch[1,2,*], T. Stephan[1,2], A. M. Davis[1,2,3] M. J. Pellin[1,2,3,4], D. Rost[1,2], M. R. Savina[1,5], C. H. Kelly[1,2], and N. Dauphas[1,2,3], [1]Chicago Center for Cosmochemistry, [2]Department of the Geophysical Sciences, The University of Chicago, [3]Enrico Fermi Institute, The University of Chicago, [4]Materials Science Division, Argonne National Laboratory, [5]Physical and Life Sciences Division, Lawrence Livermore National Laboratory. ([*]trappitsch@uchicago.edu)

Introduction: Presolar grains are small, up to μm-sized particles that formed in the vicinity of dying stars and were incorporated into Solar System material at its formation. These grains still carry the isotopic signature of their parent stars. While certain elements in SiC grains from asymptotic giant branch (AGB) can be used to study the s-process in detail, other elements, like Fe and Ni, are expected to show minimal effects from nucleosynthesis in the star. These elements are therefore good proxies to study galactic chemical evolution (GCE). Model calculations [e.g., 1] predict that the neutron-rich isotopes ^{58}Fe and ^{64}Ni in AGB stars show some effects from the s-process, up to ~100‰ excess in ^{58}Fe and up to ~500‰ excess in ^{64}Ni. These excesses can be used to determine the type of parent star and thus to correct the minor isotopes for s-process contributions. The actual isotopic composition that went into the star in the first place can be inferred from this. In the present study, we measured 11 presolar SiC grains simultaneously for their Fe and Ni isotopic composition. All of these grains are at this point unclassified, however, all of the measured Fe and Ni analyses agree with expectations from nucleosynthesis models of low-mass stars.

Methods: We used the CHicago Instrument for Laser Ionization (CHILI) [2, 3] to determine the Fe and Ni isotopic composition of the given samples. Acid-cleaned presolar grains [4] were mounted and pressed into gold foil. Sample material was subsequently desorbed using a 351 nm UV laser. After ejecting secondary ions from the system, the neutral particles were resonantly ionized using six tunable Ti:sapphire lasers. Three lasers were used for each element. Details about the resonance ionization are given in [5]. The photoions were then extracted into a time-of-flight mass spectrometer and detected with a microchannel plate with a single anode. The measurements are done with a repetition rate of 1 kHz, and each shot is recorded separately [5]. Since the mass resolution of CHILI cannot resolve ^{58}Fe from ^{58}Ni, we delayed the Ni ionization event by 200 ns with respect to the Fe ionization event [5]. Therefore, the two peaks shift apart from each other by half a mass unit – a shift that can be easily resolved in CHILI. This allows the simultaneous analysis of Fe and Ni without isobaric interferences. This is the first time that such a time discrimination scheme is used in RIMS for measuring the isotopic compositions of elements that have direct iso-

bars. To standardize our measurements, we used stainless steel with an Fe/Ni ratio of ~7 and a NIST SRM 610 glass with an Fe/Ni ratio of ~1. Both standards showed the same isotope ratios, except for interferences with TiO on ^{62}Ni and ^{64}Ni in the glass. We also measured the gold substrate itself. Aside from the surface layer in which we detected a few counts for usually less than a second of measurement time, we did not see any contamination in the gold.

Results and Discussion: The Fe isotopic composition (see Figure 1) in the 11 measured grains shows some excesses in δ^{57}Fe and a hint of excess in δ^{58}Fe. The isotope ratio of ^{54}Fe/^{56}Fe is close to the Solar System value. Figure 1 also shows our previous measurements of Fe isotopic composition [6] using the CHARISMA instrument at Argonne National Laboratory as well as data measured by secondary ion mass spectrometry (SIMS) [7]. The uncertainties of the measurements performed with CHILI are up to a factor of 2 smaller than for previous measurements with CHARISMA [6] and about a factor of 4 smaller than for measurements by SIMS [7], allowing the detection of small GCE effects. The Ni isotopes show Solar System composition in δ^{61}Ni. The values for δ^{60}Ni , δ^{62}Ni, and

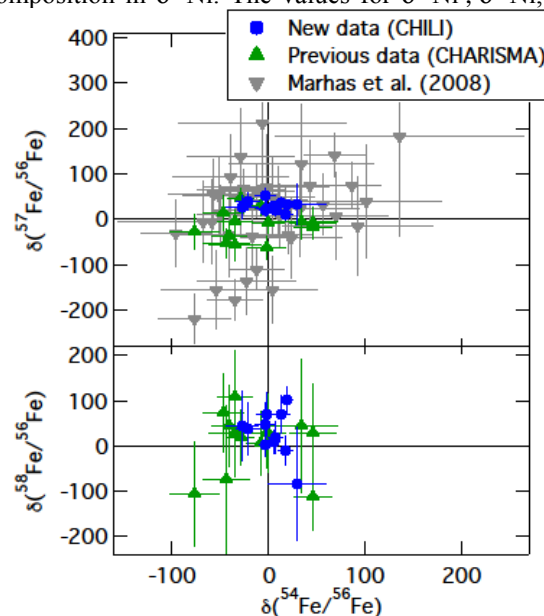*Figure 1. Iron isotopic ratios in comparison with literature values [6, 7]. Uncertainties are 1σ.*

δ^{64}Ni show hints of excesses in these isotopes. The Ni data however have uncertainties comparable to data from SIMS measurements [7]. This is due to the fact that our detected Ni abundance is much lower than the Ni abundance found previously [7], resulting in larger uncertainties.

Elemental Fe/Ni ratio. On average, the measured elemental fractionation between Ni and Fe is 0.59 in the stainless steel and 0.56 in the NIST SRM 610 glass. The reason why our detection of Fe is better than the detection of Ni by almost a factor of two is explained by the laser ionization scheme. As described in [5], about half the Ni neutrals are in the ground state after the desorption event, our first ionization laser however starts at a low-lying excited state and the ground state is thus not used in our ionization scheme. This results in a loss of about 50% of the Ni isotopes. The two fractionation factors for steel and glass are very similar, even though they were determined on two very different matrices. It is reasonable to assume that the fractionation factor for a SiC matrix is similar as well. Figure 2 shows the estimated Fe/Ni elemental ratios that we calculated for our samples. Uncertainties from the fractionation factor and the count rates are smaller than the symbols. The blue shaded area shows the Fe/Ni elemental range measured by SIMS [7]. The Ni abundance in these measurements was much higher than in our case. It is unclear if and how these samples could have been contaminated with extra Ni. One possible source of contamination could be the gold the presolar grains were mounted on. We previously discovered that even high-purity gold can be contaminated with Ni, even if no Fe contamination is detected. Another possibility could be that meteoritic Ni was incompletely removed during grain separation. Taken at face value, our results suggest that ~90% of the Ni signal measured by [7] may have been extraneous to the SiC. Our measurements were performed on acid-cleaned presolar grains [4], and we analyzed the gold substrate our grains were mounted on and detected neither Fe nor Ni contamination.

Comparison of presolar grain data with nucleosynthesis and GCE models. All of the measured presolar grains show close to Solar System composition in their Fe and Ni isotopes. We can thus conclude that these grains come from low-mass stars. We see a slight enhancement in ^{58}Fe and ^{64}Ni; however, due to the large uncertainties, we cannot determine a unique type of star that would produce this excess. GCE calculations predict that all minor Fe isotopes are depleted by >100‰ compared to ^{56}Fe and that all minor Ni isotopes are enhanced by >200‰ compared to ^{58}Ni [8]. Our results show that δ^{60}Ni and δ^{62}Ni might show a slight enhancement compared to the Solar System; also δ^{57}Fe shows a

slight enhancement. We do not see, however, the high depletion and enhancement for Fe and Ni isotopes predicted by [8]. GCE models have similar problems explaining Si isotopes, which should also show only minor *s*-process contributions. Correlating multiple GCE dominated elements can help in the future to better understand the processes that contributed to the chemical composition of the galaxy.
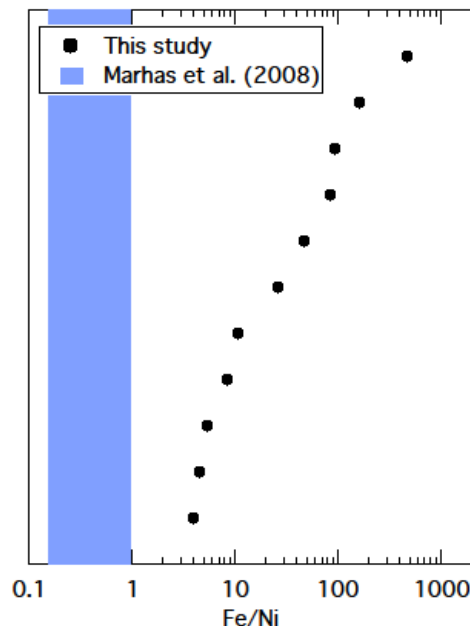

Figure 2. Fe/Ni elemental ratio in the measured samples.

Summary and Outlook: We present Fe and Ni isotopic compositions of 11 presolar SiC grains including interference free, simultaneous analyses of ^{58}Fe and ^{64}Ni. We see a slight enhancement in several isotopes. Uncertainties in the neutron rich isotopes are at this point too high to clearly determine the type of parent star for these grains. These are preliminary results, and more Fe and Ni measurements in presolar grains will soon be performed. We will subsequently measure the Si and C isotopic abundance in these presolar grains to classify them. Since Si isotopes are also mostly dominated by GCE, it remains to be seen if correlations between Si, Fe, and Ni isotopes exist.

References: [1] Gallino et al. (1998) *ApJ, 497*, 388–403. [2] Stephan et al. (2013) *LPS 44,* #2536. [3] Stephan et al. (2014) *LPS 45*, #2825. [4] Levine et al. (2009) *Int. Journal of Mass Spec., 288*, 36-43. [5] Stephan et al. (2016) *LPS 46,* this meeting. [6] Trappitsch R. et al. (2012) *LPS 43,* #2497. [7] Marhas et al. (2006) *ApJ, 689*, 622–645. [8] Kobayashi et al. (2011) *ApJ, 414*, 3231–3250.

A SEARCH FOR SHOCKED CHROMITES IN FOSSIL METEORITES WITH RAMAN SPECTROSCOPY. S. S. Rout[1,2*], P. R. Heck[1,2,3] and B. Schmitz[1,4], [1]Robert A. Pritzker Center for Meteoritics and Polar Studies, The Field Museum of Natural History, 1400 S. Lake Shore Drive, Chicago IL, 60605, USA. [2]Chicago Center for Cosmochemistry, [3]Department of Geophysical Sciences, The University of Chicago, 5734 S. Ellis Avenue, Chicago IL, 60637, USA. [4]Department of Physics, Lund University, Lund, Sweden. *srout@fieldmuseum.org

Introduction: The L-chondrite parent body breakup (LCPB) in the asteroid belt ~470 Ma ago produced ejecta that was discovered as fossil meteorites (FM) in Sweden and abundant fossil micrometeorites worldwide within post LCPB mid-Ordovician sediments [1,2]. Both elemental and isotopic studies of relict chromite and chrome-spinel from these extraterrestrial materials have confirmed that they are L chondritic except one which was classified as winonaite-like [2-4]. Many of the modern L chondrite meteorites show extensive shock metamorphism and presence of high pressure phases within shock melt veins (SMVs) [5]. Two high-pressure polymorphs of chromite were discovered in a SMV of the Suizhou L6 chondrite [6]. Experiments determined the higher-pressure phase, xieite (orthorhombic $CaTi_2O_4$-type), that forms between 18-23 GPa and 1800–1950°C and the intermediate phase, CF-chromite (orthorhombic $CaFe_2O_4$-type), forming above ~12.5 Gpa and 1700-1800ºC [7].

We therefore expect that the chromites from SMVs within the FM could have been also transformed in the shock event that lead to the LCPB. Finding shock signatures can help us constrain the P,T history of the FM and the LCPB event. Here, we present results from a survey for high pressure phases of chromite within shocked modern L chondrites and in FM.

Samples and Methods: Polished thin sections (PTS) from Tenham (L6, S6; ME 2617; #4) and Catherwood (L6, S6; ME 3066; #2, and #3) from the Field Museum collection and Coorara (L6, S6; USNM 5591-1) from the Smithsonian National Museum of Natural History were searched for chromite within and near SMVs using BSE/EDS mapping with the Field Museum's Zeiss Evo 60 SEM equipped with an Oxford Aztec SDD EDS system (Fig. 1). Chromite grains from these L6 chondrites, and polished mounts from [3] with chromites from Mount Tazerzait (L5), Hessle (H5), and FM from the Thorsberg (Österplana) and the Gärde (Brunflo) quarries were then studied using a HORIBA LabRAM HR Evolution confocal Raman system at the NUANCE facility, Northwestern University. A 532 nm Ar^+ laser was focused to ~1 μm spot and spectra were accumulated for 120 sec. Raman spectra were obtained from 47 chromite grains from 12 FM found in 8 sedimentary beds, 4 from Mount Tazerzait, 1 from Hessle, 20 grains from Coorara, 39 from Catherwood, and 11 from Tenham.

Results: Some of the grains from FM are highly fractured (Fig. 1d), similar to matrix chromite grains found outside the SMVs in L6 chondrites (Fig.1a). We found four grains within SMVs of Tenham and Catherwood (Fig. 1c) that we identified as intergrowths of chromite and CF-chromite or xieite, from their Raman spectra: primary peaks at ~605 cm^{-1} and ~684 cm^{-1} (Fig. 2). Chromites outside the SMVs show a distinct primary peak between 686-688 cm^{-1} and two secondary peaks at ~600 cm^{-1} and 496-500 cm^{-1} (Fig. 2). Most of the chromites within SMVs have only a broad peak before a primary peak at 680-685 cm^{-1} (Fig. 2). Raman spectra of the chromites can be divided into three groups: I) spectra similar to matrix chromites from Tenham, Catherwood and Coorara (51% of analyzed FM chromites); II) spectra with a large and broad peak between 500-600 cm^{-1} before the primary peak at 685-689 cm^{-1} (30% of analyzed FM chromites). We only find three chromites with group II spectra in the SMVs of Coorara L6 chondrite and none in the matrix of any of the analyzed modern meteorites; III) spectra similar to chromites in SMVs from Tenham, Catherwood and Coorara (19% of analyzed FM chromites; Fig. 2); IV) spectra produced from an intergrowth of matrix chromite and CF-chromite or xieite (none of FM chromites; Fig. 2).

Discussion: Group I spectra of FM chromites indicate that these are matrix chromites. At present we cannot explain the broad peak between 500-600 cm^{-1} in group II spectra. Our current dataset on group II spectra in modern meteorites is limited to three grains in SMVs only and we cannot determine with confidence yet if the FM chromites with group II spectra are from SMVs or matrix. The chromites with group III spectra inside the SMVs occur as closed packed polycrystalline aggregates (Fig. 2) and still have the Raman peak at ~684 cm^{-1}, characteristic of the spinel structure of low-pressure chromite. Thus, the crystal structure has not changed from spinel-type to something else, and is neither CF-type chromite nor xieite. It is difficult to differentiate between CF-chromite and xieite by Raman spectroscopy [7]. However, the absence of the secondary Raman peaks which would be expected in the spinel structure is unexpected. This could be due to transformation to an intermediate state that is stable at lower P,T than CF-chromite and xieite. This interme-

diate state could be produced by a fragmentation of the original chromite grain during shock loading or back-
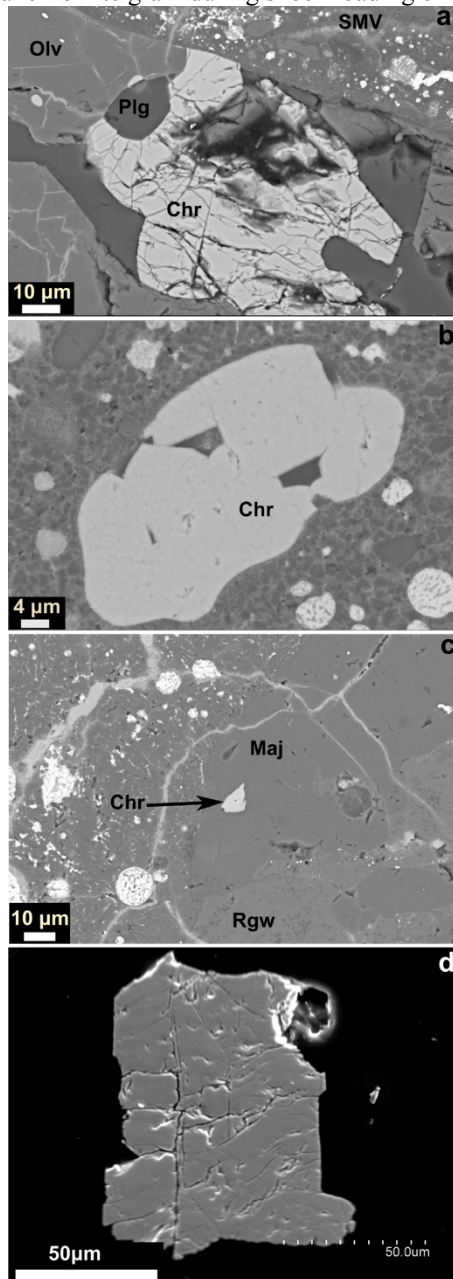

Fig. 1: Back Scattered Electron (BSE) images. (a) Matrix chromite (Chr) grain adjacent to a shock melt vein (SMV) in the Tenham. Olv=Olivine, Plg=Plagioclase; (b) Chr inside a SMV in Catherwood. Bright areas are Fe-sulfide and Fe-metal. Dark line contrast within the grain most probably are grain boundaries separating the sub-grains. (c) Region inside a SMV in Catherwood. Chr grain (Catherwood_c4) is enclosed inside majorite (Maj), which is in contact with ringwoodite (Rgw) and fine grained matrix of the SMV. (d) Chromite grain from the fossil meteorite Sex 003.

transformed to a phase that is stable between normal, spinel-type chromite and higher pressure, CF-type chromite.

Conclusions: The majority of the FM chromite grains are matrix chromite (51%, Group I). None of the studied chromites from FM have been transformed all the way to the high-pressure phase CF-chromite or xieite but some grains (19%, Group III) do show signatures of intermediate shock similar to the chromite grains found within the SMVs of modern L chondrites. The remaining (30%, Group II) FM chromites could be from SMVs but this needs to be verified in follow up studies. TEM analysis of chromites from all groups from SMVs, matrix and FM will be done to investigate the shock effects in more detail.
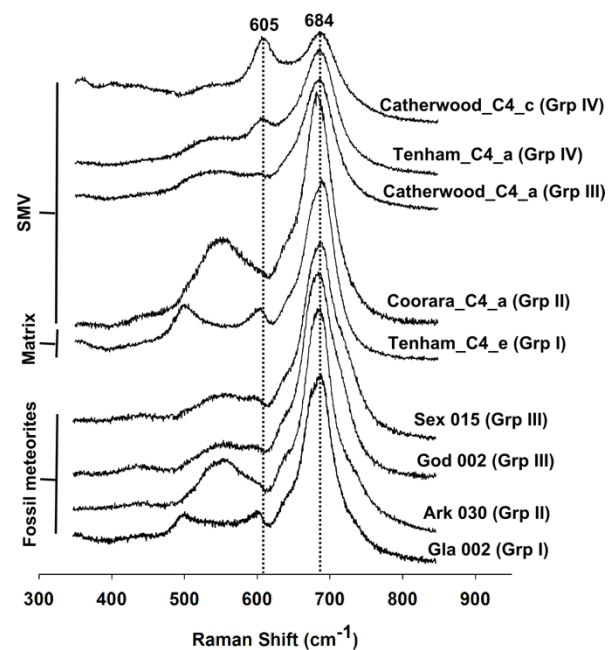

Fig. 2: Stacked Raman spectra of chromites from Tenham, Catherwood and Coorara L6 chondrites and fossil meteorites. The spectra from matrix chromites and chromites within SMVs of Tenham and Catherwood show the progressive transformation of low pressure chromite to high pressure chromite. The values on top indicate the peak position of Catherwood_C4 chromite (Fig. 1c).

References: [1] Schmitz B. et al. (2003) *Science 300,* 961–964. [2] Schmitz B. (2013) *Chemie der Erde 73*, 117-145. [3] Heck P. R. (2010) *Geochim. Cosmochim. Acta, 74,* 497–509. [4] Schmitz B. et al. (2014) *EPSL 400*, 145–152. [5] Sharp D. G. and DeCarli P. S. (2006) *Meteorite and Early Solar System II,* pp. 653-677. [6] Chen M. (2003) *Geochim. Cosmochim. Acta, 67,* 3937-3942. [7] Chen M. et al. (2003) *PNAS*, 100, 14651-14654.